

**A Study of the Prediction of Vibration-Induced
Fretting Corrosion in Electrical Contacts**

by

Chen Chen

A dissertation submitted to the Graduate Faculty of
Auburn University
in partial fulfillment of the
requirements for the Degree of
Doctor of Philosophy

Auburn, Alabama
December 18, 2009

Keywords: electrical contacts, fretting corrosion,
modeling, finite element analysis

Copyright 2009 by Chen Chen

Approved by

George T. Flowers, Chair, Alumni Professor of Mechanical Engineering
Jeffrey C. Suhling, Quina Distinguished Professor of Mechanical Engineering
Robert L. Jackson, Associate Professor of Mechanical Engineering
Michael J. Bozack, Professor of Physics Department

Abstract

It is generally recognized that fretting corrosion is one of the major failure mechanisms in electrical contacts. The negative effects of fretting corrosion were found in many areas such as aerospace, automobile, electrical packaging, etc. In recent years, much of the research work has focused on the causes of fretting corrosion, the mechanism of this phenomenon, and its prevention. However, nowadays, most evaluation of the connector fretting corrosion is conducted through exhaustive experiments, making the connector design and validation process time consuming and costly. Therefore, a new method using modeling and simulation techniques to predict the influence of various design factors on vibration-induced fretting propensity in electrical connectors would be very beneficial to the study of the fretting corrosion.

In the author's work, a series of studies concerned with the modeling, analysis and experimental validation of vibration-induced fretting corrosion of electrical connector were conducted. A FEA based methodology was developed and optimized to predict and simulate the vibration-induced fretting corrosion on both typical single blade/receptacle connector pair. A series of corresponding experiments were then performed to evaluate its performance. Comparison between 2-D simplified and 3-D detailed modeling and analysis method were conducted. The 3-D detailed simulation was proved to be more accurate but requires larger computational cost. The influences of different connector design factors were investigated in both simulation and experiments. The relative motion

at contact interface was proved to be a great indicator for the threshold of fretting corrosion. Finally, the simulation results were found to be in good agreement with experimental results. It is demonstrated that, this finite element modeling and analysis method have great potential in predicting of the vibration-induced fretting corrosion in electrical contacts.

Acknowledgements

I would like to express my sincere thanks and deep appreciation to my advisor Dr. George T. Flowers for his guidance in the completion of this research work in Auburn University. His wise suggestions, his generous support and his whole-heartedly encouragement contributed immensely to the fulfillment of my study and lighted my path towards the magnificent science palace.

I also would like to thank the other advisory committee members, Dr. Jeffrey C. Suhling, Dr. Robert L. Jackson, and Dr. Michael J. Bozack for their academic instructions and assistance. I also thank Dr. John L. Evans for his valuable comments and corrections, and for his great help for being my outside reader.

Special thanks would be given to all my friends, especially Dr. Fei Xie and Dr. Alfonso Moreira, which without their constant support this “journey” would have been very difficult to accomplish.

Finally, I would like to express my greatest gratitude and gratefulness to my parents, Zhaocai Chen and Aihua Liu, whose love, care and perpetual support have been invaluable for the completion of this degree (Doctor of Philosophy in Mechanical Engineering).

Table of Contents

List of Figures.....	ix
List of Tables.....	xv
Chapter 1 Introduction and Literature Review	1
1.1 Fretting Corrosion.....	2
1.2 Finite Element Method	3
1.3 Literature Review of Fretting Corrosion in Electrical Contacts	5
Chapter 2 A Study of Vibration- Induced Fretting Corrosion in a Single Blade/Receptacle Connector Pair	14
2.1 Introduction.....	14
2.2 Experimental Configuration.....	15
2.2.1 Experimental Samples	15
2.2.2 Experimental Equipment	17
2.2.2.1 Keithley Model 2010 Multimeter	17
2.2.2.2 Polytec Laser Vibrometer System	18
2.2.2.3 HP 35665A Dynamic Signal Analyzer	19
2.2.2.4 Vibration System	20
2.2.3 Experimental Setup.....	23
2.2.3.1 Transfer Function Measurement.....	23

2.2.3.2	The Fretting Threshold Level Measurement.....	26
2.3	Finite Element Model	28
2.3.1	Geometric Model	28
2.3.2	Material Properties.....	31
2.3.3	Boundary Conditions	31
2.4	Vibration Process Simulation	33
2.5	Experiment and Simulation Results.....	35
2.5.1	Transfer Function Results.....	35
2.5.1	Fretting Threshold Results.....	42
2.6	Summary and Conclusions	53
Chapter 3	Three Dimensional Modeling and Anlysis of a Blade/Receptacle Connector Pair for the Prediction of Vibration-Induced Fretting Degradation.....	55
3.1	Introduction.....	55
3.2	Three Dimensional Detailed Finite Element Model Generation	56
3.2.1	Geometric Model	56
3.2.2	Mesh Control	58
3.2.3	Parallel Execution	60
3.2.4	Define Contact	62
3.3	Simulation Methodology and Boundary Conditions	63
3.3.1	Mating Process Simulation	63
3.3.2	Boundary Conditions	67
3.4	3-D Detailed Model Simulation Results.....	69

3.4.1	Transfer Functions	69
3.4.2	Threshold Values	76
3.5	Computational Cost	81
3.5	Summary and Conclusions	82
Chapter 4	The Application of FEA Simulation Techniques to the Fretting Degradation of a Connector System	84
4.1	Introduction.....	84
4.2	Experimental Configuration.....	85
4.2.1	Experimental Samples	85
4.2.2	Experimental Equipment	87
4.2.3	Experimental Setup.....	92
4.3	FEA Modeling	94
4.3.1	Detailed Three Dimensional Model.....	94
4.3.2	Simplified Two Dimensional Model	95
4.3.3	Comparison between 2-D and 3-D Model	97
4.4	Experiment and Simulation Results.....	98
4.4.1	Transfer Function.....	98
4.4.2	Fretting Rate.....	102
4.5	Summary and Conclusions	106
Chapter 5	Conclusions and Recommendations	108
References	111
Appendix A	Ansys Log File for the 2-D Simplified Finite Element Model	119

Appendix B	MATLAB Code Example for Transfer Function and Relative Motion	
	Calculation	146

List of Figures

Figure 2-1: Photograph of the blade and receptacle parts.....	16
Figure 2-2: Mated blade/receptacle pair	16
Figure 2-3: Four-wire dry circuit resistance measurement	18
Figure 2-4: Photograph of the Polytec laser vibrometer system.....	19
Figure 2-5: Photograph of HP 35665A dynamic signal analyzer	20
Figure 2-6: PA 500L amplifier	21
Figure 2-7: V408 shaker	22
Figure 2-8: Typical vibration system.....	22
Figure 2-9: Experimental setup of the transfer function measurement.....	25
Figure 2-10: Detailed view of displacement measurement.....	26
Figure 2-11: Photograph of the fretting threshold levels experiment setup.....	27
Figure 2-12: Photograph of the resistance measurement.....	27
Figure 2-13: Overall view of the 2-D geometric model	29
Figure 2-14: Close-up view of the 2-D geometric model.....	29
Figure 2-15: Geometric model for the blade/receptacle configuration.....	32
Figure 2-16: Sinusoidal vibration excitation with the load substeps	33
Figure 2-17: Full model motion at Time 1 during vibration.....	34
Figure 2-18: Motion of the blade and the receptacle at time 1	34

Figure 2-19: Motion of the blade and the receptacle at time 2	35
Figure 2-20: Node locations for the transfer function simulation.....	36
Figure 2-21: Transfer function results from experiment and 2-D model simulation for different friction coefficient.....	37
Figure 2-22: Experimental results for different contact normal force levels.....	38
Figure 2-23: 2-D simulation results for different contact normal force levels	38
Figure 2-24: Experimental results showing the variation of transfer function with excitation amplitude for Specimen Type 1.a	40
Figure 2-25: Experimental results showing the variation of transfer function with excitation amplitude for Specimen Type 2.a	40
Figure 2-26: Simulation of relative motion transfer functions for various wire tie-off lengths (Specimen Type 1.a).....	41
Figure 2-27: Simulation of relative motion transfer functions for various levels of supplementary mass (Specimen Type 1.a).....	42
Figure 2-28: Identification of the threshold displacement (or g-level).....	44
Figure 2-29: SEM picture of accumulation area.....	45
Figure 2-30: Simulated X-axis relative motion at position 2.....	48
Figure 2-31: Comparison between experimental and simulation results for fretting threshold displacements of Type 1.a.....	49
Figure 2-32: Comparison between experimental and simulation results for fretting threshold displacements of Type 1.b	49
Figure 2-33: Comparison between experimental and simulation results for fretting threshold displacements of Type 1.c.....	50

Figure 2-34: Comparison between experimental and simulation results for fretting threshold displacements of Type 2.a.....	50
Figure 2-35: Comparison between experimental and simulation results for fretting threshold displacements of Type 2.b	51
Figure 2-36: Comparison between experimental and simulation results for fretting threshold displacements of Type 2.c.....	51
Figure 2-37: Comparison of fretting threshold displacements for Type 1 samples with different contact normal forces	52
Figure 2-38: Comparison of fretting threshold displacements for Type 2 samples with different contact normal forces	53
Figure 3-1: Overall view of the 3-D geometric model	57
Figure 3-2: Close-up view (cross section) of the 3-D geometric model.....	57
Figure 3-3: Partitions in the receptacle component	59
Figure 3-4: Picture of the workstation for the 3-D simulation.....	61
Figure 3-5: Defined contact pair in 3-D model.....	63
Figure 3-6: Unmated connector pair	64
Figure 3-7: Connector pair in mating process.....	65
Figure 3-8: Mated connector pair	65
Figure 3-9: Unmated receptacle part.....	66
Figure 3-10: Mated connector pair	67
Figure 3-11: Boundary conditions in the 3-D model.....	68
Figure 3-12: Nodes location in the 3-D detailed model.....	70

Figure 3-13: Experimental transfer function results for different contact normal force levels	71
Figure 3-14: 2-D simulation transfer function results for different contact normal force levels	72
Figure 3-15: 3-D simulation transfer function results for different contact normal force levels	72
Figure 3-16: Comparison of experimentally determined transfer function and 2-D simulation model results	73
Figure 3-17: Comparison of experimentally determined transfer function and 3D simulation model results	74
Figure 3-18: Comparison between 2-D simulation and 3-D simulation of relative motion transfer functions for various tie-off lengths (Specimen Type 2.b).....	75
Figure 3-19: Comparison between 2-D simulation and 3-D simulation of relative motion transfer functions for various tie-off lengths (Specimen Type 2.b).....	75
Figure 3-20: Comparison between 3D simulation results and experimental results for scaled inverse relative motion transfer functions for Type 1 samples.....	76
Figure 3-21: Comparison between 3D simulation results and experimental results for scaled inverse relative motion transfer functions for Type 2 samples.....	77
Figure 3-22: Comparison of 2-D simulation, 3-D simulation and experimental results with scaled inverse relative motion transfer functions (Specimen Type 1.a).....	78
Figure 3-23: Comparison of 2-D simulation, 3-D simulation and experimental results with scaled inverse relative motion transfer functions (Specimen Type 1.b).....	78

Figure 3-24: Comparison of 2-D simulation, 3-D simulation and experimental results with scaled inverse relative motion transfer functions (Specimen Type 1.c).....	79
Figure 3-25: Comparison of 2-D simulation, 3-D simulation and experimental results with scaled inverse relative motion transfer functions (Specimen Type 2.a).....	79
Figure 3-26: Comparison of 2-D simulation, 3-D simulation and experimental results with scaled inverse relative motion transfer functions (Specimen Type 2.b).....	80
Figure 3-27: Comparison of 2-D simulation, 3-D simulation and experimental results with scaled inverse relative motion transfer functions (Specimen Type 2.c).....	80
Figure 4-1: Photograph of the connector system sample.....	86
Figure 4-2: Photograph of the connector system sample.....	87
Figure 4-3: Photograph of LDS V850 shaker with KISTLER accelerometer.....	90
Figure 4-4: DACTRON vibration control system and SPAK amplifier.....	90
Figure 4-5: Diagram of LDS vibration test system.....	91
Figure 4-6: Photograph of the experimental setup.....	92
Figure 4-7: Photograph of transfer function measurement.....	93
Figure 4-8: Diagram of transfer function measurement configuration.....	94
Figure 4-9: Picture of the 3-D detailed connector system model.....	95
Figure 4-10: Overall view of the 2-D connector system model.....	96
Figure 4-11: Detailed view of the 2-D connector system model.....	96
Figure 4-12: Comparison of computational cost for initial simulation between 2-D model and 3-D model.....	98
Figure 4-13: Comparison of experimentally determined transfer function and 2-D model simulation results.....	99

Figure 4-14: Experimental determined transfer function results for different contact normal force levels of specimen Type 1	100
Figure 4-15: Simulation transfer function results for different contact normal force levels of specimen Type 1	101
Figure 4-16: Experimental determined transfer function results for different contact normal force levels of specimen Type 2.....	101
Figure 4-17: Simulation transfer function results for different contact normal force levels of specimen Type 2.....	102
Figure 4-18: X-axis relative motion for different contact normal force levels for specimen Type 1 in simulation	104
Figure 4-19: X-axis relative motion for different contact normal force levels for specimen Type 2 in simulation	104
Figure 4-20: Rate of resistance change for Type 1 sample in experiment.....	105
Figure 4-21: Rate of resistance change for Type 2 sample in experiment.....	105

List of Tables

Table 2-1: Different types of experimental samples.....	17
Table 2-2: Displacement decoder specification of the laser vibrometer system	19
Table 2-3: Material and dimensional properties of the model components.....	30
Table 2-4: Relationship analysis for type 1.a connector pair.....	46
Table 2-5: Relationship analysis for type 2.a connector pair.....	47
Table 3-1: Material properties for 3-D model components	58
Table 3-2: Mesh techniques and size control for different components.....	60
Table 3-3: Specifications of the workstation	61
Table 3-4: Corresponding circular frequency values in the 3-D simulation.....	69
Table 4-1: Types of Experimental Samples.....	86
Table 4-2: G-levels and corresponding displacements at shaker head	103

CHAPTER 1 INTRODUCTION AND LITERATURE REVIEW

It is generally recognized that fretting corrosion is one of the major failure mechanisms in electrical contacts. In recent years, much of the research work was focused on the causes of fretting corrosion, the mechanism of this phenomenon and its prevention. However, most evaluation of the connector fretting propensity is conducted through exhaustive experiments, making the connector design and validation process time consuming and costly. Therefore, a method using modeling and simulation techniques to predict the influence of various design factors on the vibration-induced fretting corrosion in electrical connectors would be very beneficial.

In the author's work, a series of studies concerned with the modeling, analysis and experimental validation of vibration-induced fretting corrosion of electrical contacts were conducted. Based on these results, the dissertation is divided into five chapters. In chapter one, an introductory material as well as a comprehensive literature review about the vibration-induced fretting corrosion problem such as the meaning of fretting corrosion, the mechanism of this phenomenon, the history of related study, the present status of the research on this topic are stated. Chapter two describes a study of vibration-induced fretting corrosion in a single blade-receptacle connector pair. A research on the three-dimensional modeling and analysis method on the prediction of vibration-induced fretting corrosion is discussed in Chapter three. Chapter four describes the application of FEA

techniques to the fretting degradation of a connector system. All the studies discussed in this dissertation are then summarized in chapter five and some recommendations for the necessary further work on this topic are also provided.

1.1 Fretting Corrosion

Fretting is one of the major contact failure mechanisms. It is a small amplitude contact movement between two contacting surfaces. Such micro motions (slip) may range from a few μm to as much as 100 μm in electronic connectors. This slip can be produced by external vibrations, changing temperatures, differential thermal expansion of the contacting metals, load relaxation, and junction heating as the power is switched on and off.

Fretting causes metal transfer and wear at the contact interface. This fretting damage serves to repeatedly expose fresh metal to atmospheric oxidation for non-precious metal plated contact interfaces. This base-metal contact produces insulating oxide debris. The formation of metallic wear and oxidized debris is resulted from the adhesion, abrasion, and delamination wear progress in fretting. Catalytic materials such as palladium and other platinum group metals yield the insulating frictional polymers. The precursors to these polymers are absorbed organic air pollutants from the atmosphere. The accumulation of these insulating solids in the contact zone causes electrical resistance to increase. If these substances are inorganic solids, like oxides, the process is called "fretting corrosion"[1].

It is widely know that fretting corrosion is a frequent cause of failure of suspension springs, bolt and rivet heads, king pins in auto steering mechanisms, jewel bearings, variable-pitch propellers, shrink fits, contacts of electrical relays, connecting

rods, and other parts of vibrating machinery. It may also cause discoloration of stacked metal sheets during shipment. An early documented example of fretting corrosion was recognized when automobiles were being shipped some years ago by railroad from Detroit to the West Coast. By the reason of vibration, the ball-bearing races of the wheels became badly pitted by fretting corrosion. Therefore the automobiles were not operable on arrival. This damage was worse in winter than in summer, but could be avoided if the load on the wheels was relieved during shipment.

It is proven from laboratory experiments that fretting corrosion of steel against steel requires oxygen but not moisture. Moreover, damage is less in moist air compared to dry air and is markedly less in a nitrogen atmosphere. Damage increases as the temperature decreases, so the mechanism is clearly not electrochemical in nature. Increasing the load increases the damage. Fretting corrosion is also worsened by increased slip, provided the surface is not lubricated. Increases in frequency for the same number of cycles tend to decrease damage, but in nitrogen no frequency effect is observed [1].

1.2 Finite Element Method

The finite element method (FEM), sometimes named finite element analysis (FEA), is a computational technique which is used to obtain approximate solutions of boundary value problems in engineering. In simple, a boundary value problem is a mathematical problem in which one or more dependent variables must satisfy a differential equation everywhere within a known domain of independent variables and satisfy specific conditions on the boundary of domain [2]. FEM technology has been widely used in solving structural, mechanical, heat transfer, and fluid dynamics problems

as well as problems of other disciplines. The advancement in computer technology enables us to solve an even larger system of equations, to formulate and assemble the discrete approximation, and to display the results quickly and conveniently. This has also helped the finite element method become a powerful tool.

From the early 1900s, Rayleigh [3], Ritz [4] used trial functions to approximate solutions of differential equations. Galerkin [5] used the same concept for solution and provided a very strong basis for the finite element method. However, the finite element method didn't have its real start until Courant [6] introduced the concept of piecewise-continuous functions in a sub-domain in 1943. In the late 1940s, a matrix method of the force analysis was developed by certain aircraft engineers known as the flexibility method. In 1960, the term finite element was first used by Clough [7] in the context of plane stress analysis and has been in common usage since that time. From then on, the finite element method was extended to applications in shell bending, plate bending, pressure vessels, fluid flow, heat transfer [8][9], and general three-dimensional problems in elastic structural analysis.

The finite element method is computational intensive due to the complicated operation on very large matrices. Therefore, finite element software code was developed by taking advantage of the great computational capacity of modern computers. The first software code was NASTRAN [10] in conjunction with the space exploration program of the United States in 1960s. Since then, different commercial software packages have been introduced for finite element analysis, such as ANSYS [11], ALGOR [12], COSMOS [13] and ABAQUS [14]. Most of these packages can be used on desktop computers and

workstations to solve large problems in many areas under today's computational environment.

1.3 Literature Review of Fretting Corrosion in Electrical Contacts

An understanding of the processes which contribute to connector degradation is necessary to facilitate the correct selection of contact materials and component designs and to establish the conditions in which they must be used so as to assure reliable performance. Fretting corrosion is known as a typical problem for many electrical and electronic equipments which could lead to huge cost in repair and replacement. Nevertheless, the negative effect of fretting corrosion was not generally recognized as a serious factor of electrical connector degradation problems until Bock and Whitley [15] clearly demonstrated its importance in 1974.

From then on, a series of systematic studies of the fretting corrosion phenomenon in electronic connectors were conducted [16][17][18][19][20]. In 1984, Antler [21] provided a comprehensive review of fretting corrosion problem. In his study, the mechanisms of this phenomenon were systematically discussed such as transfer, wear, oxidation, and frictional polymerization that apply to the fretting of contacts; the effect of operational parameters such as the cycle rate and force on contact resistance change; a survey of materials whose fretting behavior has been characterized; and an analysis of the different roles that lubricants play in controlling fretting according to the contact materials. It was also pointed out that the determination factors of whether contact materials will be satisfactory for a given application were the connector designs, the expected connector lifetimes, and their reliability requirements. Moreover, hardware tests such as shock and vibration were also suggested to be conducted before new contact

designs and materials are incorporated in connectors. Antler concluded that contact resistance is determined by the composition of the interface and this composition may change during fretting with dissimilar metals due to transfer, wear, and film formation. The contact resistance for fretting corrosion and friction polymerizing systems generally becomes more unstable under longer wipe time. Contact resistance transients during fretting may be significantly higher than static contact resistance. Lubricants which may retard the rate of wear of thin noble metals on film-forming substrates by dispersing frictional polymers and thereby reducing the oxidation rate were proved to be able to stabilize the contact resistance. Finally, fretting process has been categorized into four regimes by Slade [1]:

- Stick. Movement between the contact surfaces is accommodated by elastic deformation of the members in the near-surface regions. The asperities are joined, and there is no surface damage until the members are separated. The stick regime may occur for movements of about 1 μm depending on the material, contact geometry, and on other factors.
- Mixed Stick-Slip. There is a central stick area surrounded by an annular slip region where there may be crack formation, fretting fatigue, and wear debris.
- Gross Slip. All asperity contacts are broken during each cycle. Asperities slide across several others of the opposing surface. Damage is extreme with delamination wear. Movements of 10-100 μm are involved.
- Reciprocating Sliding. With large displacements more than 100-200 μm , there is sliding wear which may result in fretting.

Fretting corrosion exists in many application fields. One of the most critical fields is vehicle electronics. The automotive environment combines external vibrations with the strong environmental factors of temperature and humidity. Therefore, fretting corrosion can be a major problem on connector systems used in vehicle electronics. From 1986, studies in this field were underway on automotive connector systems [22][23][24]. An early study on the fretting corrosion of tin-plated copper alloy used for a stepping motor/precision stage assembly was reported by Lee and Mamrick [23] in 1987. The purpose of their research is to explore the physical phenomena of electrical conduction using tin-plated contacts subjected to fretting corrosion and the influence of electric load on the fretting corrosion process. The rise in contact resistance of a tin-plated copper alloy under cyclical minute motion was studied a both dry circuit and then with electrical loads. It was found that in the range of circuit voltage and current investigated, the electrical conduction through slightly corroded contacts was shown not to be affected by the electrical load. For moderately corroded contacts, the resistance characteristic showed a sustained plateau near the melting voltage of Sn, and for severely corroded contacts, a plateau occurred in the resistance range corresponding to the voltage range of the melting, sublimation, and decomposition of the oxides and vaporization of tin. They summarized that the resistance plateaus were consistent with the view that the current passing through the contact constriction caused the contact spots to thermally run-away until melting of the tin occurred. With further corrosion giving higher resistance and more heating, the temperature could rise further up to the melting, sublimation, and decomposition of the oxides and even up to the vaporization of tin collectively forming the second contact resistance or voltage plateau.

In 2000, Swingler, McBride and Maul [25] proved the complexity of the fretting corrosion in vehicle environment. In this study, temperatures of automotive connectors, which were undergoing road testing, were being monitored to evaluate stress levels during real operation. An empirical model of temperature behavior for three types of connectors was presented based on real environmental data obtained from the tests. Furthermore, a number of micro-sensors embedded within a connector housing were then used to enhance this study. This for the first time allows real information about the events occurring at the connector interface.

Nevertheless, relatively few researchers have studied the vibration influence of fretting corrosion in electrical connectors. From 2002, Flowers and Xie [26] investigated the influence of accelerated vibration on fretting corrosion problems. An electrical measurement methodology by monitoring transfer functions and fretting thresholds was provided. The relationship between applied excitation levels and fretting rates was examined. The results of this study exhibited threshold behavior at each frequency for the onset of fretting degradation. Typically a plateau region was observed where similar g-levels produced similar fretting rates. It was also found that outside the plateau region the g-levels varied according to the dynamic behavior of the mechanical system. In addition, a transfer matrix model was used to analyze these results. An empirical fit of the data correlated well with the model when damping was used. This analysis revealed the importance of the bending moment induced at the contact interface as a result of excitation levels and tie-off configurations. Consequently, it is concluded that dynamic response of the mechanical system under various g-levels and tie off configurations can greatly impact the performance of a connector system subjected to vibration stresses.

A different method for measuring the relative motion that causes fretting corrosion was reported recently. In 2005, Lam et.al [27] used a novel thick film sensor to measure the displacement at the connector interface to test for environmental influences on electrical contact fretting. The sensor was assembled into a connector sample, replacing the male component. When the interface experienced movement, the relative displacement of the contact point caused a corresponding linear change in the resistance measured across the male and female connection. The sensors were validated by a series of experiments and subsequently used in a field test to establish the relationships between the fretting effects and temperature, humidity and differential pressure. The group found that the variation in differential pressure dominated the movement behavior at the contact interface of the well-sealed connector sample, while temperature and humidity had negligible influences on the measured relative displacement.

Another similar work was conducted by N. Ben Jemaa and E. Carvou [28] in France in 2006. The purpose of this study was to examine conjointly the wear amount and electrical behavior of connector terminal under vibration and higher current stress. During this experiment, the spring lamellas were firmly attached to a fixed support under high number of vibrations (10³ to 10⁶). High frequency oscillation (100Hz) with amplitude of 50 μ m was used. The contact area was made with copper alloy and coated with 2 μ m of tin. The contact was inserted in resistive circuit supplied by 20V and 3A and the contact voltage was then measured and observed in real time with a fast sampling oscilloscope. Finally, the main results showed that at low level of wear observed during the earlier stage of fretting corresponded to pure constriction voltage less than 20mV. However after this initiation period as the wear is increased, the contact voltage increased

and reached a few hundred milli-volts (melting and frittling voltage). In a later stage of degradation, an arcing voltage due to bounce phenomena was detected at about 12V. This short arc, observed for the first time in the fretting area under power could accentuate the wear and fretting degradation process on power connectors.

Although many studies have been done for fretting corrosion based on exhausted experiments, it is a very difficult task to develop models to predict contact resistance behavior under fretting corrosion. In 1994, Bryant [29] developed a comprehensive model to predict the contact resistance during the n th fretting cycle and the ultimate usable lifetime of the contact. Different aspects such as contact wipe, fretting vibration amplitude and frequency, contaminant chemistry, material properties, plating thickness, asperity deformations, normal load, electrical load, and surface topography were considered in this model. It was based upon two corrosive fretting failure mechanisms: one involving the filling of surface valleys with wear debris generated by fretting while the other one involving the contamination of surface asperities by the corrosion product. Both showed estimates that were within an order of magnitude of the observed values for fretting tests and field failures. The model assumed that as fretting motions pull the exposed corroded asperities back together, a mismatch in size occurs and some of the corrosive products are scraped off and deposited in the valleys. Eventually, the valleys are filled and the a-spots are separated, resulting in ultimate failure. In contrast, a material balance between the amounts produced and scraped off was used to estimate the amount of corrosive product dragged into the contact. Shifting of molecules via plastic deformation mixes particles of corrosive product into the asperity metal. This model calculated the amount of corrosive product produced on the exposed surfaces during the

separation phase of a cycle of fretting. Assumptions that correlate mixing to plastic flow and the use of modern composite theory led to an estimate of the conductivity within the contaminated asperity. Integration over the asperity volume gave the asperity resistance, and then Greenwood's theory was used to estimate the total contact resistance.

In the early 1990s, Malucci [30][31] refined and combined two previously developed models dealing with contact resistance and oxide build-up under fretting conditions respectively into a single analytical model. This model was then used to predict the average effects of contact force and fretting amplitude on contact degradation. The results from fretting tests on specially prepared tin plated contacts were explained within the framework of this model. This study found that decreasing contact force or increasing fretting amplitude produced increased degradation and this was explained in terms of an increase in oxide buildup due to either asperity deformation (lower forces) or an increase in the number of asperity deformations per cycle (longer fretting amplitude). In addition, the data from thermal shock experiments were analyzed to determine the relationship between the temperature swing (ΔT) and acceleration factor. He concluded that the assumed connection between the temperature swing and fretting amplitude was consistent with both the fretting probe data and the thermal shock tests. These results provided a basis for modeling the degradation rate in terms of fretting cycles and the temperature swing. Consequently, this model was developed sufficiently to estimate the acceleration factor for a given set of laboratory test parameters to simulate field degradation.

As mentioned in Chapter 1.2, the finite element method is widely used in engineering including fretting corrosion area. For instance, in 1996 Villeneuve et.al [32]

from the Ford Motor Company used FEA to simulate the terminal crimping process for a vehicle connector. In this study, the terminal grip cross section, the punch tooling and the wire strands were modeled. The grip was forced into the punch while sitting on an anvil, mimicking the real life application. The results of the study showed that the friction between the grip surface and the punch surface is crucial to the formation of a “good” crimp. The model also showed that the crimping process is a combination of both the plane stress and plane strain conditions. In 2005, Monnier et.al [33] used finite element analysis to simulate the behavior of a sphere-plane electrical contact when a high current flowed through it, taking into account the mechanical, electrical and thermal coupling involved. Several analytical expressions were used in the simulation and the model validity was confirmed by experimental results. The simulation also gave the contact terminal voltage, the contact resistance of the system and the solid temperature, which are impossible to measure experimentally.

In 2008, Jackson et.al [34] provided a multi-physics (structural, electrical and thermal) finite element model of the bulk region of an electrical connector. This model was developed based upon a multi-scale sinusoidal rough surface (MSRS) contact model using a MATLABTM code that communicates with ANSYSTM. The resulting coupled multi-physics connector model was then used to analyze the performance of the connector under certain current range. Finally, the result showed that there was a significant proportional rise in voltage drop and temperature across the bulk regions of the connector parts. Therefore, it is proved that this coupled multi-physics model together with the MSRS model had greater accuracy in the prediction of contact forces, electrical contact resistance (ECR) and thermal contact resistance (TCR).

Currently, many universities and companies around the world are conducting important research on electrical contacts. These universities include Auburn University, Drexel University, Georgia Institute of Technology, Pennsylvania State University, University of Florida, University of North Carolina, University of Maryland (USA), Beijing University of Posts and Telecommunications, Beijing University of Technology, Harbin Institute of Technology, Huazhong University of Science&Technology, Xi'an Jiaotong University(China), the University of Manchester, the University of Southampton (England), Uppsala University, Linkoping University (Sweden), the University of Rennes (France), Vienna University of Technology (Austria), the University of Aarhus (Denmark), Nanyang Technology University (Singapore), Tver State University of Technology (Russia), the University of Tokyo, Keio University, Ishinomaki Senshu University, Keio University, Mie University, Nippon Institute of Technology, Shizuoka University (Japan), and so on. The large companies and research centers include Eaton Corporation, Molex Incorporated, AMI Doduco, Checon Corporation, Chugai USA, Rockwell Automation, MOOG Components Group, Delphi Research Labs, Sandia National Laboratories, and so on. The research fields covered include arc materials [35] , arc interruption [36], power [37] connector fretting corrosion [38], modeling [39] MEMS in contacts [40], fundamental research [41], sliding [42], automotive contacts [43] and safety issues [44].

CHAPTER 2 A STUDY OF VIBRATION-INDUCED FRETTING CORROSION IN A SINGLE BLADE/RECEPTACLE CONNECTOR PAIR

2.1 Introduction

Fretting corrosion is generally recognized as one of the major failure mechanism for electrical connector systems. The importance, necessity, history and current status of fretting corrosion study have been introduced in chapter one. At present, most evaluations of the fretting propensity of particular connector designs and the influence of variations in those designs on fretting performance are conducted through exhaustive experimental testing, which requires a major commitment of time and resources. Thus, a simulation-based method for a single blade-receptacle connector pair would therefore be of great value to those working on connector design and applications. In 2002, Flowers and Xie investigated a series of interesting behaviors on the topic of vibration-induced fretting degradation, especially a threshold vibration level for the onset of fretting and a strong relationship between vibration amplitude (beyond the threshold level) and the rate of resistance change[26][38][45]. The present study is the next step of this effort.

The main objective of this study is to develop and validate a methodology using modeling and simulation technology to predict the influence of various design factors on vibration-induced fretting propensity in electrical contacts. The procedure seeks to use finite element models for the connector system to relate the actual dynamics of the contact interface to the threshold vibration levels required for the onset of fretting and the

relative motion transfer function. Xie et.al [45] developed a two dimensional (2-D) model in ANSYS based on the typical single blade/receptacle connector pair configurations and the model was then adjusted and utilized for the evaluation of fretting propensity of this connector system by the author. A series of simulations of relative motion transfer functions and threshold levels were performed on this model as a function of excitation frequency, wire tie-off length, supplementary mass, interface friction coefficient and contact normal force. Corresponding experiments were also conducted to validate and test the simulation methodology. Finally, the results from the simulation are introduced and compared with the results from the experiment. All the details of this work are described in the sections below.

2.2 Experimental Configuration

2.2.1 Experimental Samples

A typical type of single blade/receptacle connector pair is used in this study. As shown in Figure 2-1, the sample basically consists of two parts: the blade part on the left and the receptacle part on the right. Inside the receptacle part, there is a spring component connected to the top front inner layer of the receptacle. A gap exists between the end of this spring and the inner layer of the bottom of part. When the blade is inserted into the receptacle as shown in Figure 2-2, because the height of this gap is less than that of the blade, the spring is forced to bend and generate the contact force, forming the contact pair.

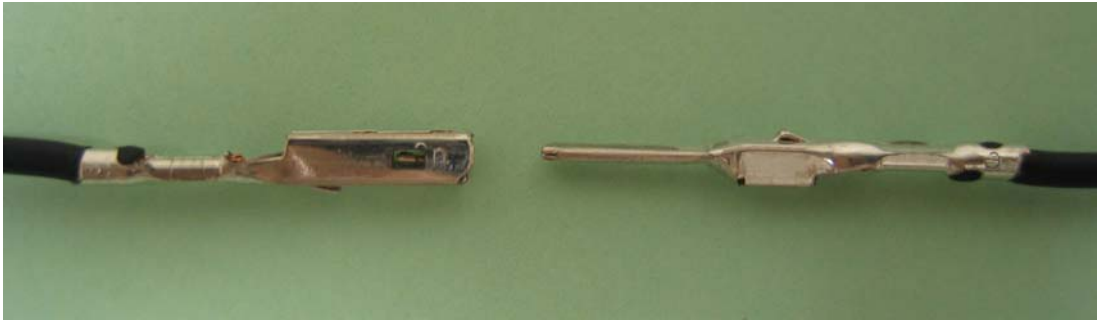


Figure 2-1: Photograph of the blade and receptacle parts



Figure 2-2: Mated blade/receptacle pair

In order to investigate the influence of different friction coefficient and contact normal forces on the fretting propensity, six different types of samples were used in total. Table 2-1 summarizes the basic sample descriptions. Both finish type 1 and finish type 2 were based upon tin deposits, with the type 2 finish having been modified to reduce the coefficient of friction (from 0.55 to 0.33) and the corresponding insertion force. In each finish type, three different gaps sizes (0.53mm, 0.48mm, 0.43mm) of the receptacle parts were used to represent different contact normal forces.

Table 2-1: Different types of experimental samples

Specimen Type	Finish	Gap Size (mm)	Normal Force (N)	Friction Coefficient
1.a	1	0.53	4.7	0.55
1.b	1	0.48	6.0	0.55
1.c	1	0.43	6.5	0.55
2.a	2	0.53	4.3	0.33
2.b	2	0.48	5.3	0.33
2.c	2	0.43	6.3	0.33

2.2.2 Experimental Equipment

The experimental equipment used in this study include a Keithley Model 2010 multimeter, which is used for the measurement of connector resistance values; Polytec laser vibrometers systems, which measures the displacements of the selected locations on connector samples; an HP 35665A dynamic signal analyzer, which could generate different types of excitation signals (such as random noise, sine wave, etc) for the shaker and analyze the frequency response; a vibration system, which consists of a Dactron vibration control system, a PA500L Amplifier and a V408 Shaker. The details of these major components are described below.

2.2.2.1 Keithley Model 2010 Multimeter

The Model 2010 is a 7^{1/2}-digit high-performance digital multimeter. It has 0.0018% 90-day basic DC voltage accuracy and 0.0032% 90-day basic resistance accuracy [46]. During the testing, the multimeter was working in four-wire mode with a resistance measurement range of 1 $\mu\Omega$ to 120M Ω .

Moreover, the dry circuit method was introduced as shown in Figure 2-3. It is a typical type of low resistance measurement method which is made on contact devices

such as switches and relay contacts. The purpose of this method is to determine whether oxidation has increased the resistance of the contacts. If the voltage across the contacts during the test is too high, the oxidation will be punctured and render the test meaningless. Therefore dry circuit testing limits the voltage across the DUT to 20mV or less.

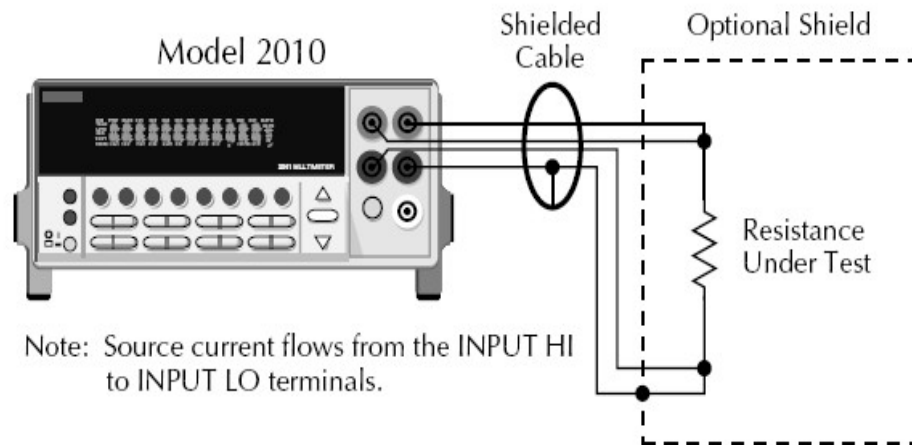


Figure 2-3: Four-wire dry circuit resistance measurement

2.2.2.2 Polytec Laser Vibrometer System

As shown in Figure 2-4, the Polytec laser vibrometer system was used in the experiment for the non-contact displacement measurements [47]. The system consists of two Polytec OFV 353 sensor heads (lasers), two Manfrotto tripods to hold the lasers and two Polytec OFV 2610 controllers. The system provides the means for a displacement measurement according to the fringe counter principle. An analog voltage signal is available at its output that is proportional to the vibration amplitude of the measurement object. This signal can be visualized with an oscilloscope or can be entered into a data acquisition and processing system, such as the HP 35665A dynamic signal analyzer. Table 2-2 shows its displacement decoder specifications.



Figure 2-4: Photograph of the Polytec laser vibrometer system

Table 2-2: Displacement decoder specification of the laser vibrometer system

Measurement Range	Full Scale Output (Peak-to-Peak)	Resolution	Max. Vibration Frequency	Max. Velocity	Max. Acceleration
$\mu\text{m/V}$	mm	μm	kHz	m/s	g
20	0.32	0.08	20	1.6	20,000
80	1.3	0.32	20	1.6	20,000
320	5.2	1.3	20	1.6	20,000
1280	20.5	5	20	1.6	20,000
5120	82	20	20	1.6	20,000

2.2.2.3 HP 35665A Dynamic Signal Analyzer

The picture of HP 35665A dynamic signal analyzer is shown in Figure 2-5. It is a two-channel fast Fourier transform (FFT) spectrum/network analyzer with a frequency range that extends from 0.19531 Hz to 102.4 kHz in the single channel mode and from 0.097656 to 51.2 kHz in the two channel mode [48]. The analyzer has a built-in signal source providing random noise, burst random noise, periodic chirp, pink noise, and fixed sine. Measurements can be saved to an internal 3.5-inch flexible disk drive, or an external

HP SS-80 disk drive, or can be directly printed out. The main characters of this analyzer used in this study are listed as below:

Input Noise Level: < -140 db

Full Span FFT Noise Floor: < -76 db (-85 db typical)

FFT Cross-Channel Gain Accuracy: ± 0.04 db (0.46%)

FFT Cross-Channel Phase Accuracy: ± 0.5 degree

Minimum Frequency Resolution: 122 μ Hz (Two Channel Mode)



Figure 2-5: Photograph of HP 35665A dynamic signal analyzer

2.2.2.4 Vibration System

The vibration system used in this study consists of a PA500L Amplifier and a V408 Shaker, as shown in Figure 2-6 and Figure 2-7 respectively. The shaker is vibrating vertically and a set of fixtures are designed and attached on the shaker for the experimental setup.

The configuration of the vibration control system is shown in Figure 2-8. The vibration system generates time-domain signals that contain the required frequency-domain characters or profile and sends them to the amplifier. The powerful amplified signal, with a larger current and voltage, then drives the shaker to vibrate. The accelerometer mounted on the payload senses the vibration on the shaker and converts it into an electrical signal, which is sent back to the vibration control system. The vibration control system deals with this time-domain signal and transfers into the frequency domain by FFT. The control system then compares the frequency-domain characteristics of this signal with the original setting. If they are different, the vibration control system will adjust its output signal accordingly. This process repeats until the frequency-domain characteristics of the signal on the shaker match the required characteristics specified by the original setting.



Figure 2-6: PA 500L amplifier

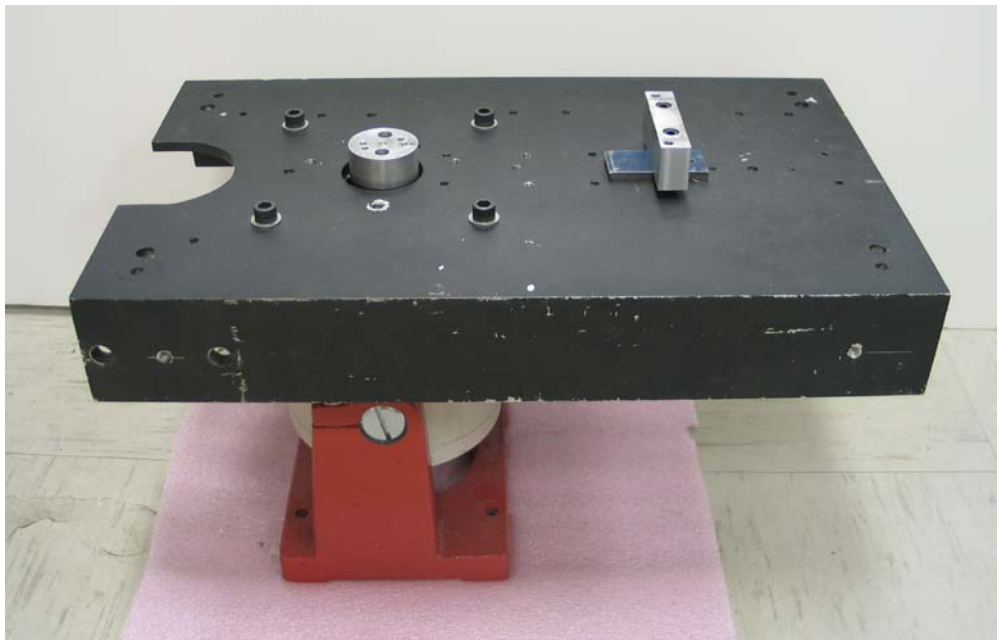


Figure 2-7: V408 shaker

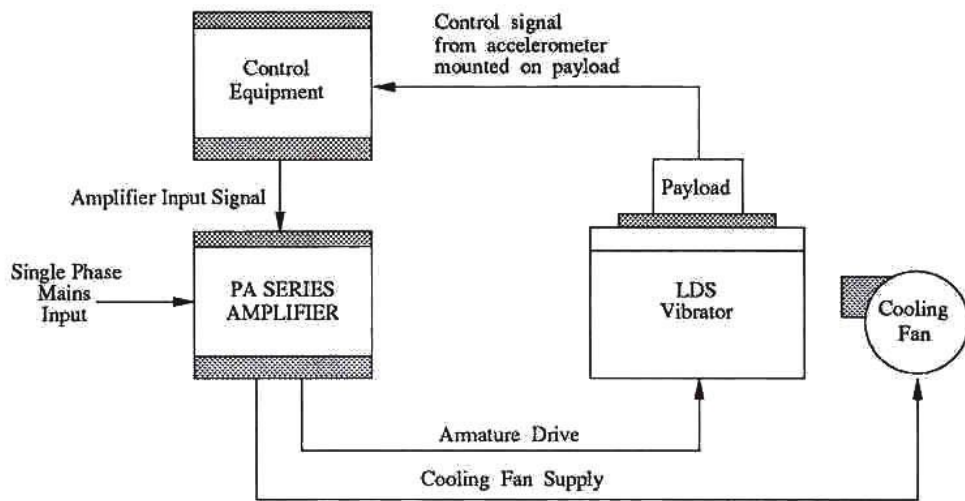


Figure 2-8: Typical vibration system

2.2.3 Experimental Setup

Two different types of experiments were conducted in this study. One is the transfer function measurement and the other one is the fretting threshold (resistance change) measurement. Details of the two experimental setups are described in the following sections.

2.2.3.1 Transfer Function Measurement

It is generally agreed that relative motion between contacting terminals is the root cause of fretting corrosion. Flowers, et.al.[38][45][51][52] provides a description of the electrical measurement methods and test procedures for determining fretting thresholds and transfer functions. The transfer function for each sample is determined by comparing the output vibration response at the connector interface to the input excitation at the vibratory shaker head. The ratio of the steady-state output amplitude to the input amplitude for a given excitation frequency is the magnitude of the transfer function at that frequency. The phase difference between the steady-state output and input responses for a given frequency is the phase of the transfer function at that frequency.

From a dynamic modeling perspective, a transfer function is a functional relationship, in the frequency domain, between the magnitude (M) and phase (θ) of an input motion and the corresponding output motion. For example, a transfer function magnitude of 1 and zero phase shift indicates that there is no relative motion between the respective input and output measurement points. Similarly, a transfer function with a magnitude of 2 and a 45° phase indicates that the output motion is twice as large as that of the input and that it lags the input response by 45° . For most dynamic systems, there is a peak magnitude for input excitations at one or more of the resonant frequencies.

Typically, the phase shift is small for low frequency excitations and increases dramatically as the driving frequency approaches and exceeds the primary resonance value. Another way of thinking of the transfer function is in terms of a complex number where the real part is $M \cos(\theta)$ and the imaginary part is $M \sin(\theta)$. Therefore, the transfer function can be expressed by the following equation:

$$\text{Transfer Function} = M \cdot \cos(\theta) + i \cdot M \cdot \sin(\theta) \text{ or } M \angle \theta \quad (1)$$

Based on the above transfer function, the relative motion between the two-half interfaces is defined by:

$$Z_F = \sqrt{[1 - M \cos(\phi)]^2 + [M \sin(\phi)]^2} \quad (2)$$

where Z_F is the relative motion, and $M \cos(\theta)$ and $M \sin(\theta)$ are the real part and imaginary part of the transfer functions, respectively.

Figure 2-9 shows the basic setup of the transfer function measurement for the blade/receptacle connector pair. Because the front-half connector interface is fixed at the shaker head, its input displacement is the same as for the shaker head. Therefore the reflector for the input measurement was taped on the top of blade right next to the receptacle after mated while the output reflector was taped on the top of the receptacle, as shown in Figure 2-10. A wire leads 230mm in length was attached to the receptacle samples those were to be tested. A group of three steel balls was attached to the wire lead by using the heat shrink tube to serve as a supplementary mass to lower the natural frequency and increase the fretting propensity of the system. Without the addition of the supplementary mass, it was very difficult to impart sufficient energy to the system to produce fretting. These small diameter (2.5mm diameter) steel balls were attached to the wiring lead 13.0mm from the junction with the receptacle. The blade to be tested was

firmly attached to the shaker head with a clamp, as shown, while the receptacle was mated to the blade, with the other end of the wire lead clamped to a fixed (non-vibrating) table. Vertical driven motion (random noise) was input to the shaker head. The displacement of the blade and receptacle were then measured using the non-contacting laser displacement measurement system as described in the previous section.



Figure 2-9: Experimental setup of the transfer function measurement

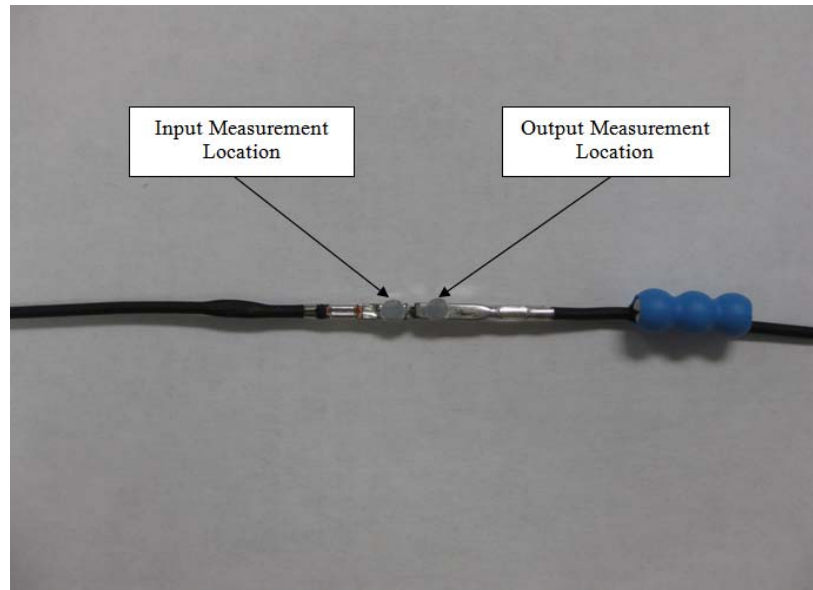


Figure 2-10: Detailed view of displacement measurement

2.2.3.2 The Fretting Threshold Level Measurement

The setup of the fretting threshold level measurement is shown in Figure 2-11 and Figure 2-12. The blade and receptacle are clamped the same way to the shaker table as in the previous transfer function testing. In order to measure the resistance of the connector pair and minimize the effect of magnetic field, the electrical wire in the receptacle part was clamped in the fixture while the other wire connected in the blade part was bent and secured to the top of the fixture the shaker table. Another reason of putting the both ends of the electrical wire close is because the four gator connectors and measuring wires of the multimeter should be placed closer so that the wires could be plaited together to minimize the circuit loops. Sinusoidal signals were generated from the control system, and the real-time resistance change was then observed and recorded by a computer system with a Labview program.

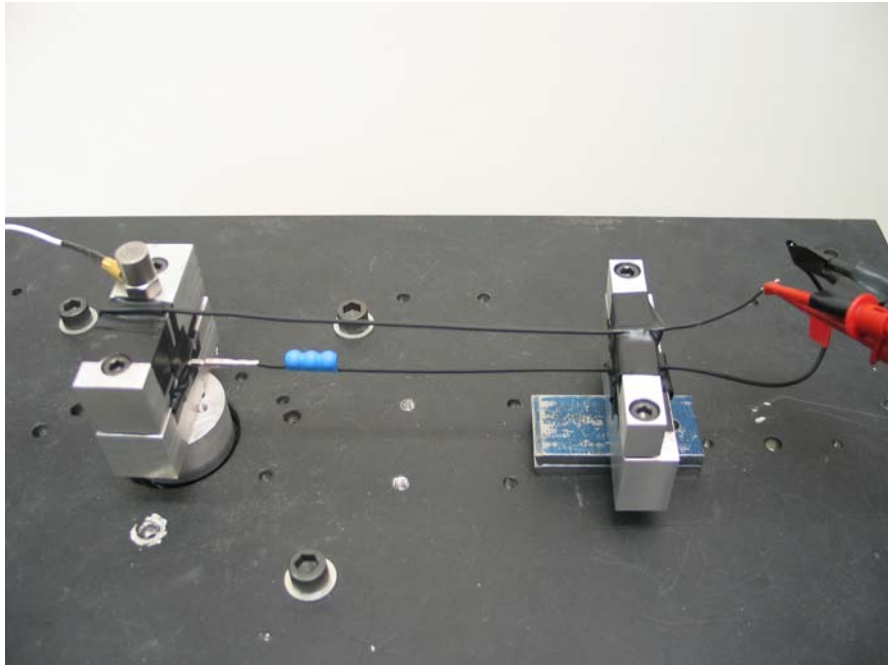


Figure 2-11: Photograph of the fretting threshold levels experiment setup

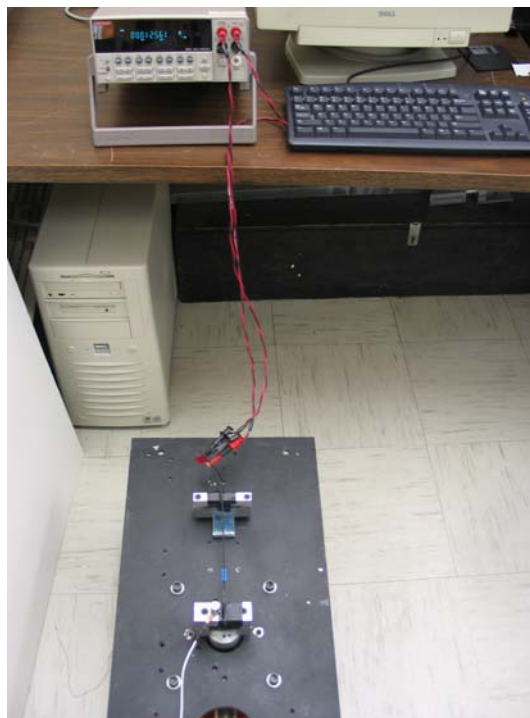


Figure 2-12: Photograph of the resistance measurement

2.3 Finite Element Model

An ANSYS [11] finite element simulation model was developed based on the same samples and experimental configurations as those introduced in the previous part of this chapter. A two-dimensional (2-D) simplified model was used in order to reduce the number of elements and increase simulation speed. The geometric model was generated according to the detailed CAD drawings of the single blade/receptacle connector pair with proper material properties which were first measured from the real experiment and then adjusted according to the 2-D geometry. Different mesh controls for mesh convergence and simulation precision were assigned to the different parts of the model depending on its geometry and importance. Two simulation methods, harmonic and transient simulation, were utilized to simulate the transfer function and fretting process respectively. Details of the modeling study are described in the sections below.

2.3.1 Geometric Model

The 2-D model was generated to simulate the real single blade/receptacle connector pair configuration in the experiment. The dimensions of the geometric model followed those of the real blade/receptacle sample, wire and balls used. Figure 2-13 and 2-14 show the overall view and a close-up view of the 2-D model, respectively. In Figure 2-13, the blue part on the left represents the blade; the cyan part on the right represents the receptacle and its leading wire; the yellow parts on top of the wire are the supplementary balls. Detailed geometry of each part is shown in Figure 2-14. The 2-D model consists of seven parts in total: blade, U-bend, cantilever beam spring, receptacle (outer structure), crimp, supplementary mass and wire.



Figure 2-13: Overall view of the 2-D geometric model

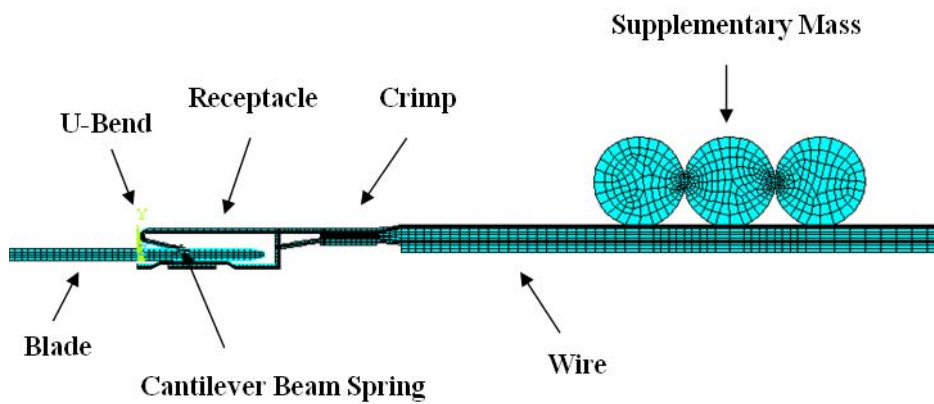


Figure 2-14: Close-up view of the 2-D geometric model

As just mentioned before, most of these geometric parts are used exactly the same dimensions as the real components besides the outer structure of the receptacle. The real outer structure of the 3D receptacle was composed of four metal pieces and served as a “box” for the blade to be inserted into. Both the annulus and the spring component are inside the box. Obviously, the metal pieces on the two sides of the receptacle can restrict the displacement of the upper and bottom pieces in the reality. However, for the limitation of 2-D plane model, these two pieces on both sides cannot be included. Therefore, the stiffness of the outer structure of the receptacle was adjusted to be

significantly high in order to fix the two sides as that of real situation. Therefore the Young's modulus of the outer structure was set to a very large value.

As shown in Table 2-3, most thickness values of the components in the geometric model are the same as those of the real parts. However, 1.12mm was not the real thickness of the wire. This is because when the thickness value was applied to the wire, it would generally extrude according to the thickness value and thus the cross section of the wire would be a rectangle instead of a circle. Due to this geometric change, it is important to make sure that the $I_{\text{equivalent}} * E_{\text{equivalent}}$ for the 2-D wire model was equal to the $I_{\text{real}} * E_{\text{real}}$ for the real wire, where I is the wire's inertia moment (a function of its dimensions) and E is its Young's modulus. This requirement resulted in the 2D wire being assigned a thickness of 1.12mm.

Table 2-3: Material and dimensional properties of the model components

Components	Thickness	Density	Modulus of Elasticity
Blade (portion inside the receptacle)	1.5 mm	8910 kg/m ³	130 GPa
Blade (portion outside the receptacle)	1.5 mm	6974 kg/m ³	130 GPa
U-bend portion of the cantilever beam	1.9 mm	8910 kg/m ³	130 GPa
Cantilever beam spring in the receptacle	1.5 mm	8910 kg/m ³	130 GPa
Receptacle (excluding spring member) and part of wire under the crimp	2.6 mm	8794 kg/m ³	130 GPa
Wire portion outside the crimp	1.1 mm	4564 kg/m ³	96.5 GPa
Supplementary mass (balls)	2.6 mm	12,876 kg/m ³	195 GPa

2.3.2 Material Properties

The values of material properties used in the 2-D model are also shown in Table 2-3. Due to the changes of dimensions of thickness of certain parts, the material properties of each component were adjusted to the corresponding values from the real connector samples to ensure the correct functioning of the model. The density of the blade, receptacle and balls remained the same as the real values because that they has the same weights as their real world counterparts. The weights and the volume of some other components had also changed, particularly the outer structure of the receptacle and the wire. Hence, their densities also had to be adjusted to match the weights of the original samples in experiments.

As mentioned in the previous section, the Young's modulus for the outer structure of the receptacle was set to a very large value to constrain this structure (excluding the annulus and spring inside the receptacle) from deforming when the blade was being inserted into the receptacle. A series of initial simulations have been performed to select the necessary Young's modulus value. The results revealed that this value had to be increased to 1000 times larger than the original value to obtain the same function.

2.3.3 Boundary Conditions

The boundary conditions applied to the 2-D model were set up to match the real conditions with respect to the experimental configuration and vibration. As shown in Figure 2-11, the blade was clamped on the shaker head and the end of the wire (which was attached with the receptacle) was also clamped onto the fixture. During the vibration, the blade and the shaker head moved back and forth vertically (along the y-axis in the 2-D model) as a sinusoidal driven motion. Consequently, in the 2-D model, the end of the

wire was fixed in all degree of freedom while the end of the blade was constrained in x-axis and z-rotation to vibrate only in the y-axis. A sinusoidal function was utilized to the y-axis motion to simulate the real vibration process. Each vibration cycle was evenly divided into forty small substeps to ensure the accuracy of the simulation analysis. Moreover, the small substep intervals made it easier to obtain the solving convergence. No restraint was needed on the receptacle in both experiment and simulation. Figure 2-14 and Figure 2-15 show all the boundary conditions assigned to the 2-D model and the profile of the sinusoidal vibration excitation with the load substeps respectively.

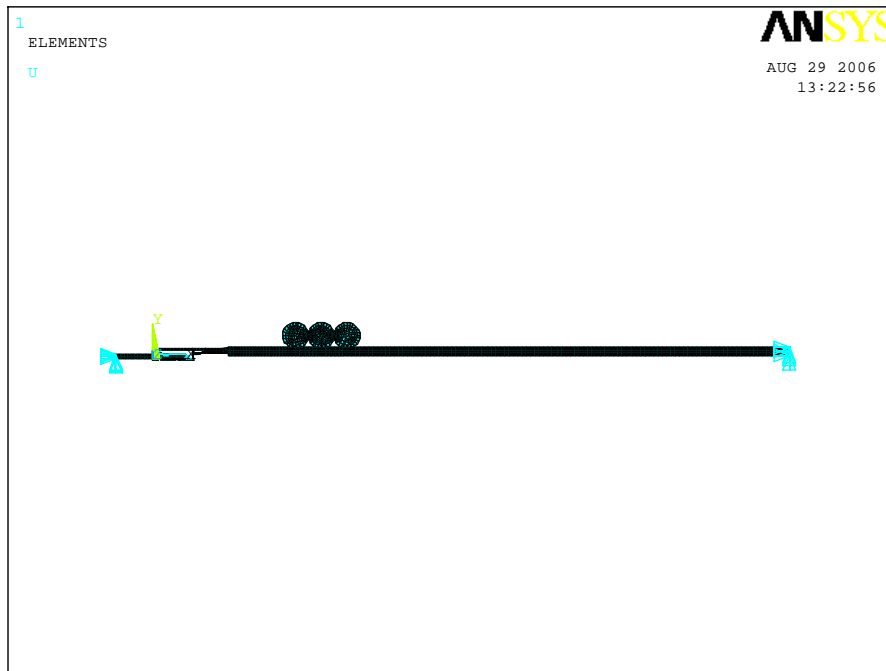


Figure 2-15: Geometric model for the blade/receptacle configuration

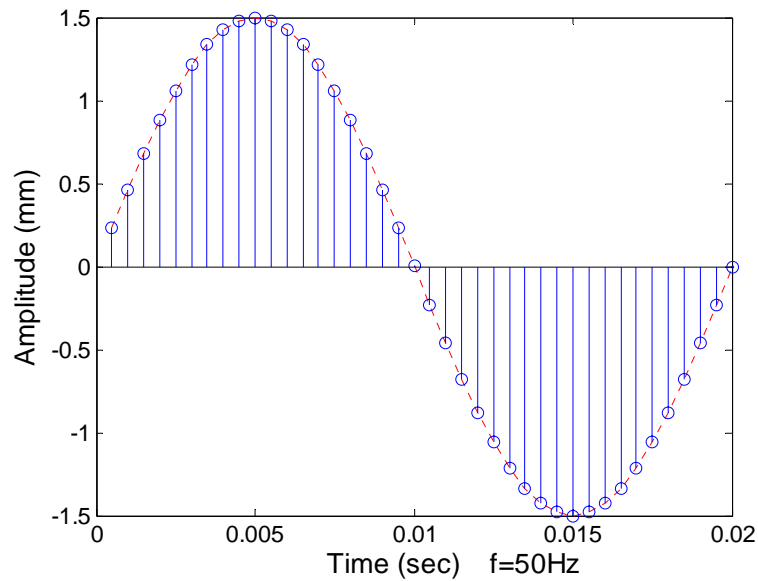


Figure 2-16: Sinusoidal vibration excitation with the load substeps

2.4 Vibration Process Simulation

As shown in Figure 2-17, the excitation of the sinusoidal vibration at the blade produced motion in the wires and the supplementary mass (balls). In turn, that motion caused motion of the receptacle and at the connector interface. Figure 2-18 and Figure 2-19 show the motion of the receptacle, which clearly indicates that the receptacle rocks (rotates), rather than simply sliding along with the blade. Therefore, rocking was found to be the main mode for the receptacle's motion.



Figure 2-17: Full model motion at Time 1 during vibration

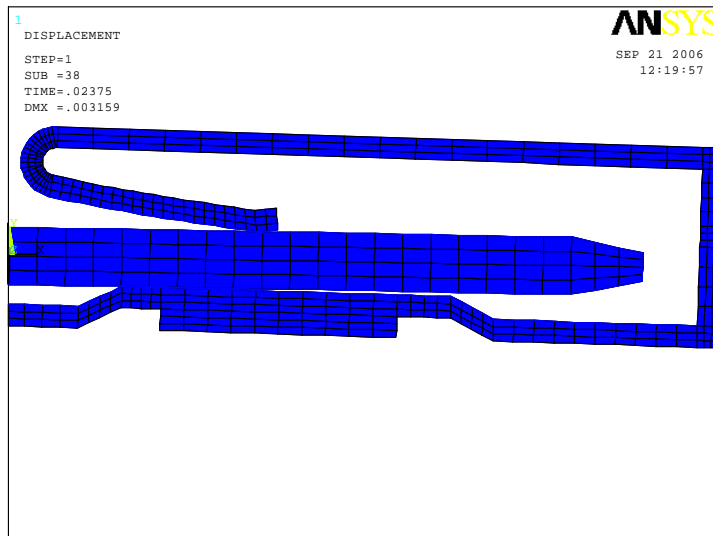


Figure 2-18: Motion of the blade and the receptacle at time 1

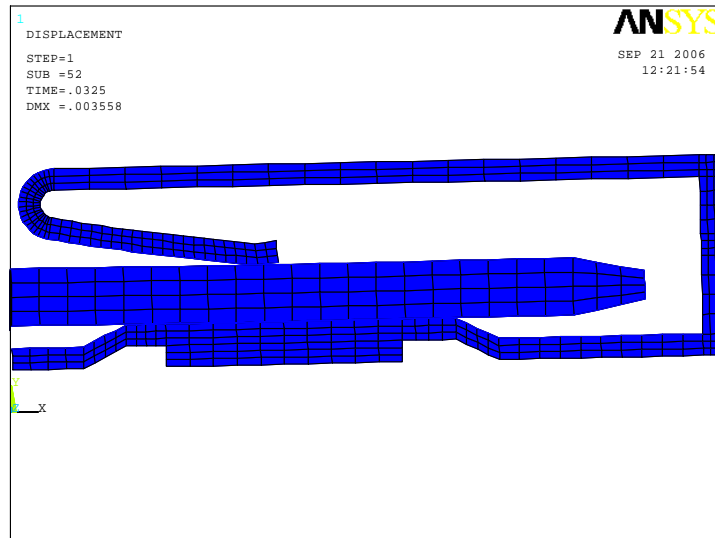


Figure 2-19: Motion of the blade and the receptacle at time 2

2.5 Experiment and Simulation Results

Based on the experimental configuration and 2-D model generation described above, concurrent simulation and experimental studies were performed to evaluate the dynamic response and the threshold vibration levels as a function of excitation frequency, interface friction coefficient, contact normal force, supplementary mass and wire tie-off length. Detailed analysis of the results is discussed in the sections below.

2.5.1 Transfer Function Results

As described in section 2.2.3.1, the relative motion between the contacting sections is generally agreed to be the basic inducement of fretting degradations. Therefore the transfer function in a certain frequency domain which is recognized as the indicator of dynamic response of the system and the relative motion between contacting terminals is observed in both of the experimental and simulation studies instance. In the

transfer function simulation, the input and output measurement locations remained the same as the locations of the transfer function measurements in the experiment. In this particular model, the input location was on the node 124 (input node) and the output location was on node 743 (output node), as shown in Figure 2-19. These two nodes corresponded to the two locations where the laser spots measured the transfer function in the experiment.

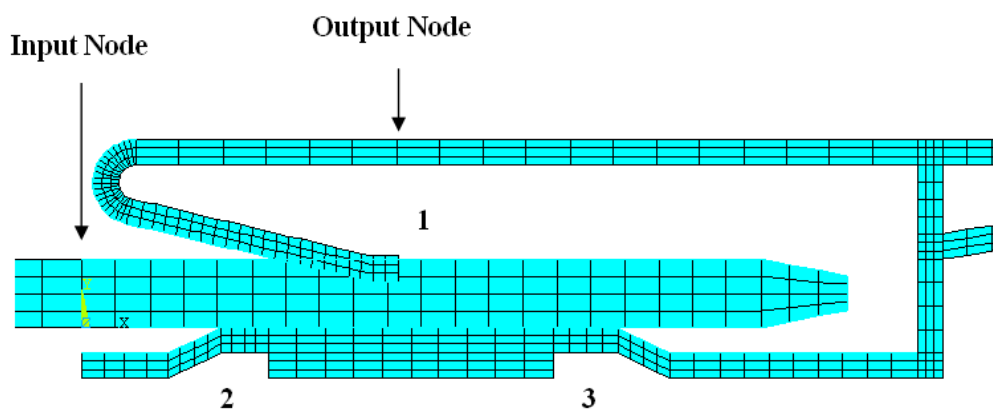


Figure 2-20: Node locations for the transfer function simulation

Example transfer functions of the Type 1.a and Type 2.a configurations for different friction coefficient (0.55 and 0.33 respectively), obtained both experimentally and using the simulation model, are shown and compared in Figure 2-21. The transfer functions generated by the 2-D model for the Type 1 and Type 2 connector finishes were very similar to each other and they generally matched the experimental measured values well, particularly for the lower frequency range (around the first resonant peak). The reason why these two types of finish contact pairs had a similar transfer function was due to the main motion mode, in other word, the first vibration mode of the receptacle being the rocking mode. This rocking motion mode minimized the effect of differences in the

friction coefficient at the contact interface due to the different surface finishes on the connectors. During the author's study, it was also observed that this mode minimized the effect of differences in the contact normal forces between the blade and the spring. As shown in Figure 2-22 and Figure 2-23, both experiment and simulation results show that the differences of overall shape and resonant peak of the transfer functions for different contact normal forces are very similar. However, it is still could be observed that the simulation results show less variation comparing with experiment results. This is because of the adjusted high stiffness of the outer structure as described in section 2.3.1.

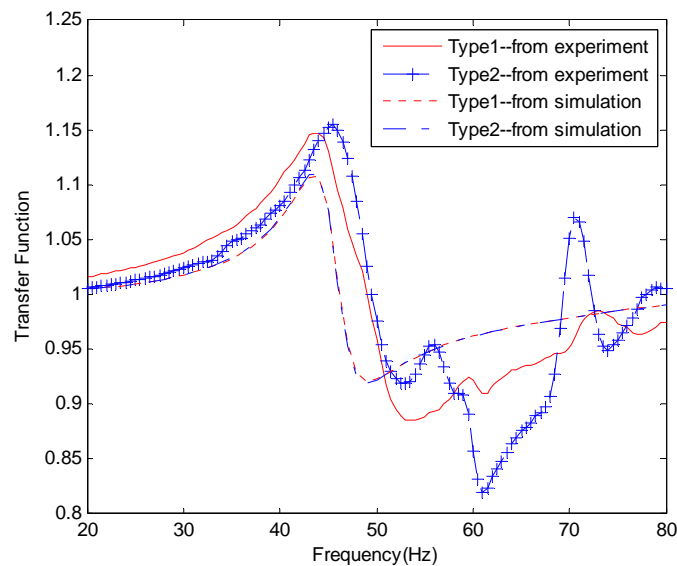


Figure 2-21: Transfer function results from experiment and 2-D model simulation for different friction coefficient

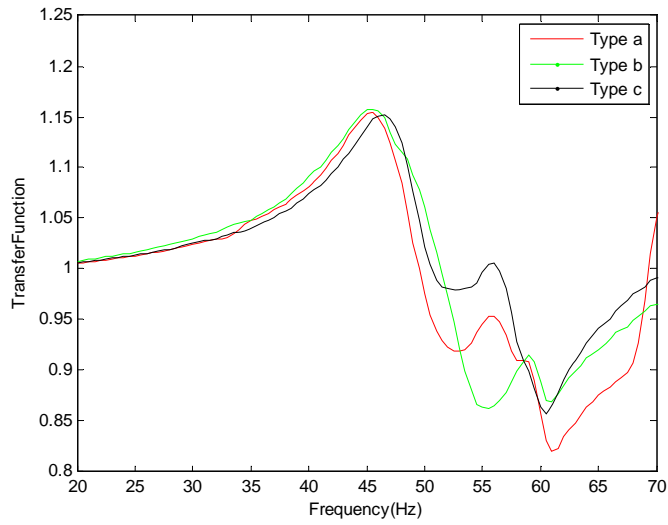


Figure 2-22: Experimental results for different contact normal force levels

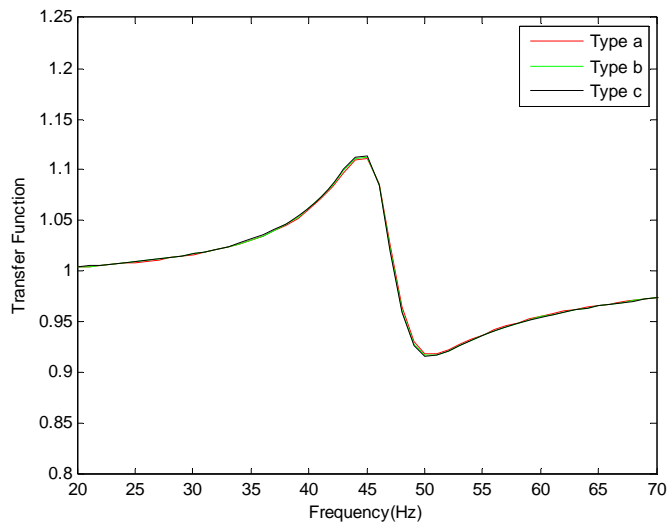


Figure 2-23: 2-D simulation results for different contact normal force levels

A series of experiment testing was performed to study the “slippage” effect of the friction at the contact interface in the experiment. Figures 2-24 and 2-25 show the transfer functions that were obtained for selected vibration amplitudes for the Type 1 and Type 2 samples, respectively. For the Type 1 samples with a higher friction coefficient,

the effect of increasing the input amplitude is clearly observable but does not tend to greatly alter the overall shape of the transfer function. The peak of the first resonant frequency did shift to the left as the increment of vibration displacement. The difference between the lowest and the highest peak amplitudes of transfer functions is about 10%. This is due to the slippage at the contact interface, which results in a somewhat longer cable length and a lower cable tension. However, for the Type 2 samples, the effect of different vibration displacements is much more dramatic as shown in Figure 2-24. These samples have a much lower contact friction coefficient compared to the Type 1 samples. The peak of the first nature frequency has a significantly larger shift than the Type 1 results. Moreover, the difference between the lowest and the highest peak amplitudes of transfer functions is about 25%. It should also be noted that, for both sample types, decreasing the amplitude below the smallest value shown (0.082 mm) did not result in any observable shifting of the resonant peak. Therefore, as one could intuitively expect, the “slippage” effect at the contact interface was generally reduced for the higher friction finish (Type 1).

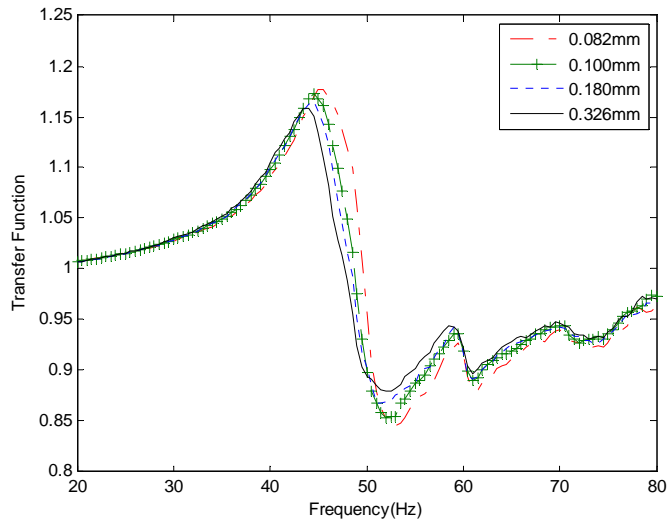


Figure 2-24: Experimental results showing the variation of transfer function with excitation amplitude for Specimen Type 1.a

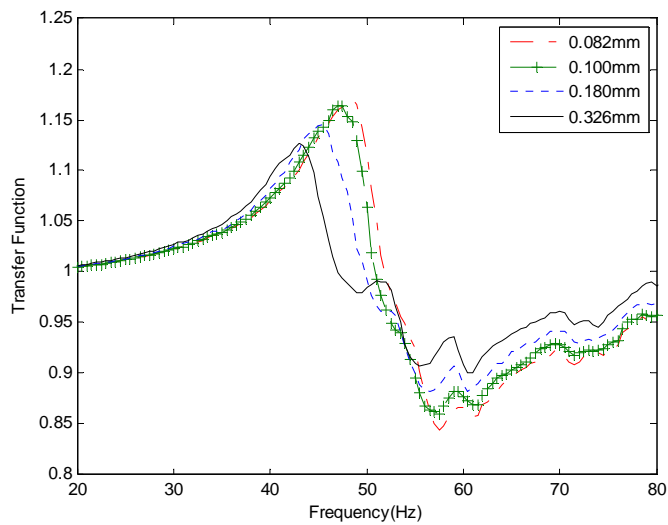


Figure 2-25: Experimental results showing the variation of transfer function with excitation amplitude for Specimen Type 2.a

As mentioned in previous sections, several simulation studies were performed with the goal of understanding the predicted effects of wire length and supplementary

mass on the behavior of the transfer function. The results are presented as relative motion transfer functions. The definition of the relative motion transfer function was discussed in section 2.2.3.1.

Figure 2-25 shows the effect of changing cable tie-off length. As the tie-off length is decreased, the resonant peak shifts to the right and tends to become somewhat higher in amplitude. This effect is due to a relative decrease in system internal damping, which comes primarily from the wiring.

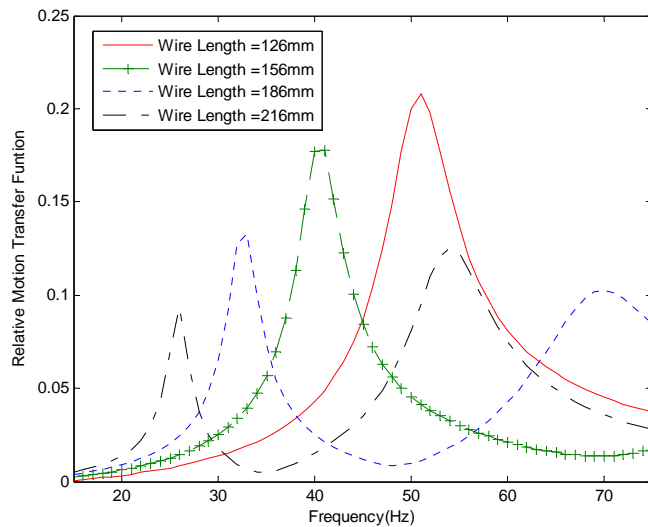


Figure 2-26: Simulation of relative motion transfer functions for various wire tie-off lengths (Specimen Type 1.a)

Figure 2-26 shows the simulation results of predicted effects of supplementary mass on the relative motion transfer function. As the supplementary mass is increased, the resonant frequency shifts to the left and the amplitude of the resonant peak increase dramatically. This trend provides an explanation for the difficulty in obtaining fretting for samples without supplementary mass. That is, the relative motion in the frequency and amplitude range of interest is too small to produce significant fretting degradation.

Substantial additional vibration energy would have to be put into that sample configuration in order to exceed the threshold levels required for the onset of fretting, as discussed by Malucci [53].

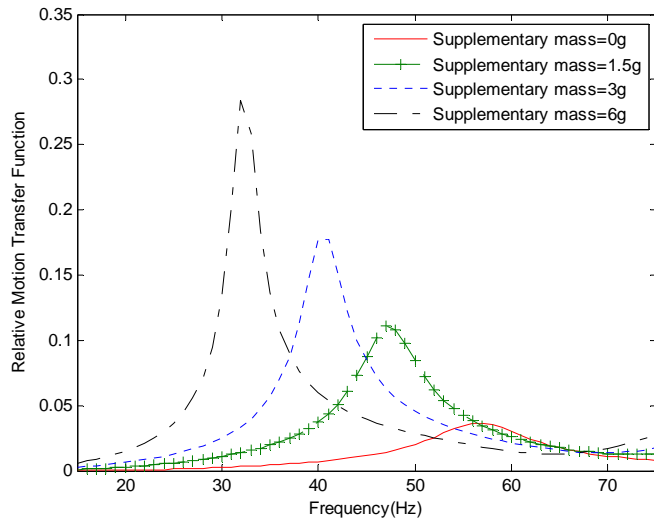


Figure 2-27: Simulation of relative motion transfer functions for various levels of supplementary mass (Specimen Type 1.a)

2.5.1 Fretting Threshold Results

The threshold fretting level for a given configuration and vibration frequency is determined by exposing samples to differing amplitudes of vibration and measuring the resistance for two minutes. For all electrical resistance measurements, the four-wire configuration was used as described in section 2.2.2.1. The resulting time trace is then visually inspected. If there is no net increase in resistance over the time period of the test, the sample is deemed to have not fretted. A fresh sample was then tested, with the vibration amplitude increased by an increment of 0.1mm and the inspection process repeated until a net increase in the resistance of greater than 5×10^{-6} ohm/sec is observed. The lowest vibration amplitude for which such a net increase in resistance is observed is

designated as the threshold g-level for that sample. For each configuration and frequency, a minimum of 5 samples are tested and the threshold g-levels averaged to obtain the nominal threshold g-level for that configuration and frequency.

By using the method described above, a series of fretting threshold experiments have been performed on all six different types of connector samples. Figure 2-28 shows an example of how the threshold displacement value was determined using the change in resistance curves. In this example, the Type 1.a samples were tested under different vibration amplitude at the frequency of 45Hz. It could be observed that below 0.8mmpk, which signifies a vibration amplitude of 0.8mm peak-to-peak at the shaker head, the trends of the resistance change curves are generally flat. Once the displacement reached 0.8mmpk, however, the trend began to rise and after 0.8mmpk, the trends continued to increase. Consequently, 0.8mmpk was determined to be the threshold displacement at the shaker head for the type1 connector with a 0.53mm gap at 45Hz. The other contact pairs were also characterized in the same way. The reason of the increase is the accumulation of Sn oxidations as described in Chapter 1.

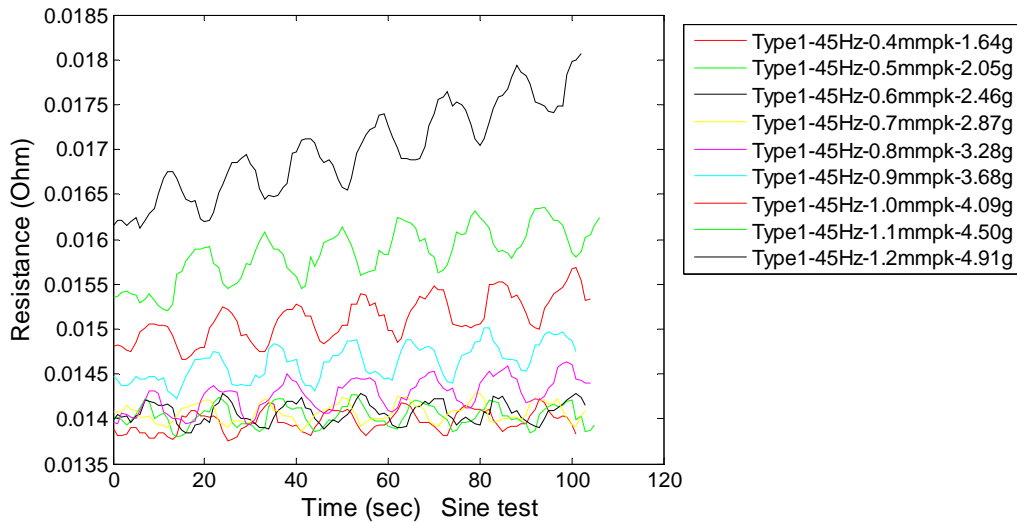


Figure 2-28: Identification of the threshold displacement (or g-level)

One interesting phenomenon observed in the fretting threshold experiments was that even for the flat resistance curves, such as curves for vibration amplitudes smaller than 0.8mm peak-to-peak, the resistance values still varied periodically like a repeated half sine wave (first 180 degrees phase). For example, for the curve Type1-45Hz-0.6mmpk, the entire trend is flat with a resistance changes in a period of roughly 10 seconds. Obviously this is not due to the changing amplitudes of vibration because the frequency of vibration is 45Hz, which is a period of about 0.022 second. Part of the reason of this phenomenon is the effects of magnetic field from the shaker. Besides that, Another possible guess to explain this phenomenon is the “build-up” and “break-down” process of the insulating Sn oxidations. According to the surface analysis, the Sn board finish is generally a combination of SnO, SnO₂, Sn (elemental), and Sn-OHx[57]. As the vibration process started, the Sn oxidations start to be worn away from the contact surfaces and accumulated at the edge. As shown in Figure 2-29, the marked spot is one accumulation area. As more and more insulating debris stacked together, the height and

volume of the accumulation generally increased which resulted in the increment of the contact resistance. This is the “build-up” process, roughly first 5 seconds of each period. However, this higher “stack” also resulted in higher contact normal forces and corresponding higher shear stress due to the sliding effect. Therefore, as the value of the shear stress reached certain critical value, the stack started to “break down” and the resistance decreased. This explains the second half of the resistance decrease period. Further study might be needed to prove this hypothesis.

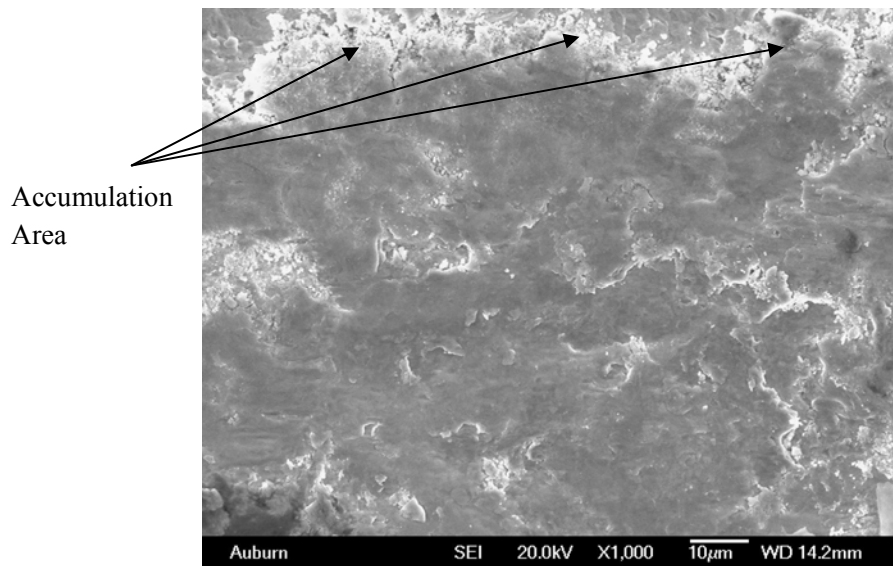


Figure 2-29: SEM picture of accumulation area

As observed in previous studies [45][51][52], the inverse relative motion transfer function is proved to be a good predictor of the variation in the threshold values with excitation frequency. The excitation frequencies, amplitudes of the relative motion, threshold displacement at the shaker head, and their product values are listed in Table 2-4 and Table 2-5 for type 1.a and type 2.a connectors, respectively. It could be observed that the products of the threshold displacement at the shaker head and the relative motion for each type of connector pairs remained generally constant. This relationship provided a

solid theoretical base for looking for a consistent indicator of the fretting threshold value simulation.

For current FEA simulation technology, it is still impossible to simulate the real-time resistance changes. Therefore, a key task in the prediction of threshold values using a simulation model is to select a relative motion indicator. In the simulation model, there will always be some relative motion at the contact interface for any input vibration level. In order to make a selection, the interface motion was examined in detail. Because of the rocking motion mode of the receptacle, three points of contact were of particular interest, as shown in Figure 2-20. Position 1 was the point of contact between the blade and the end of the spring during the vibration, Position 2 was the point of contact between the blade and the left inner bottom surface of the receptacle during the rocking motion, and Position 3 was the point of contact between the blade and the right inner bottom surface of the receptacle during the rocking motion.

Table 2-4: Relationship analysis for type 1.a connector pair

Frequency	Relative Motion (RM)	Threshold displacement at shaker head (peak)	Product of RM and Displacement
30Hz	0.0321	3.0mm	0.0963mm
35Hz	0.0696	1.4mm	0.0974mm
40Hz	0.1355	0.6mm	0.0813mm
45Hz	0.1273	0.8mm	0.1019mm
50Hz	0.1004	0.9mm	0.0904mm

Table 2-5: Relationship analysis for type 2.a connector pair

Frequency	Relative Motion (RM)	Threshold displacement at shaker head (peak)	Product of RM and Displacement
30Hz	0.0371	2.9mm	0.1076mm
35Hz	0.0826	1.2mm	0.0991mm
40Hz	0.1645	0.6mm	0.0987mm
45Hz	0.1221	1.0mm	0.1221mm
50Hz	0.0696	1.45mm	0.1009mm

Initially, the threshold displacements at the shaker head at different frequencies obtained from the experiment were used as the input excitation displacement for the real-time vibration simulation. At all position 1, 2 and 3, the x-axis relative motions for these different frequencies were very similar while the y-axis relative motions were quite different. This reflected that the fretting was only related to the x-axis (not y-axis) relative motion between the contact interfaces, as expected. Moreover, the x-axis relative motion at position 2 is larger than those at position 1 and position 3. This means the x-axis relative motion at position 2 made the largest contribution to the fretting. As shown in Figure 2-30, the x-axis relative motion vibration amplitude at position 2 was approximately 1.5 μm peak-to-peak. This value is in reasonably good agreement with the work of Hamman, et. al.[54], who reported that “Almost any slip ($>1 \mu\text{m}$) resulted in an increased contact resistance in the performed experiments,” for the particular system that was considered. It should be noted that the threshold level for a given connector system depends upon the contact material and will generally be different for different plating materials, so a somewhat different value to that reported by Hamman, et. al. [54] is not unexpected.

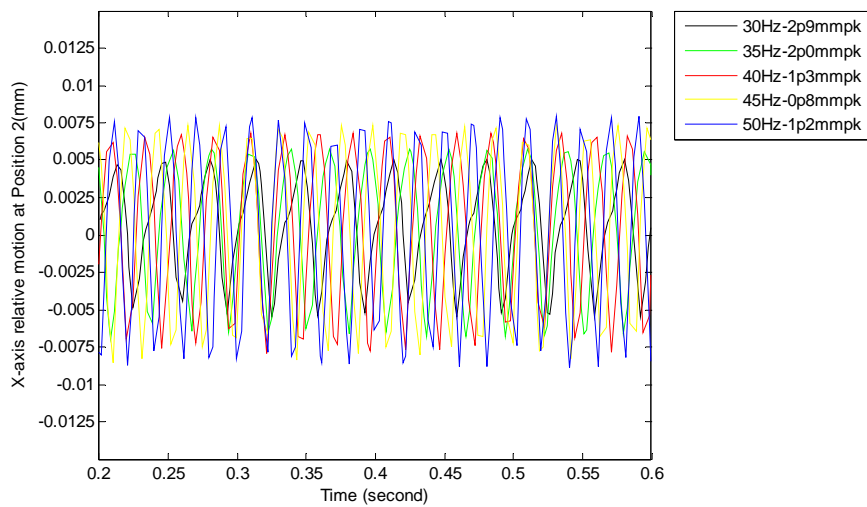


Figure 2-30: Simulated X-axis relative motion at position 2

Based on the fundamentals described above, the input excitation amplitude at a particular frequency was adjusted until the x-axis relative motion at position 2 reached the value of $1.5 \mu\text{m}$ peak-to-peak. The resulting amplitude was taken to be the threshold input level at that frequency. Both fretting threshold value experiments and simulation were conducted for different input excitation levels and the frequencies of 30Hz, 35Hz, 40Hz, 45Hz and 50Hz. The reason of choosing these frequencies is because the first resonant peak of the relative motion transfer function is around 40Hz, thus the differences between relative motions at different frequencies are more significant. Figure 2-31 to Figure 2-36 show the simulation and experiment threshold results as well as the inverse relative motion transfer functions. As expected, the inverse relative motion transfer function is a good predictor of the variation in the threshold values with excitation frequency. The threshold displacements at the frequency with lower relative motion transfer function values (roughly 40Hz to 50Hz) are somewhat lower than others. The

overall simulation threshold results generally correlated well with experiment results for all six types of connector samples.

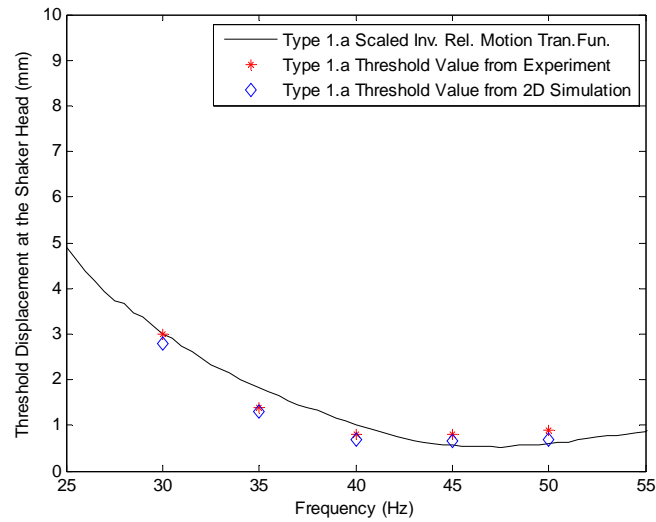


Figure 2-31: Comparison between experimental and simulation results for fretting threshold displacements of Type 1.a

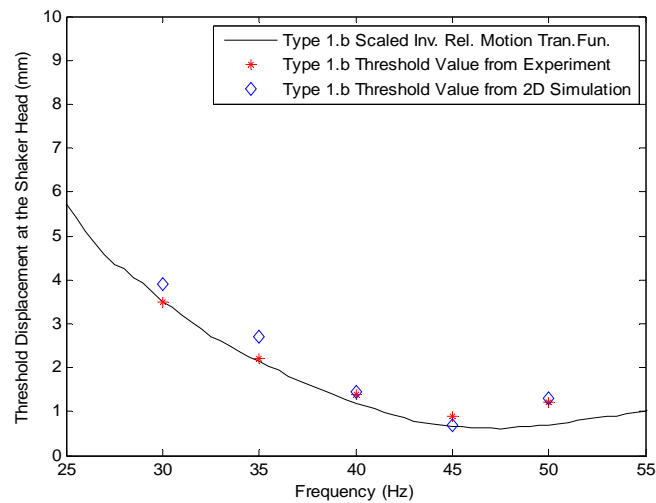


Figure 2-32: Comparison between experimental and simulation results for fretting threshold displacements of Type 1.b

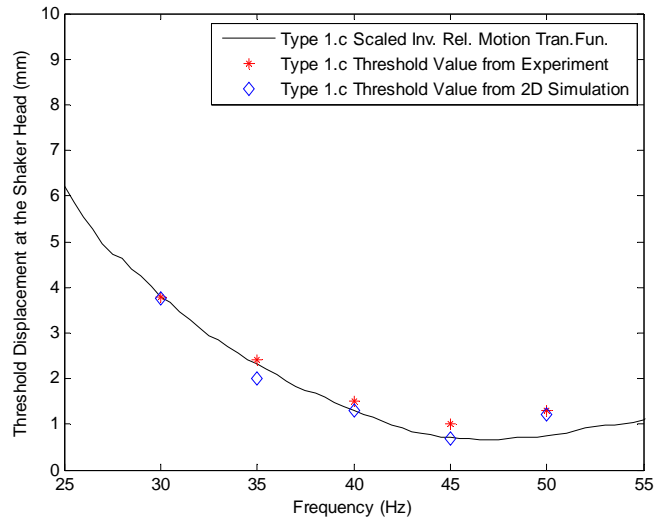


Figure 2-33: Comparison between experimental and simulation results for fretting threshold displacements of Type 1.c

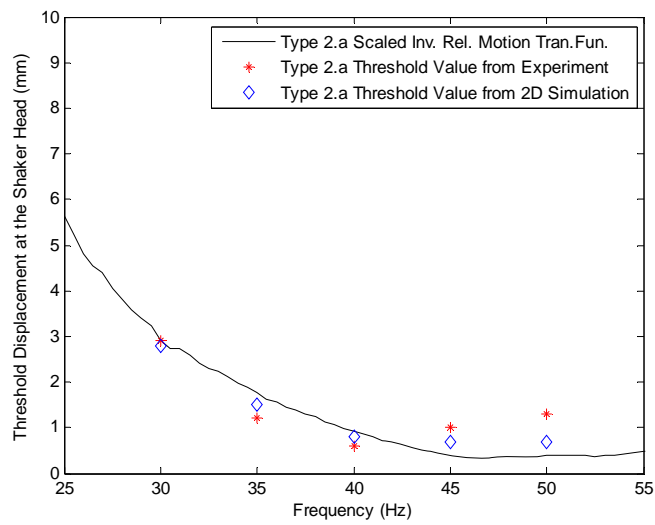


Figure 2-34: Comparison between experimental and simulation results for fretting threshold displacements of Type 2.a

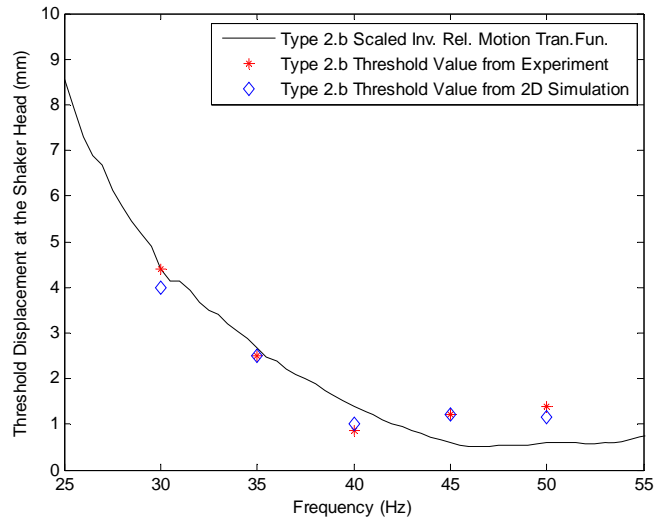


Figure 2-35: Comparison between experimental and simulation results for fretting threshold displacements of Type 2.b

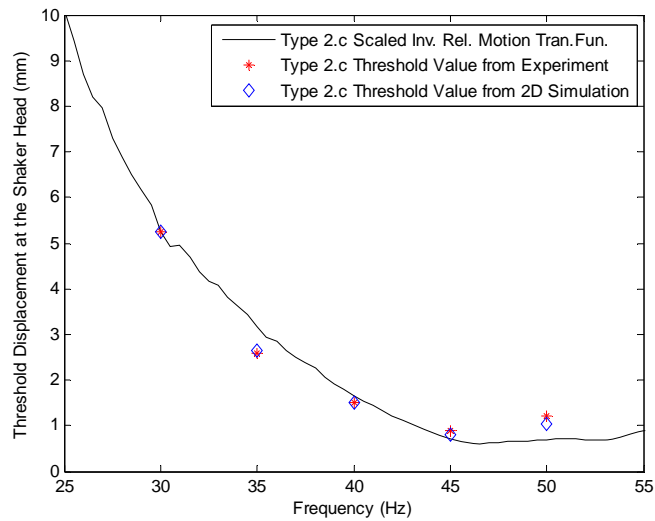


Figure 2-36: Comparison between experimental and simulation results for fretting threshold displacements of Type 2.c

One purpose of this fretting threshold study is to evaluate the influence of various design factors on vibration-induced fretting degradation. Figure 2-37 and Figure 2-38 show the differences of fretting threshold displacements for Type1 and Type 2 connector

samples with different contact normal forces, respectively. As the contact normal forces increased from Type a to Type c, the threshold values generally increased. The higher contact normal force at the contact interfaces leads to smaller relative motion between the blade and the receptacle and then reduces the insulating oxidation accumulation process at contact terminals. Therefore, higher contact normal force inhibited the fretting process and resulted in higher fretting threshold values. In addition, the fretting threshold displacements of Type 1 and Type 2 samples with different friction coefficient at contact terminals are similar. This result is with the same trend of transfer function results. Each is due to the minimized effect of “rocking mode” as described in previous sections.

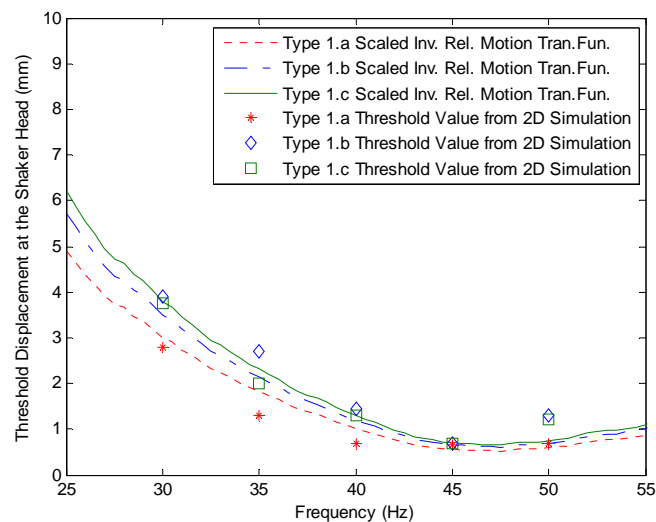


Figure 2-37: Comparison of fretting threshold displacements for Type 1 samples with different contact normal forces

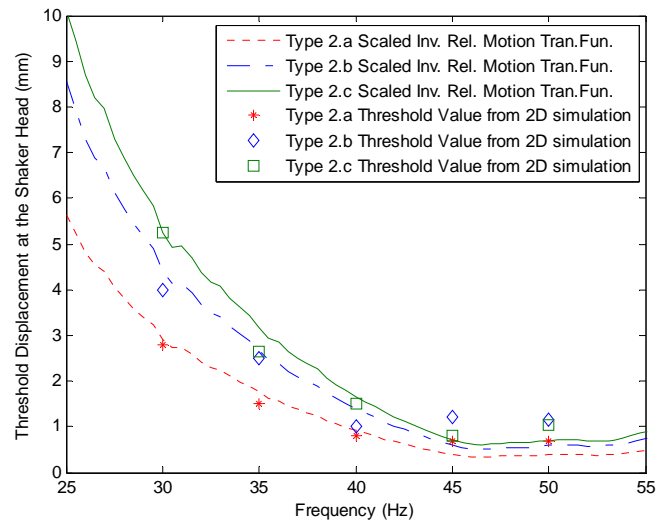


Figure 2-38: Comparison of fretting threshold displacements for Type 2 samples with different contact normal forces

2.6 Summary and Conclusions

A study of the vibration induced fretting degradation of a single blade-receptacle pair was presented. A series of blade/receptacle connector pair configurations were analyzed both experimentally and with an FEA model. Two variations of finish type were considered, with each finish type having three different contact normal force levels. Three supplementary steel balls served as an artificial loading condition were attached to the wires of each receptacle sample to make the system susceptible to fretting. The transfer functions and the fretting threshold displacement for a series of frequencies were measured in the experiment. The relative motion transfer function was proved to be a good indicator of the tendency of such systems to fret. The geometric dimensions, material properties and boundary conditions of the FEA model were generated based on the experimental values. The same x-axis relative motion at the contact interfaces was observed when the experimental threshold displacements were used as the input vibration

levels for this single blade/receptacle pair system. Finally, the results from the simulation were compared with the results from the experiment and generally found to be in good agreement. It was demonstrated that, for this limited system, finite element modeling and analysis methodology is a potentially valuable tool for the evaluation of the influence of design variations on the fretting behavior of connector. This study's findings can be summarized and concluded as follows:

- Transfer functions and threshold fretting displacements at the shaker head at different frequencies for the single blade/receptacle pair were observed in both experiments and simulation.
- The relationship between the relative motion function and the threshold fretting displacement at the shaker head for this contact pair system was proven.
- The x-axis relative motion at the contact interface was indicated to be the main source of fretting.
- The results from the simulation generally correlated well with those obtained from the experiment.
- Finite element modeling and analysis method has great potential for evaluating the influence of design variations on fretting behaviors.

CHAPTER 3 THREE DIMENSIONAL MODELING AND ANALYSIS OF A BLADE/RECEPTACLE CONNECTOR PAIR FOR THE PREDICTION OF VIBRATION-INDUCED FRETTING DEGRADATION

3.1 Introduction

Vibration-induced fretting can be a major problem for connector systems used in vehicle electronics. At present, most of the evaluations of fretting propensity for particular connector designs and the influence of variations in those designs on fretting performance are conducted through exhaustive experimental testing. A simulation-based method would be of great value to those responsible for connector design and application. As mentioned in Chapter 2, an earlier initial study was conducted in which a simplified finite element model was developed and experimentally validated for a blade/receptacle pair. However, due to the restrict assumptions and the geometric limitation of two-dimensional planar finite element analysis, the 2-D simplified model might not be accurate enough to completely represent the influences of the design factors, for example, the dynamic response of different contact normal forces. Moreover, considering of the fast development of computational capacity of computers, it is practical to perform simulations of a more complicated model in an acceptable time period on a better platform.

Based on the reasons above, in this study, a highly detailed 3-D finite element simulation model was developed in ABAQUS [14] according to true dimensions and

boundary conditions of the blade-receptacle connector pair configuration in experiments. A workstation with better computational capability (2 Quad Core Xeon Proc 5320, 16GB ddr2 memory, 640GB hard drive) as well as the parallel execution technology in ABQUS was utilized to reduce the computational time. The 3-D detailed model was then optimized and analyzed to evaluate the threshold vibration levels as a function of excitation frequency, wire tie-off length, supplementary mass, interface friction coefficient, and normal force. Finally, the results from the simulation were introduced and compared with the results from the 2-D simplified model simulation and the experiment. The content in this chapter describes all the details of this work.

3.2 Three Dimensional Detailed Finite Element Model Generation

An ABAQUS [14] detailed finite element model in three dimension (3-D) was developed from the CAD drawings for the sample experimental configuration as described in Chapter 2. This is a complicated but accurate model with all the real boundary conditions and material properties. This model is expected to have enough potential to precisely simulate most of the influences of different design factors of this blade/receptacle connector configuration.

3.2.1 Geometric Model

Figure 3-1 and Figure 3-2 show the overall view and cross-section view of the 3-D connector model to represent both the outside and inside structure. The connector model basically consists of four parts: wire, which is the electrical lead for electrical power transfer; supplementary mass, which serves to provide enough fretting damage for

the system; receptacle, including an out frame and an inside spring; blade, mated with the receptacle part with contacts with the spring and bottom inner layer.

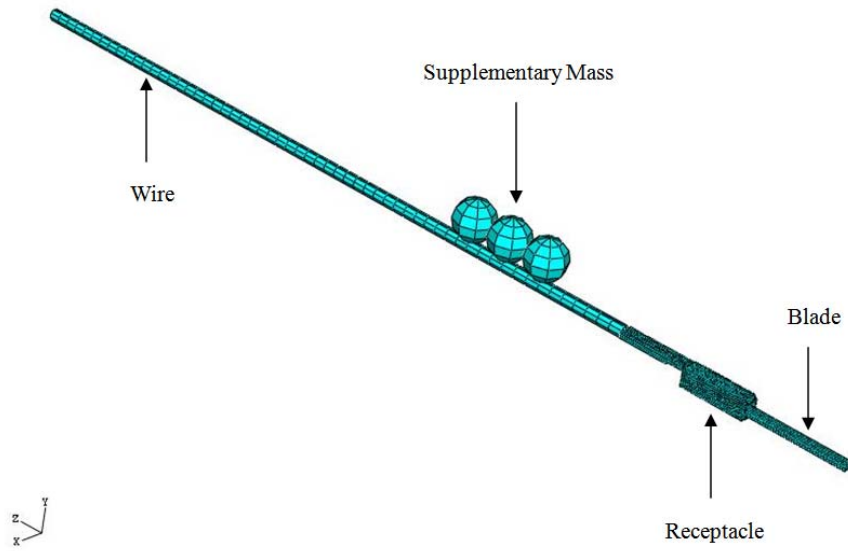


Figure 3-1: Overall view of the 3-D geometric model

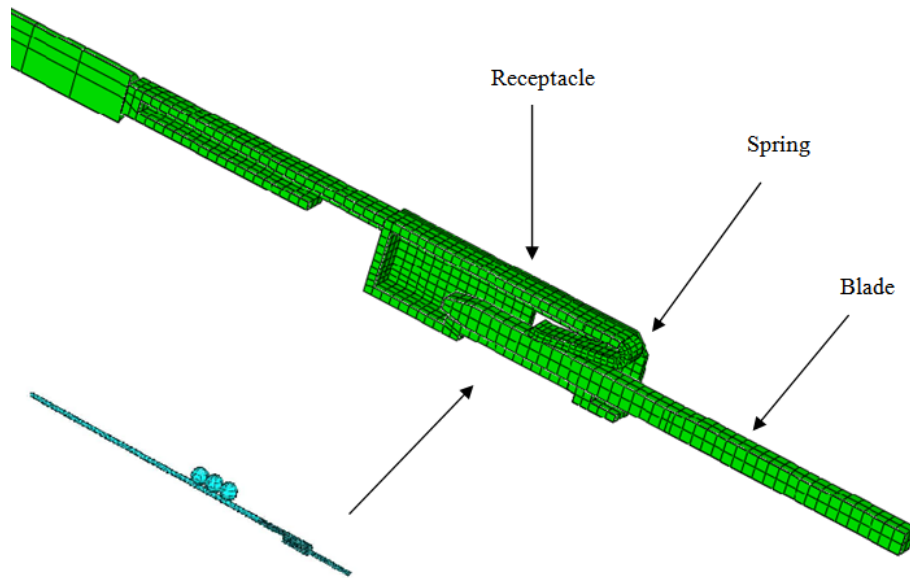


Figure 3-2: Close-up view (cross section) of the 3-D geometric model

The material properties of each model component are listed in Table 3-1. There are two sets of material properties for the two different plating finishes. Basically, the plating is expected to dictate the coefficient of friction. However almost all the other mechanical responses of the system are related to the copper alloy base materials used, which resulted in somewhat different for the two sample types. The material properties for the wire leads and auxiliary mass remain the same in simulations for all types of specimens.

Table 3-1: Material properties for 3-D model components

Components	Friction Coefficient	Density	Young's Modulus
Plating Type 1 (blade/receptacle section)	0.55	8910 kg/m ³	129.7 GPa
Plating Type 2 (blade/receptacle section)	0.33	8910 kg/m ³	120.6 GPa
Wire portion	-	3423 kg/m ³	96.5 GPa
Supplementary mass(balls)	-	7793kg/m ³	195 GPa

3.2.2 Mesh Control

3D standard stress elements were utilized for all components in this 3-D detailed model. According to the calculation strategy of finite element method, the hex elements with cuboids structure would result in more accurate results. Therefore, all parts in the 3-D model were meshed by structure technique into hex elements except the three supplementary balls. Proper partitions were assigned to the model to ensure the execution of the structure mesh especially for the receptacle part which includes complicated geometry. Figure 3-3 shows the details of partitions in the receptacle (without spring). The supplementary balls and wire were meshed separately by sweep technique. This is

because the circular structure can only be meshed with sweep or free mesh, and sweep technique is considered to be more precise in this situation.

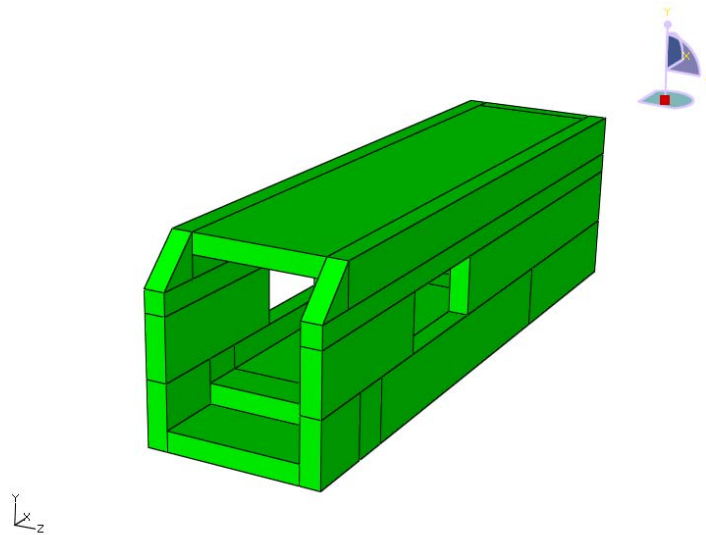


Figure 3-3: Partitions in the receptacle component

In consideration of the complexity as well as the resulting computational cost, different mesh size controls were assigned to different parts based on its importance. As shown in Figure 3-2, the blade was finely meshed to elements of approximately $0.4\text{mm} \times 0.375\text{mm} \times 0.4\text{mm}$ (length*width*height). It is basically a nonlinear contact process between spring and the upper surface of the spring, which would significantly affects the convergence. Therefore, mesh convergence and adjusted step increment was utilized in this model. Moreover, as one could easily expected, after mated together, the spring part inside the receptacle had very large deformation and high bending stress. Therefore, the mesh size on the spring was adjusted to be very small, at a size of $0.15\text{mm} \times 0.15\text{mm} \times 0.15\text{mm}$. After optimized mesh, the 3-D details model contains 3442 elements and 6150 nodes. Table 3-2 lists the element types, mesh techniques and sizes for all parts in the model.

Table 3-2: Mesh techniques and size control for different components

Components	Mesh Technique	Mesh Size (mm)
Blade	Structure	0.4*0.375*0.4
Receptacle Frame	Structure	0.35*0.35*0.35
Spring	Structure	0.15*0.15*0.15
Supplementary Mass	Sweep	1.5 (Global Size)
Wire	Sweep	2.0 (Global Size)

3.2.3 Parallel Execution

The accurate 3-D model contains a large number of elements which could result in long computational time (four to six hours in many cases) for a single simulation run on a single-processor workstation. Dell Precision 690 workstation was utilized for the 3D simulation, as shown in Figure 3-4. This is an ultra-high-performance workstation that is designed to maximize performance and scalability in an innovative, customer-driven workstation with great computational capability. Table 3-3 lists the specifications of the system. Moreover, the Linux Operating System was installed in this computer to enhance the computational speed of ABAQUS especially for complicated models. Parallel execution technology in ABAQUS was utilized to increase the computational speed. This technology allows the computer to run the complex model in multiple processors (8 processors on this workstation) at the same time and dramatically reduce the computational cost.



Figure 3-4: Picture of the workstation for the 3-D simulation

Table 3-3: Specifications of the workstation

Type	Dell Precision 690n Mini-Tower
Processor	Quad Core Xeon Proc E5320 1.86GHz, 2 X 4MB L2 Cache
Memory	16GB, DDR2 ECC SDRAM Memory 667MHz, 4X4GB
Video Card	nVidia, Quadro FX 3500, 256MB PCIe x16, dual VGA or DVI Graphics Card
Hard Drive	4* 160GB Serial ATA, 10K RPM Hard drive with 16MB Data Burst Cache
Operating System	Red Hat Enterprise Linux WS v4Intel EM64T 64bit

3.2.4 Define Contact

Contact is a crucial problem in the 3-D modeling and simulation. In section 2.4, the vibration process simulation in 2-D simplified model indicated that the main motion of the receptacle is a “rock motion”. Therefore a complicated process in combination of impact, slippage and sliding would be expected to exist in the contact. Figure 3-5 shows the defined node-to-surface contact pair in the model. The pink surfaces are the slave surfaces including bottom surface of the spring and upper side of bottom inner layer of the receptacle with smaller mesh size. The red surfaces are the master surfaces including bottom and upper surfaces of the blade with larger mesh size. One reason of the different mesh sizes is during the calculation of contact in ABAQUS, the slave surface is not allowed to penetrate into the master but the penetration of master nodes to slave surface is acceptable. Thus, if the mesh size of the master surface is smaller than slave surface, more nodes will penetrate into the slave surface and more intersection will exist in the contact pair which might lead to inaccurate results and difficulties in convergence.

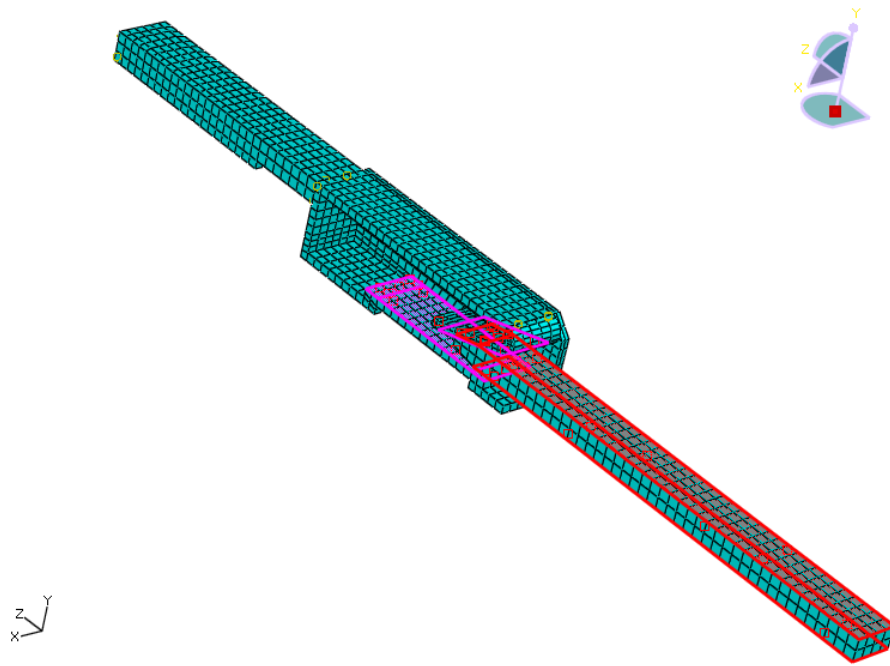


Figure 3-5: Defined contact pair in 3-D model

3.3 Simulation Methodology and Boundary Conditions

In order to evaluate the fretting behavior of the connector systems, two different simulation: the harmonic analysis in frequency domain to determine the transfer functions and the vibration process simulation in real time domain to observe the relative motion at the contact terminals were conducted

3.3.1 Mating Process Simulation

One challenging aspect in this simulation is to ensure the stiffness value of the spring as well as the generated contact normal force to be as close as possible to the real values. In the production process, the spring part was pushed up with different forces to generate different distances between the right bottom surface of the spring and upper side of the inner layer of the receptacle. These different distances of “gaps” were utilized to

reflect different spring stiffness and contact normal forces. One example for the “gap” is shown in the unmated connector pair in Figure 3-8. Therefore, in order to assure the same effect, a “mating” step was created in both harmonic and vibration simulation. In this step, the blade was located close to the spring at the beginning, then inserted in and finished entire mating process. The insert-in distance is determined as the same distance in the experiments. Figure 3-9 and Figure 3-10 show the pictures of details of the mating process in 3-D simulation.

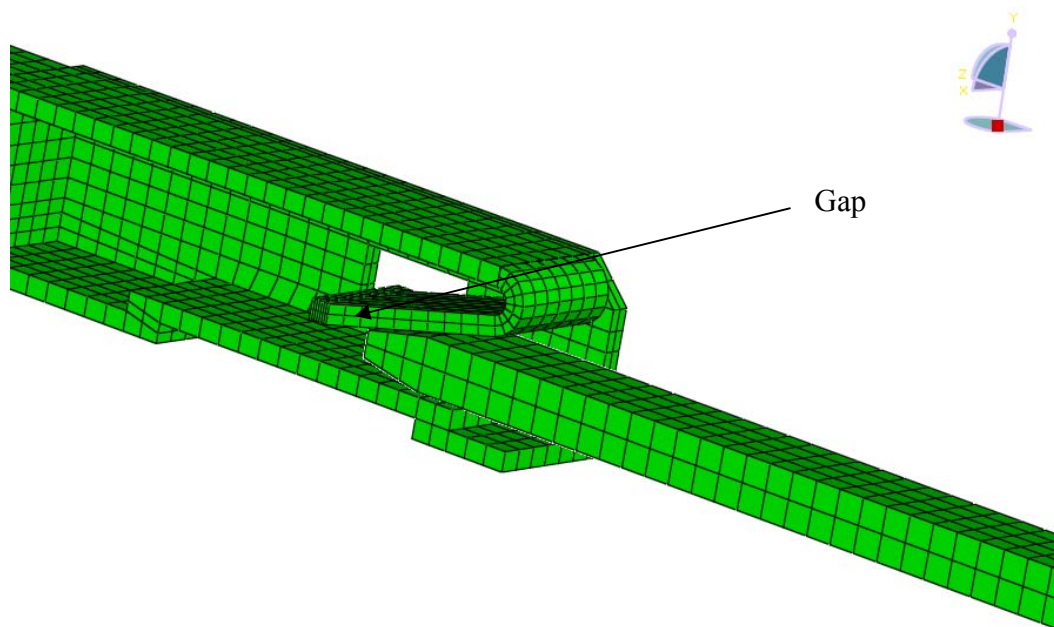


Figure 3-6: Unmated connector pair

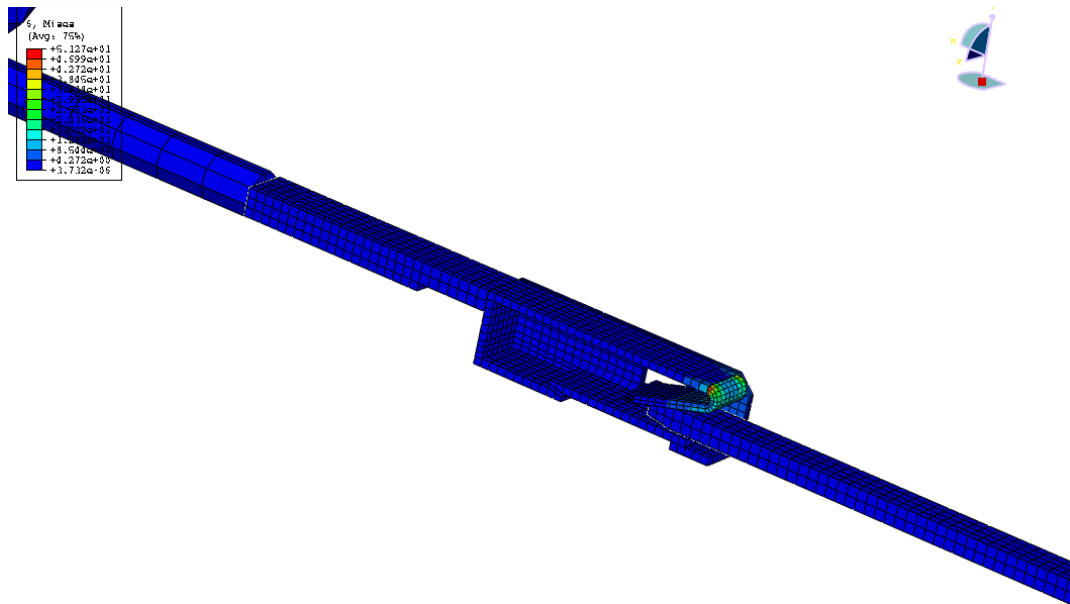


Figure 3-7: Connector pair in mating process

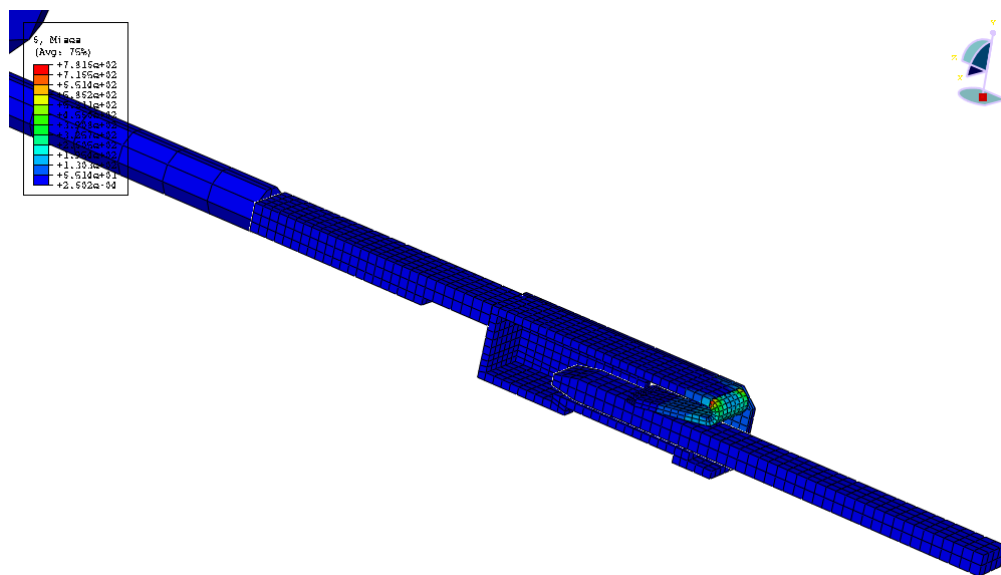


Figure 3-8: Mated connector pair

Epoxide solidification experiments were performed to study the mated process especially the inside structure geometry for mated and unmated connector pairs. The

connector samples were first epoxied in a rubber cup and solidified for about 24 hours. Then the side part of the connectors were polished away to expose the inside structure. The unmated receptacle part and the mated connector pair are shown in Figure 3-9 and 3-10, respectively. It could be observed that the 3-D mating process simulation generally represented the real situation. Thus the stiffness and contact normal force values in the 3-D detailed model should be very close to the real values in the experiments.

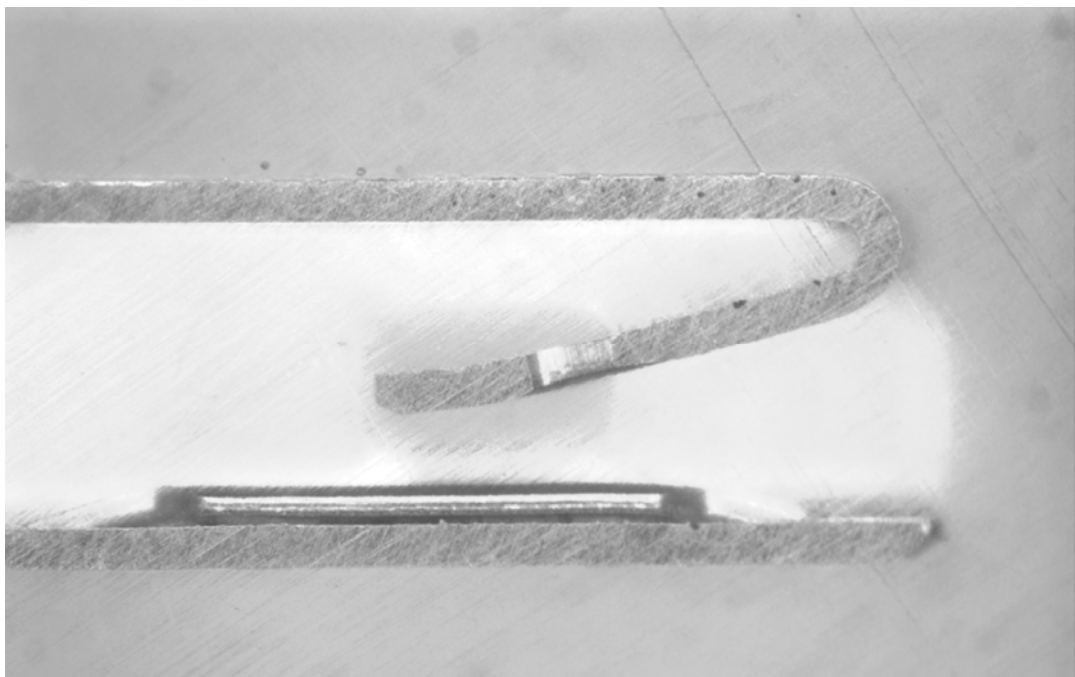


Figure 3-9: Unmated receptacle part

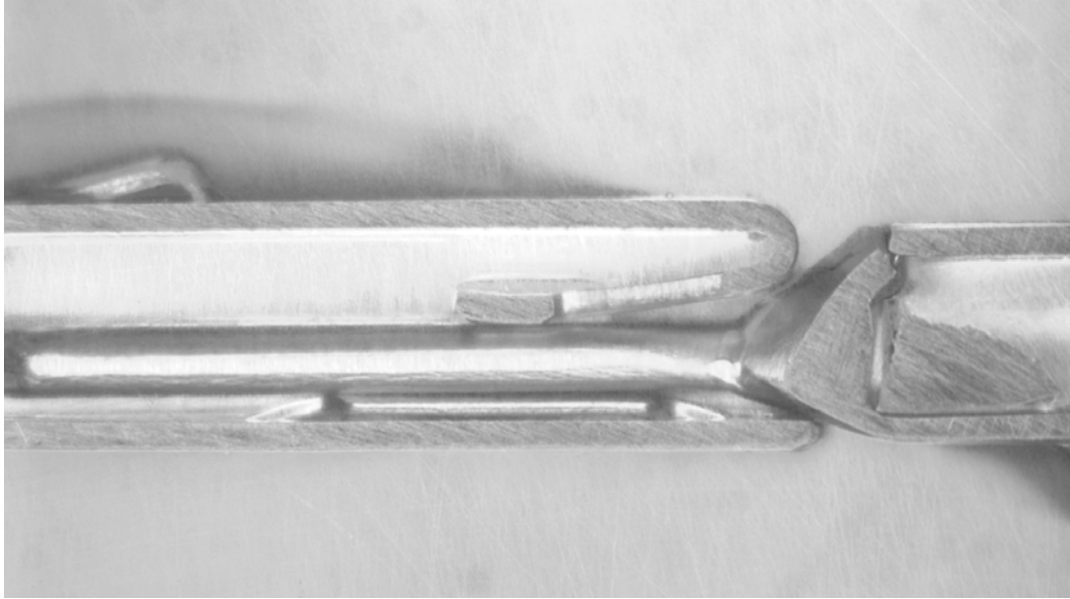


Figure 3-10: Mated connector pair

3.3.2 Boundary Conditions

Figure 3-11 shows the boundary conditions utilized in harmonic and fretting simulation of the 3-D detailed model. These conditions were determined the same as those in the experiment setup. The end of the electrical wire from the receptacle part was constrained in all degrees of freedoms while the left end of the blade was fixed in horizontal axis (z-axis in the model) to reflect that it was clamped firmly at the shaker head and only vertical motions (y-axis in the model) were allowed in the experiment. In order to simulate the vibration motions, the periodic motion function was used to define the amplitude. The function is defined as below:

$$a = A_0 + \sum_{n=1}^N [A_n \cos n\omega(t - t_0) + B_n \sin n\omega(t - t_0)] \quad (1)$$

where A_0 is the initial amplitude, A_n and B_n are the constants, w is the circular frequency defined as:

$$w=2\pi*f \quad (2)$$

where f is the frequency value from the experiments. The corresponding circular frequency values for frequencies tested in the experiment are shown in Table 3-4. According to the fretting threshold experiments, sinusoidal motion was generated from the shaker head for different frequency. Therefore in this particular circumstance, $A_0= 0$, $n=1$, $A_1=0$, $B_1=1$ $n=1$. The refined function is as below:

$$a = \text{Sin}w (t-t_0) \quad (3)$$

This function could correctly reflect the different vibration motions in fretting threshold experiments. For harmonic, simulation, a random noise from 20Hz to 70Hz was utilized in transfer function experiments.

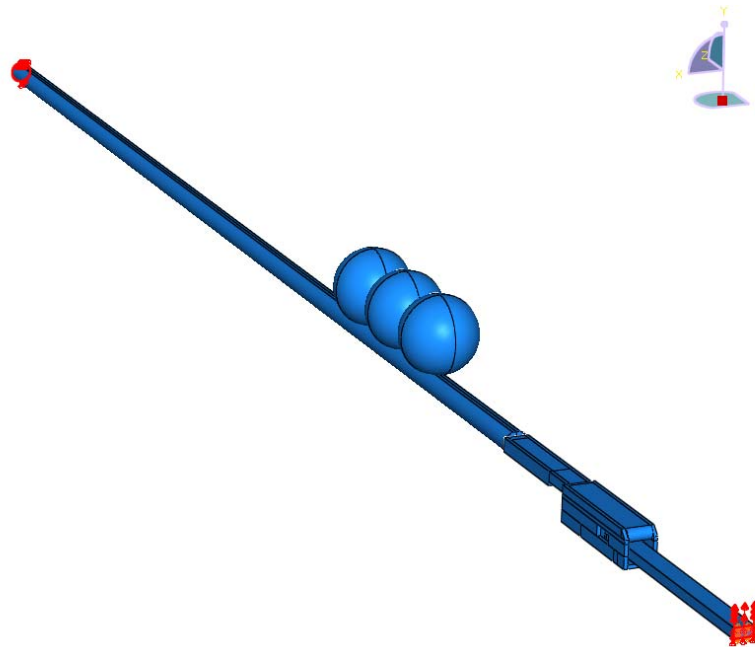


Figure 3-11: Boundary conditions in the 3-D model

Table 3-4: Corresponding circular frequency values in the 3-D simulation

Frequency tested in experiments	Corresponding circular frequency in the 3-D simulation
30Hz	188.4
35Hz	219.8
40Hz	251.2
45Hz	282.6
50Hz	314.0

3.4 3-D Detailed Model Simulation Results

Based upon the system configuration above, simulation studies of the 3-D detailed model were performed to evaluate the dynamic behavior of the system including the harmonic (transfer functions) and fretting thresholds simulations. The results were then compared and validated with 2-D simplified model simulation and experiments results. Details are described in sections below.

3.4.1 Transfer Functions

As described in Chapter 2, relative motion between the contacting terminals is proved to be the basic inducement and a significant indicator of the fretting degradations. In the previous study, transfer functions were observed in both the experiments and the 2-D simplified model simulation in ANSYS. For this 3-D detailed model simulation, the input location was on node Blade-296 and the output location was on node Female-2124 as shown in Figure 3-12. Both nodes were selected as the same positions as those in the experiments and the 2-D simulation.

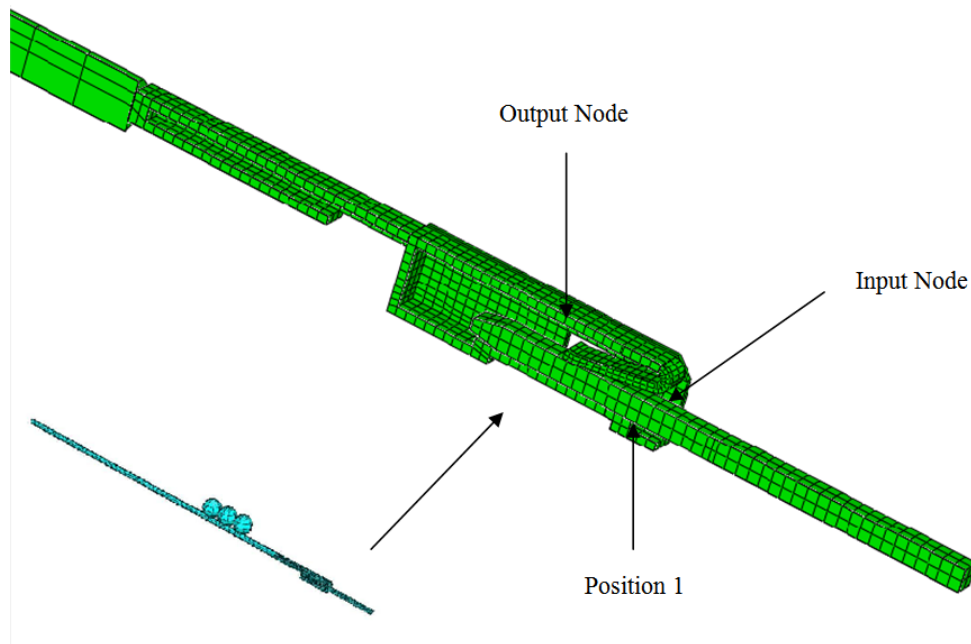


Figure 3-12: Nodes location in the 3-D detailed model

Figure 3-13, Figure 3-14 and Figure 3-15 show the transfer functions which were obtained from experimental testing, the 2-D simplified model simulation, and the 3-D detailed model simulation for different contact normal force levels respectively. It can be observed from Figure 3-13 that there were significant variations between the transfer functions for the various normal forces in the experiment, especially the first resonant peak. The frequency where the first resonant peak occurs for Type b is lower than Type a, while the frequency for Type c is larger than Type a. This behavior cannot be obtained from the 2-D simplified model in Figure 3-14. However, in the 3-D detailed model simulation, as shown in Figure 3-15, this trend was observed again. A possible reason of the better fit of the 3-D simulation results is that the 3-D detailed model could reflect all the same geometry and boundary conditions as in experiments, no stringent assumptions needed. Moreover, as described in Section 2.3, due to the limitation of the 2-D plane

model, the elasticity of the outer structure of the receptacle was adjusted to be much higher than real value in order to fix the two sides as that of the experimental configuration. This assumption would result in over constrains on the spring and the upper side of receptacle, which could minimize the different effects of different contact normal forces levels as well as the correlated transfer function results.

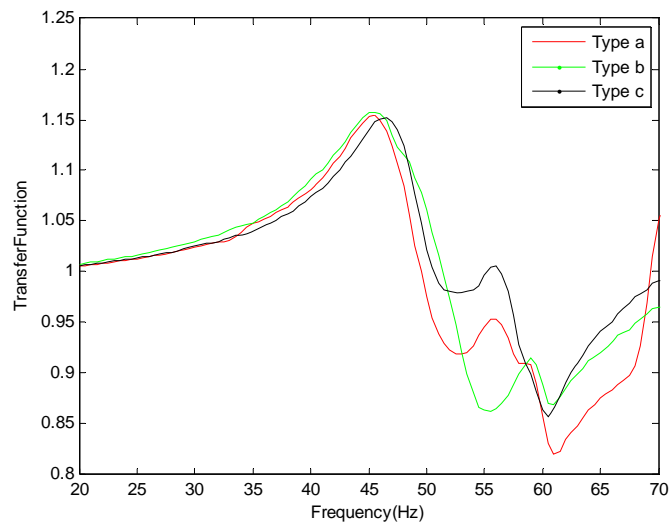


Figure 3-13: Experimental transfer function results for different contact normal force levels

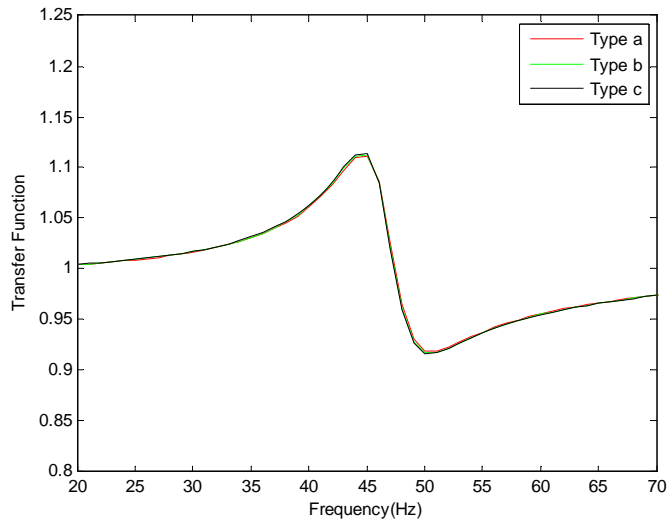


Figure 3-14: 2-D simulation transfer function results for different contact normal force levels

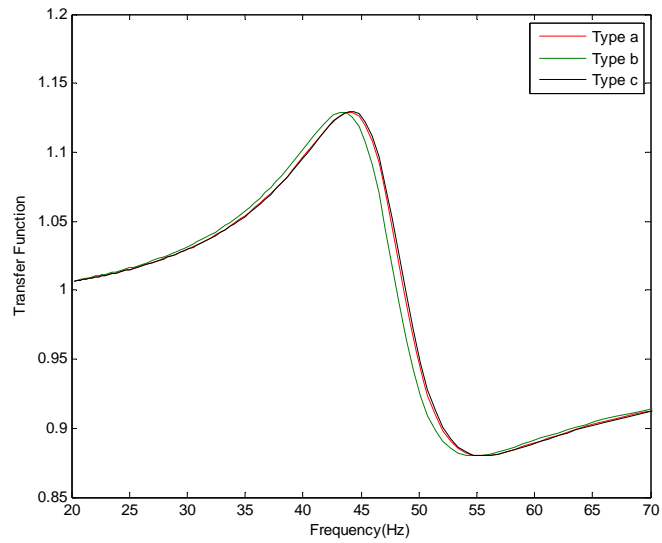


Figure 3-15: 3-D simulation transfer function results for different contact normal force levels

Figure 3-16 and 3-17 show the comparison of experimental data to the 2-D model simulation results and the 3-D model simulation results for different friction coefficient (Type1 and Type 2). It could be observed from Figure 3-16 that the transfer function

results generated from 2-D model simulation matched the experimentally measured values well particularly for the lower frequency. However, this result did not fit the experimental results in the entire frequency range. Moreover, in consideration of the first resonant peak, the magnitude of the transfer function from the 2-D model simulation is approximately 5% lower. In comparison, the 3-D model simulation result generally matched the experimental result well and the magnitude of the first resonant peak is only about 1.7% lower. The overall shape of the 3-D model simulation result also matched the experimental result much better than 2-D model simulation. Especially from 45Hz to 55Hz, the experimental result trace and the 3-D simulation result trace almost superposed each other while there's a significant difference for the 2-D model simulation result. Thus, the detailed 3-D model simulation shows a much better potential in the prediction of transfer functions than the 2-D simplified model.

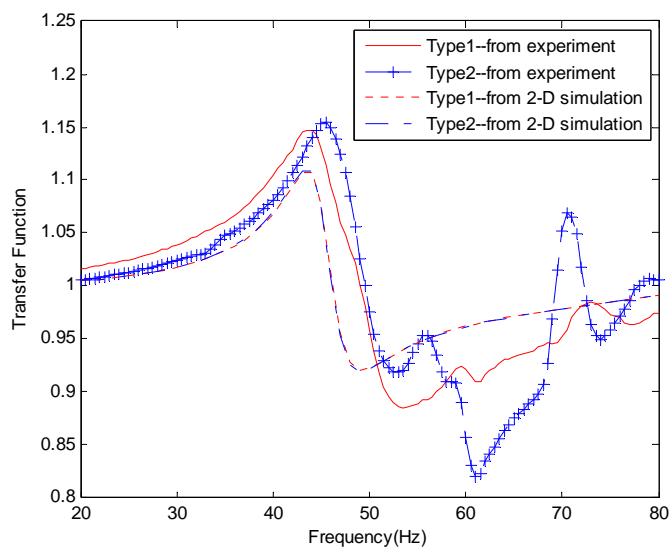


Figure 3-16: Comparison of experimentally determined transfer function and 2-D simulation model results

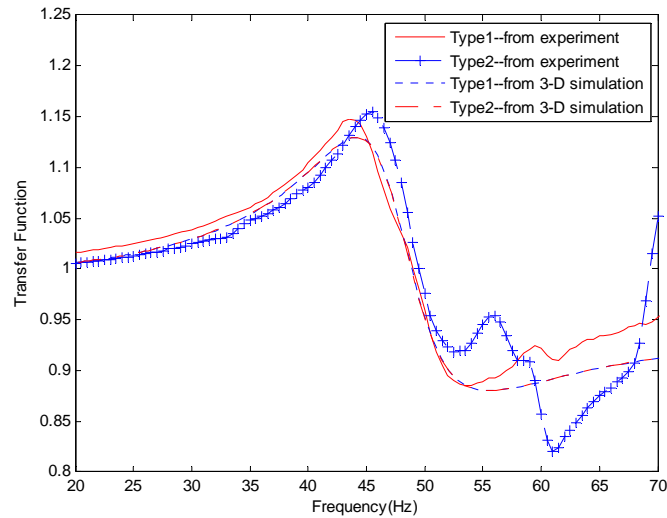


Figure 3-17: Comparison of experimentally determined transfer function and 3D simulation model results

The comparison of the predicted influences of different the wire tie-off lengths on relative motion transfer functions between 2-D simplified model simulation and 3-D detailed model simulation are shown in Figure 3-18. It is observed from both simulations that as the tie-off length is decreased, the resonant peak shifts to the right and tends to become somewhat higher in amplitude. This effect is due to a relative increase of the system stiffness which would result in an increment in the nature frequency. The shorter wire tire-off length also leads to a decrease in system internal damping, which comes primarily from the wiring and result in the increment of amplitude. Figure 3-19 shows the comparison of predicted effects of different auxiliary mass on the relative motion transfer functions between the 2D simplified model simulation and the 3D detailed model simulation. Similarly, both 2D and 3D simulations shows that as the auxiliary mass is increased, the resonant frequency decreases and the amplitude of the resonant peak increases dramatically. This trend provides an explanation for the difficulty in obtaining fretting for samples without auxiliary mass. That is, the relative motion in the frequency

and amplitude range of interest is too small to produce significant fretting degradation. Substantial additional vibration energy would have to be put into that sample configuration in order to exceed the threshold levels required for the onset of fretting.

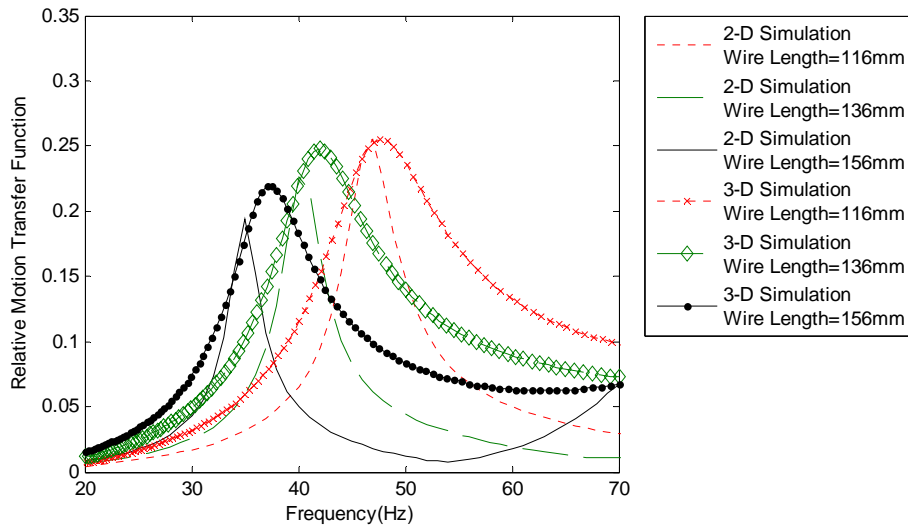


Figure 3-18: Comparison between 2-D simulation and 3-D simulation of relative motion transfer functions for various tie-off lengths (Specimen Type 2.b)

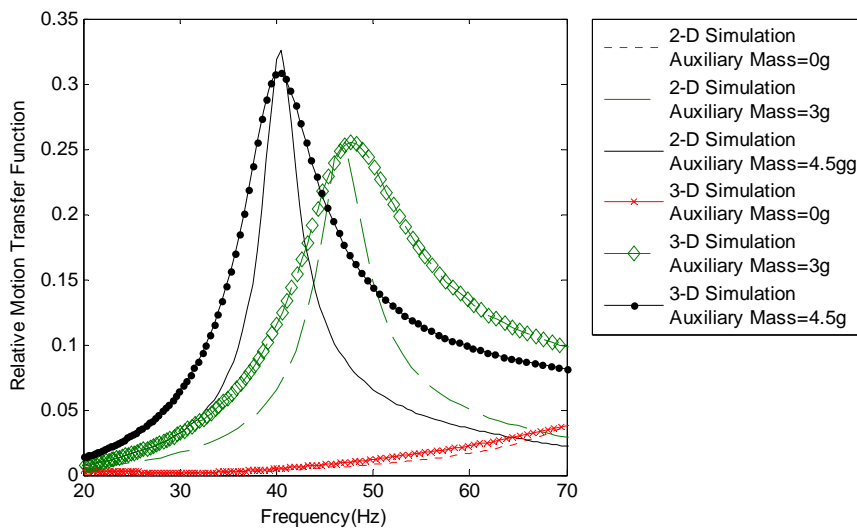


Figure 3-19: Comparison between 2-D simulation and 3-D simulation of relative motion transfer functions for various tie-off lengths (Specimen Type 2.b)

3.4.2 Threshold Values

As described in Chapter 2, the inverse relative motion transfer function is demonstrated to be a good predictor of the variation in the threshold values with excitation frequency. It was also observed that the x-axis relative motion at the position 1 where the blade and the left inner bottom surface contact during the rock motion, as shown in Figure 3-12, is the indicator of the threshold values in the modeling simulation. Figure 3-20 and Figure 3-21 show the threshold values from the 3-D detailed model simulation results and experimental inverse relative motion transfer functions. The 3-D simulation results generally match the experimental inverse relative motion transfer function quite well. The same trend, that is the fretting threshold value generally increased as the increment of the contact normal force levels (from Type a to Type c), was also predicted.

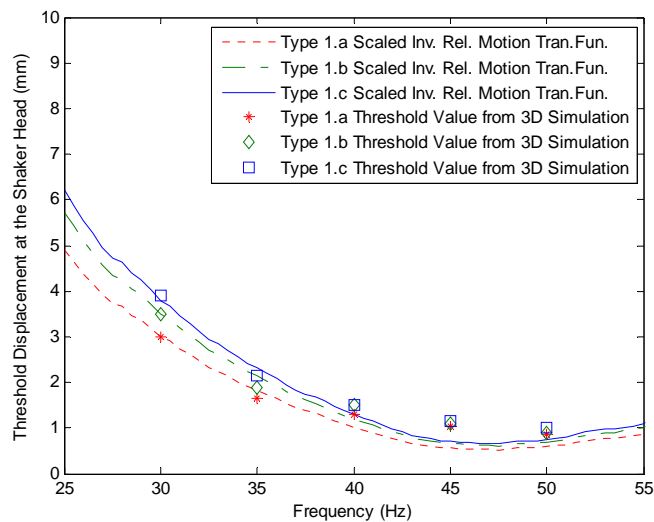


Figure 3-20: Comparison between 3D simulation results and experimental results for scaled inverse relative motion transfer functions for Type 1 samples

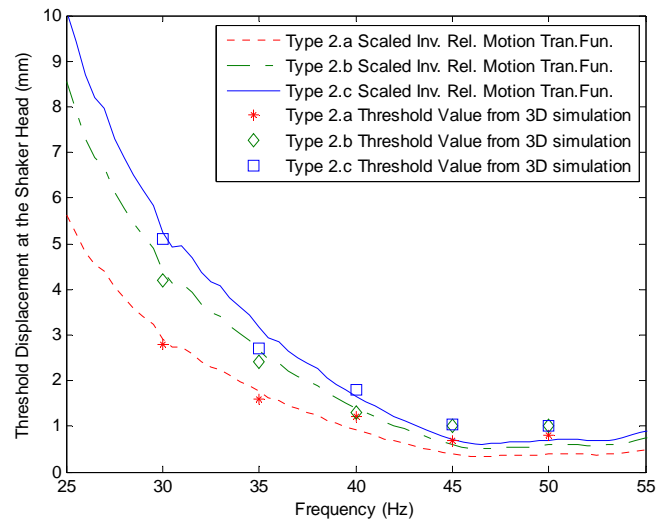


Figure 3-21: Comparison between 3D simulation results and experimental results for scaled inverse relative motion transfer functions for Type 2 samples

Figure 3-22 to Figure 3-27 show the comparison of the threshold value from experiments, the 2-D simulation and the 3-D simulation. It could be observed that the 3-D detailed model simulation matches the experimental results slightly better than the 2-D model especially in the higher frequency range (for example at 50Hz). The better fit in the 3-D results especially at higher frequency is in good match with the transfer function results observed in the 2-D simplified model simulation as mentioned in previous sections.

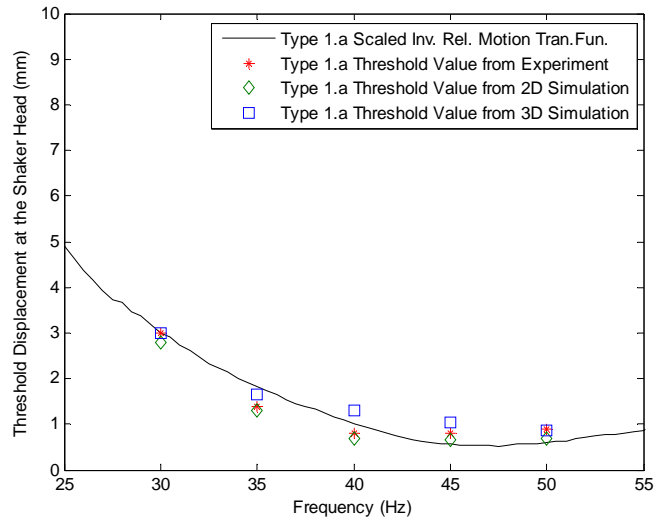


Figure 3-22: Comparison of 2-D simulation, 3-D simulation and experimental results with scaled inverse relative motion transfer functions (Specimen Type 1.a)

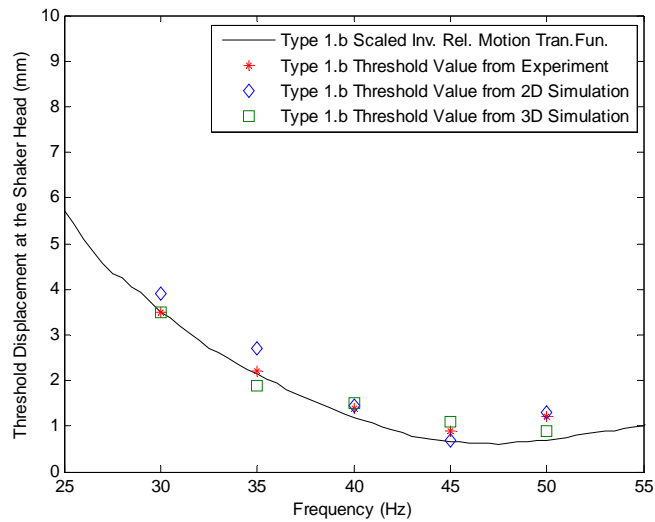


Figure 3-23: Comparison of 2-D simulation, 3-D simulation and experimental results with scaled inverse relative motion transfer functions (Specimen Type 1.b)

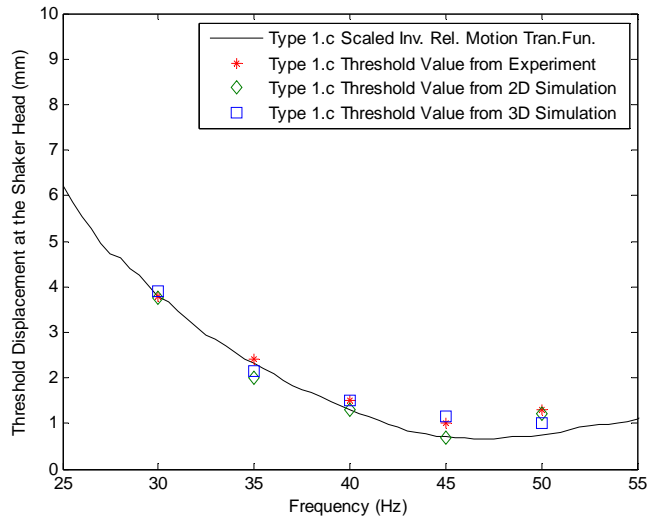


Figure 3-24: Comparison of 2-D simulation, 3-D simulation and experimental results with scaled inverse relative motion transfer functions (Specimen Type 1.c)

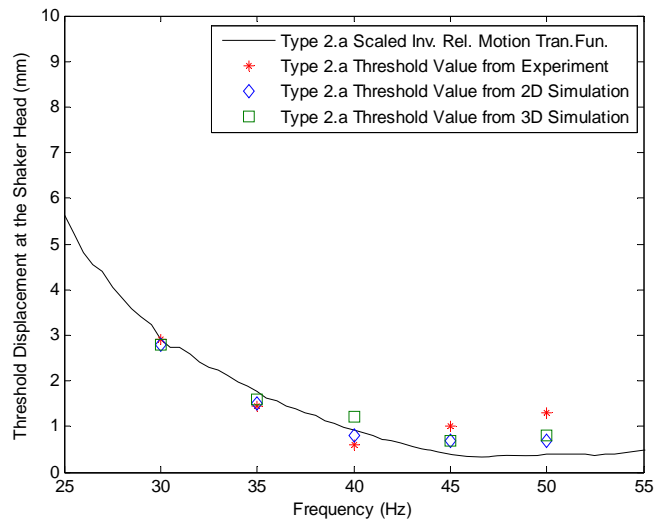


Figure 3-25: Comparison of 2-D simulation, 3-D simulation and experimental results with scaled inverse relative motion transfer functions (Specimen Type 2.a)

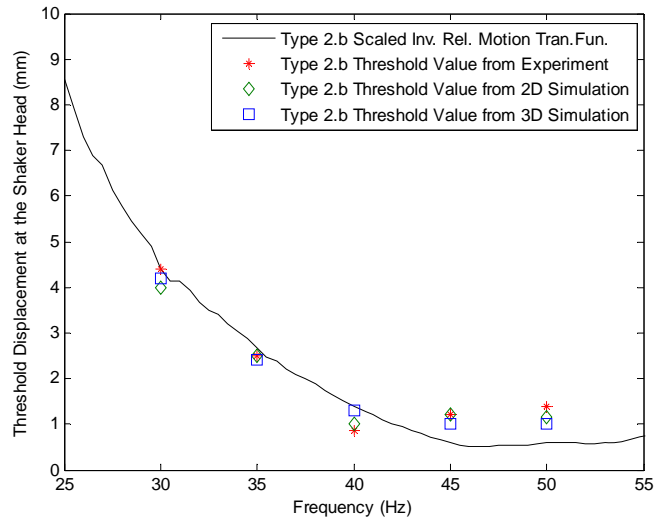


Figure 3-26: Comparison of 2-D simulation, 3-D simulation and experimental results with scaled inverse relative motion transfer functions (Specimen Type 2.b)

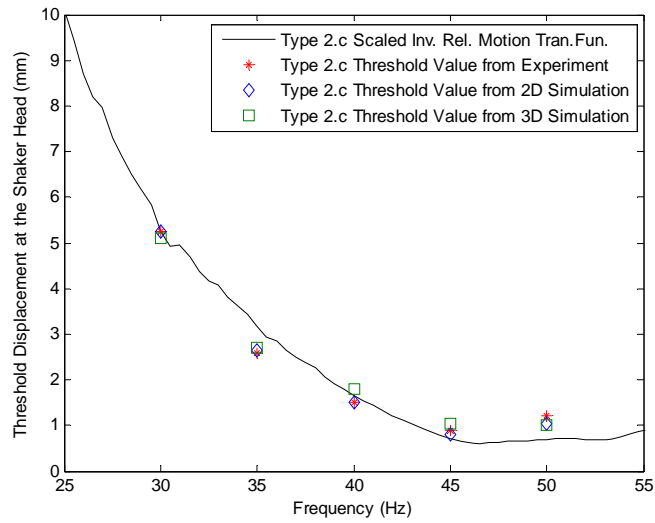


Figure 3-27: Comparison of 2-D simulation, 3-D simulation and experimental results with scaled inverse relative motion transfer functions (Specimen Type 2.c)

A comparison of fretting threshold results for different wire tire-off lengths was performed on both 2-D and 3-D model simulations. As shown in Figure 3-28, both 2-D

and 3-D simulation results showed the same trend. As the tie-off length is decreased, the lowest threshold displacement at the shaker head shifts to the right. This result generally matches the first resonant peak shifting in the transfer function simulation.

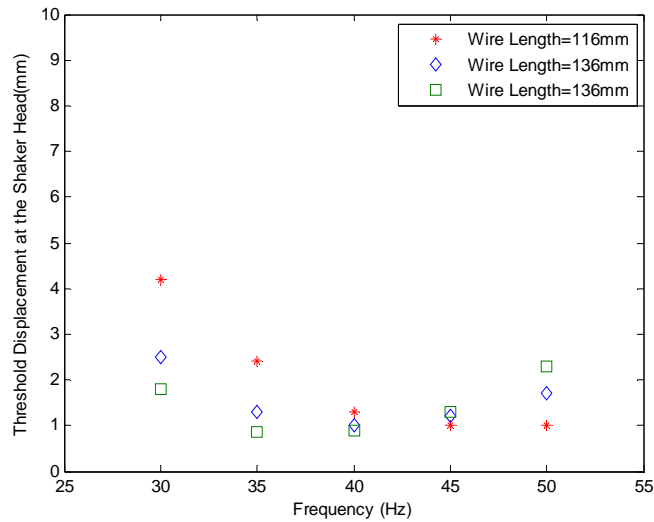


Figure 3-28: 3D detailed model simulation of threshold values for various tie-off lengths (Specimen Type 2.b)

3.5 Computational Cost

Computational cost is always a crucial issue in simulation. In three-dimensional simulation in ABAQUS/Standard, considering the cubic mesh, if the size of each element is reduced to half, the total computational cost will increase $2*2*2$ times for three dimensions. Moreover, due to the size change of the smallest elements in this model; the cost will increase another 2 times. Therefore, the total computational cost will increase to 2^4 or 16 times. This explains the complicity of the 3-D detailed model and the importance of the optimization to balance the mesh size and the accuracy of the results.

Figure 3-30 shows the comparison of computational time of single threshold simulation between 2-D and 3-D models. It could be observed that the time of 3-D

detailed model is about 45 minutes while that of the 2-D simplified model simplified model is about 4 minutes. Although the 3-D model takes about 11 times longer than 2-D model, a 45 minutes run is still acceptable for repeated simulation studies. Therefore, for this particular configuration, the 3-D model is practical and more accurate while the 2-D simplified model simulation is more time-efficient and less accurate. However, if for a more complicated system, the 2-D model might be more practical.

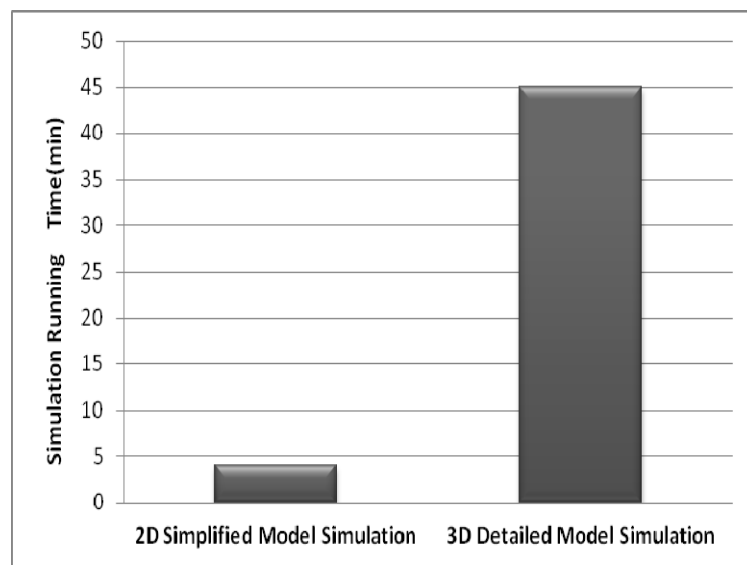


Figure 3-30: Comparison of single threshold simulation running time between 2D simplified model and 3D detailed model

3.5 Summary and Conclusions

In this study, a highly detailed 3-D finite element model in ABAQUS for a single tin-plated blade/receptacle connector pair was developed and analyzed to evaluate the threshold vibration levels. Specimens with different normal forces and finish Type have been considered. The geometric dimensions, material properties and boundary conditions of the FEA model were generally the same as the real experimental values. Simulations of the 3D detailed model have been performed to determine the transfer functions and

threshold fretting levels for various excitation frequencies, wire tie-off lengths, supplementary mass, interface friction coefficients, and normal force values.

Finally, the 3-D detailed model simulation results were compared with the 2-D simplified model simulation results and with the physical experiments. The 3-D detailed model simulation results were found to be in good agreement with the experiment and proved to be more adaptable than the 2-D simulation which requires constraining assumptions and corresponding model components. It was proven that, the present finite element modeling and analysis methodology has demonstrated potential for evaluating the influence of design variations on fretting behavior of the single blade/receptacle connector pair. This study's findings can be summarized and concluded as follows:

- A 3-D detailed finite element model was developed and optimized in ABAQUS.
- Harmonic simulation and fretting threshold simulation studies were performed on this 3-D model for all different types of connector samples.
- Consistent relationships between the relative motion function and threshold displacement at the shaker head were once again proven.
- Results from the 3-D simulation results generally matched those from the corresponding experiments quite well.
- The 3-D simulation is more adaptable to the analysis of practical connector designs than 2-D simulation, which requires constraining assumptions and corresponding model components.
- The present finite element modeling and analysis have demonstrated potential for evaluating the influence of design variations on fretting behavior.

CHAPTER 4 THE APPLICATION OF FEA SIMULATION TECHNIQUES TO THE FRETTING DEGRADATION OF A CONNECTOR SYSTEM

4.1 Introduction

Fretting degradation can be a major problem in vehicle connectors. At present, much of the evaluation of fretting propensity for particular connector designs and the influence of variations in those designs on fretting performance is conducted through exhaustive experimental testing, which requires a major commitment of time and resources. Therefore, a simulation-based method would be of great value to those working on connector design and applications.

In the author's previous work, a simplified two dimensional finite element model and a highly detailed three dimensional finite element model were developed and experimentally validated for a single blade/receptacle pair connector system, as described in previous chapters. The 3-D detailed model simulation results were then compared with the 2-D simplified model simulation results and with the physical experiments in many aspects. The 3-D simulation results show a slight advantage than 2-D simulation in predicting overall shape of the transfer function but requires more computational cost. Both the 2-D simplified model and 3-D detailed model simulations were generally found to be in good agreement with the experiments. This finding demonstrated the great potential of the finite element analysis techniques in predicting the vibration-induced fretting corrosion in single blade/receptacle connector pair configuration.

However, in the industry application of the connector system in vehicles, not single but sixteen pin connector pairs are sealed together in a housing part and serve as one entire system. Therefore, it would be of great value to apply the FEA techniques to develop and analyze a connector system model in order to provide a reliable tool to the designers to evaluate the fretting characteristics of different connector designs. Based on this purpose, a two dimensional simplified model and a three dimensional detailed model were developed and compared for the connector system in this study. A series of simulations were performed on the selected 2-D model. Corresponding experiments were conducted to validate and test the performance of the system.

4.2 Experimental Configuration

4.2.1 Experimental Samples

A series of samples were fabricated based upon a commercially available automotive connector design, as shown in Figure 4-1. Both receptacle and blade part have two rows of connectors with each row consists of 8 single tin-plated blade/receptacle connector pairs. After mating, all the connector pairs are sealed in the plastic housing and leads with two 230 mm long wires at both ends. Similar to the single connector pair samples, the connector system samples also have two different plating finish / base metal configurations and three contact normal force levels. Table 4-1 summarizes the sample types. Both finishes were based upon a pure tin system, although the type 2 finish structure had been modified to produce a coefficient of friction approximately half of the coefficient for the type 1 finish. The thicknesses of the metal strips used to fabricate the terminals were the same, and the elastic modulus of the samples were very similar.

cannot reach the measurement location on the connector pairs. According to Flowers and Xie's previous study on this topic [38][52], viewing slots were machined on the housing system, as shown in Figure 4-2. These slots allow the laser beams to go through the plastic housing and direct access to the mating terminal pairs in each half of the connector. The slots were positioned carefully at the locations which not only could reflect the right motions for the transfer function testing but also not to alter any features of the housing that constrained terminal motions.



Figure 4-2: Photograph of the connector system sample

4.2.2 Experimental Equipment

During this study, most experimental equipments used were the same as those in the previous studies. Details of the equipments including the Keithley Model 2010 multimeter, the HP 35665A Dynamic Signal Analyzer, and the POLYTEC laser vibrometer were all described in Chapter 2. However, in order to meet the requirement of

the larger g-level in the experiments, a more capable vibration system which consists of a bigger shaker and an enhanced amplifier was utilized.

The vibration system consists of the equipment below: LDS V850 shaker [55], LDS SPAK amplifier, KISTLER 8720 accelerometer, DACTRON LASER vibration control system with DAQ card and a cooling system [56]. Figure 4-3 and Figure 4-4 show photographs of these facilities. In general, this is a close-loop system and the details of its constructions are shown in Figure 4-5. During its working process, the controller first sends the output signals which have been pre-defined in the profile to the amplifier and then to the shaker. When the shaker starts vibrating, the feedback signal is generated from the accelerometer attached to the sliding table and then received by the control system through the DAQ card. The control system would compare the feedback signal with the pre-defined profile to identify if it runs properly and make proper adjustments to the output. This close-loop would keep running to ensure the shaker is vibrating properly according to the pre-defined profile. Specifications of the all these equipments are listed as below.

LDS 350 vibratory shaker:

- Useful frequency range: DC~3000Hz
- Velocity, sine, peak: 2.0 m/s (78.7 in/s)
- Acceleration, sine, peak: 5888.4 m/s² (60.0 g_n)
- Displacement peak-peak: 50.8 mm (2.0 in)

LDS SPAK Amplifier:

- Power range: 5-50 kVA in 5 kVA increments

- Rated output voltage: 100 V rms

An amplifier's self-protection capability is very important for safety reasons during vibration tests. The amplifier system is protected by the following interlocks:

- Output over-voltage
- Amplifier over-temperature
- Vibrator over-travel
- Slip Table over-travel
- Vibrator cooling system failure
- Input overdrive
- Power module failure

KISTLER 8702B50 accelerometer,:

- Measuring Range: -50 g~50 g
- Sensitivity: 99.5 mV/g
- Transverse Sensitivity: 0.3 %
- Resonant Frequency: 54.0 kHz
- Temperature: -54 – 100 °C

DACTRON LASER Vibration control system:

- Frequency range: Up to 42 kHz analysis frequency.
- Frequency accuracy: Within 0.01%
- Dynamic range: 120 dBfs.



Figure 4-3: Photograph of LDS V850 shaker with KISTLER accelerometer

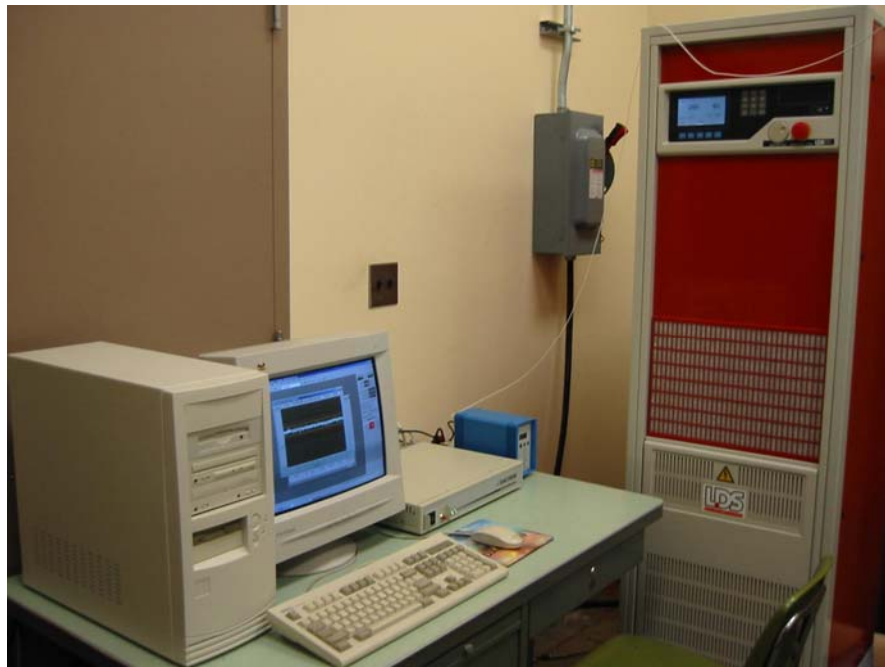
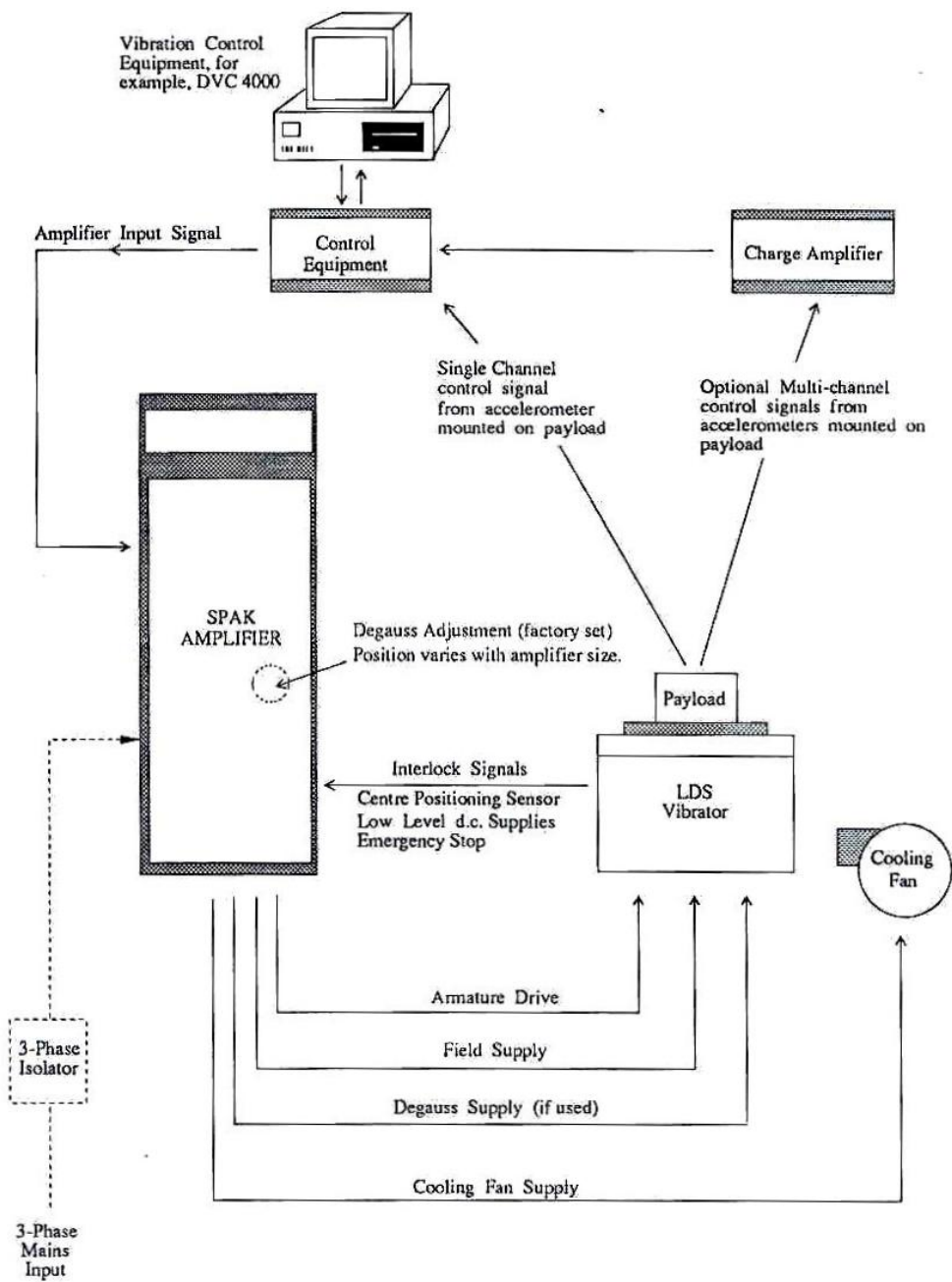


Figure 4-4: DACTRON vibration control system and SPAK amplifier



Customer responsibilities are tabulated on the Environmental Data Sheets, and are shown in dotted detail on interconnection diagrams.

Figure 4-5: Diagram of LDS vibration test system

4.2.3 Experimental Setup

A photograph showing the basic connector system experiment configuration is shown in Figure 4-6. This is the same setup as in Flowers and Xie's previous work [38]. As described in previous section, the connector system consists of 16 pin connector pairs for both the male and female terminals. Thus 16 wires were attached at each end of the connector and the other ends were clamped in the fixture. The blade terminal housing part was also clamped at the fixture to serve as an input of the system. In order to insure consistent fretting degradation in the frequency and amplitude ranges provided by the available laboratory shaker system, the supplementary inertial mass was clamped to the wire leads close to the connector housing, with a 2 mm gap between the connector housing and the mass. This inertial mass consisted of three plates, with one plate positioned between the two rows of wire leads and the other two plates on the outside of each row, with the resulting assembly clamped together with bolts.

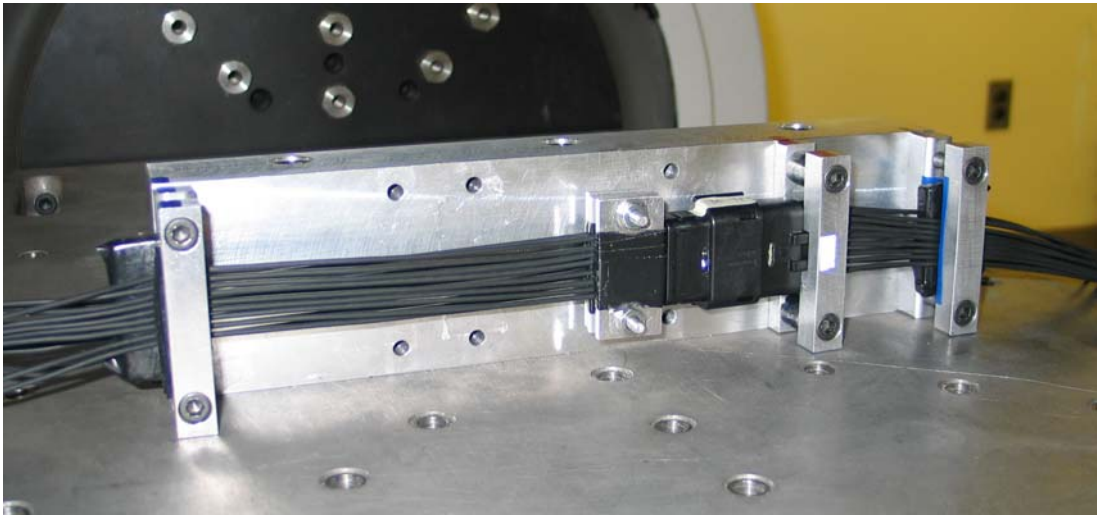


Figure 4-6: Photograph of the experimental setup

The typical transfer function testing setup is shown in Figure 4-7. This setup is based on the same methodology used in the transfer function measurements in Chapter 2.

Figure 4-8 shows a schematic diagram of the detailed test setup. The entire assembly was bolted to a horizontal slip table, which was driven by a vibratory shaker. The transfer function for each sample was then determined by comparing the output vibration response at the connector interface to the input excitation at the vibratory shaker head. Both are measured using Polytec non-contacting laser displacement measuring systems. The ratio of the steady-state output amplitude to the input amplitude for a given excitation frequency is the magnitude of the transfer function at that frequency. The phase difference between the steady-state output and input responses for a given frequency is the phase of the transfer function at that frequency.

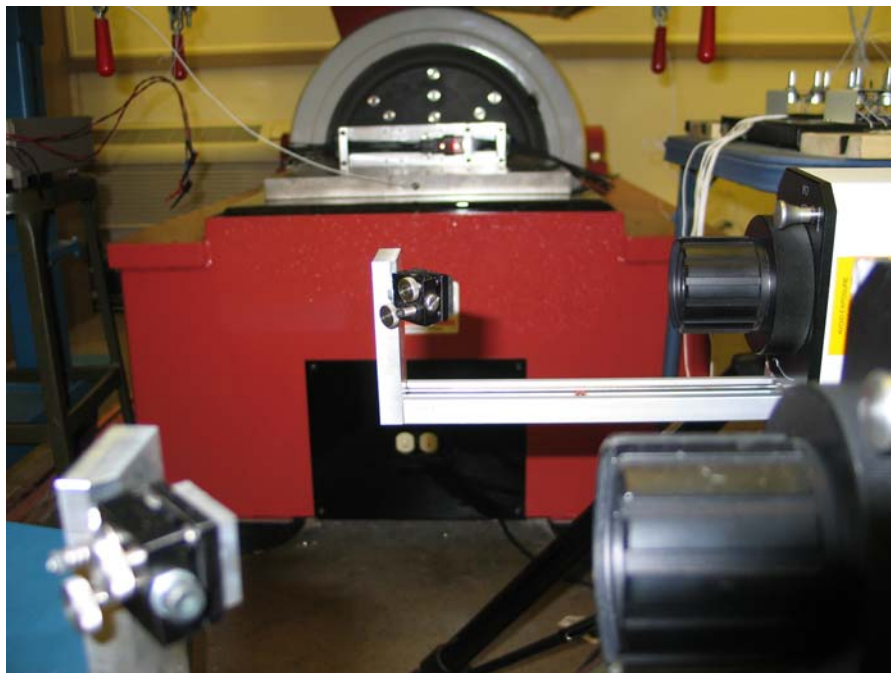


Figure 4-7: Photograph of transfer function measurement

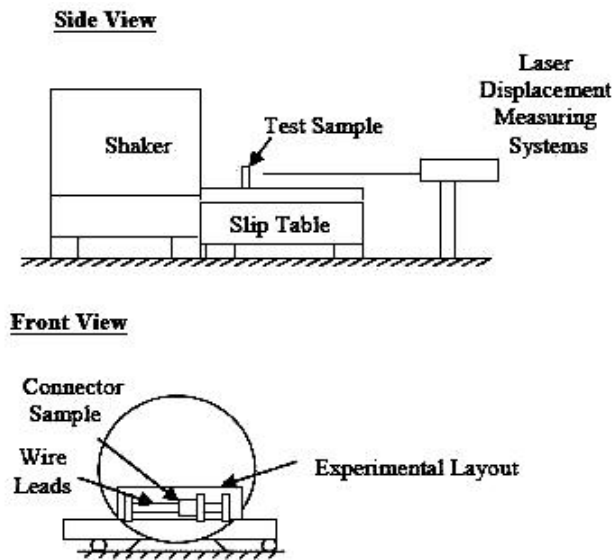


Figure 4-8: Diagram of transfer function measurement configuration

4.3 FEA Modeling

ABAQUS [14] finite element simulation models were developed based on the experimental configuration described above. A simplified two dimensional (2-D) and a detailed three dimensional (3-D) model were developed and compared. The workstation with multiple processors was utilized to reduce the computational time.

4.3.1 Detailed Three Dimensional Model

Figure 4-9 show the picture of the detailed 3-D model. This is a complicated model including most details of the experimental configuration. Sixteen blade/receptacle connector pairs were developed and sealed in a housing part. All the dimensions and material properties are the real value from the experiments. One crucial problem for the 3-D model is the optimization of the mesh size. In consideration of the convergence problem in the highly non-linear contact in this model, the springs and the contact pairs in

have to be finely meshed. Also the elements connected to these finely meshed elements cannot be meshed too coarse to insure the accuracy of the entire system. Based on these considerations, this model contains a very large volume of elements (92780 elements and 139267 nodes) and is expected to result in huge computational cost.



Figure 4-9: Picture of the 3-D detailed connector system model

4.3.2 Simplified Two Dimensional Model

In comparison, a simplified two dimensional model of the connector system was developed in ABAQUS. Figure 4-10 and Figure 4-11 show the overall view and detailed view of the 2-D model respectively. This model is basically a cross-section view of the connector system. The material properties and dimensions were adjusted similar to the 2-D model for single blade/receptacle connector pair described in Chapter 2. The wires in the blade part have been ignored because that the input location of the connector system in the experiment is at the blade-housing part, therefore the absence of these wires will

not have significant effect the dynamic response of the system. Three plates were also added on the wire to serve as the supplementary mass.

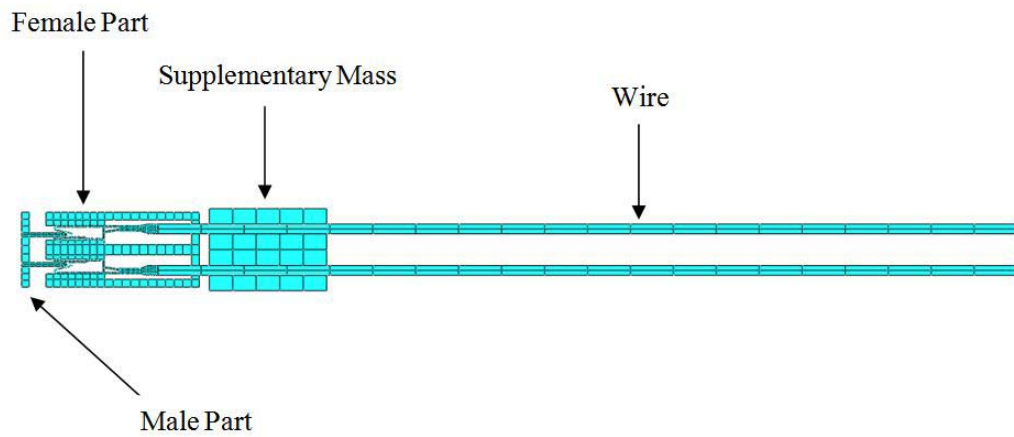


Figure 4-10: Overall view of the 2-D connector system model

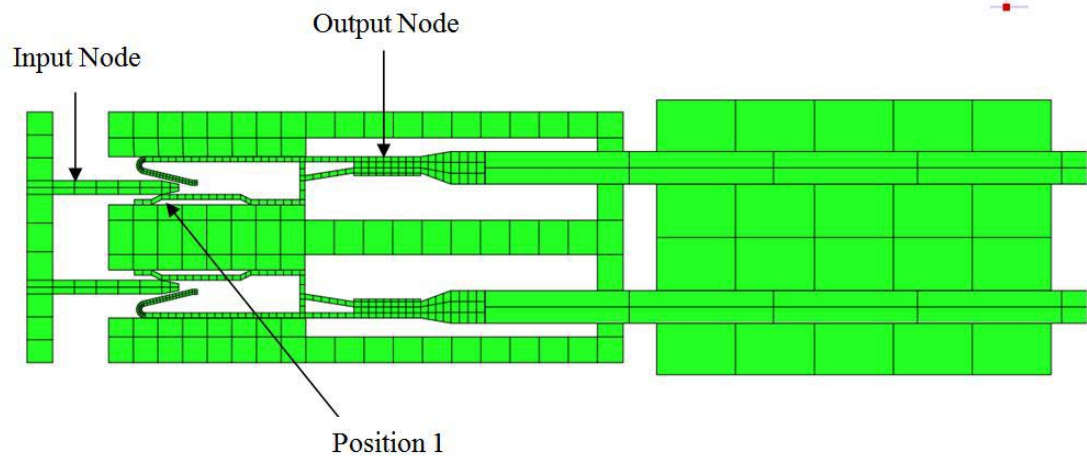


Figure 4-11: Detailed view of the 2-D connector system model

All elements in this model were meshed to hex elements by structure mesh technique. The spring part was especially finely meshed in consideration of contact convergence. Tie constrains were utilized for the connection between the supplementary

mass and wires, the housing part and connector pairs, etc. After optimization, this 2-D simplified model has only 1270 elements and 1916 nodes. Compared with the 92780 elements and 139267 nodes in 3-D detailed model, this 2-D simplified model is expected to be more practical and could significantly reduce the computational time.

4.3.3 Comparison between 2-D and 3-D Model

An initial mating-process simulation (move the blade part into receptacle part to connect the entire system) was performed on both 3-D and 2-D models to compare the computational cost. As shown in Figure 4-11, it takes about 3154 minutes to finish for the 3-D model while takes only 0.5 minute for the 2-D model, which is approximately more than 6000 times. As expected, the large volume of elements required for this detailed 3-D model and more defined constrains and contact areas tend to result in much more computational cost. The present computational capacity could not meet the requirement of this complicated model. Therefore, the 2-D simplified model is proved to be a more practical tool to investigate the fretting characteristics of this connector system.

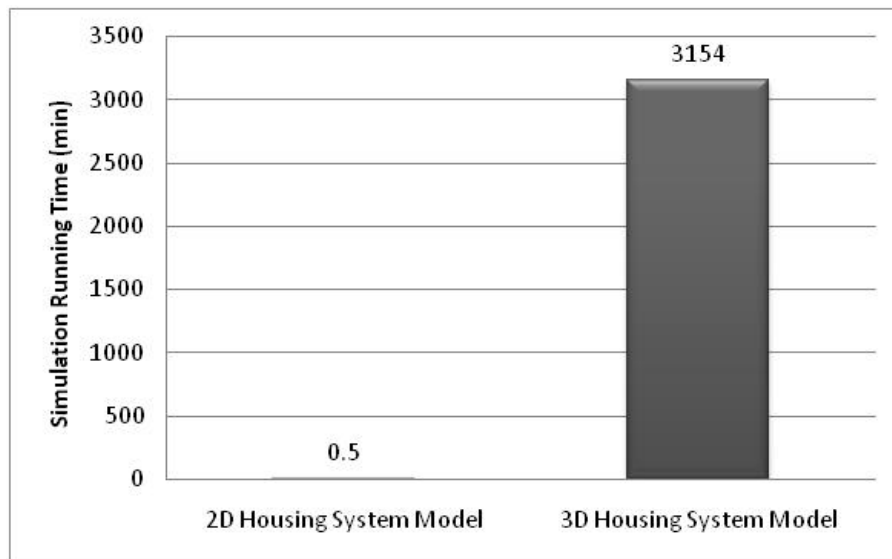


Figure 4-12: Comparison of computational cost for initial simulation between 2-D model and 3-D model

4.4 Experiment and Simulation Results

Based upon the system configuration described above, a series of simulation studies were performed to evaluate the fretting behavior. Corresponding experiments were conducted to validate it.

4.4.1 Transfer Function

Transfer functions were proved to be the great indicator of the fretting behavior, as described in previous chapters. The input and output measurement locations for both the simulation and experiments were selected to be the same. The specific positions are shown as input and output node in the 2-D model in Figure 4-11. Example transfer functions for Type 1.b and Type 2.b obtained from both experimentally and using the simulation model, are shown and compared in Figure 4-12. It can be observed from the comparison that the simulation results generally matches overall shape of the

experimentally measured results very well. The frequency where the highest peak occurs appears to be very similar between experiment and simulation results. For Type1, the frequency value generated from simulation is 125.1Hz compared with 124Hz from experiment; for Type2, the value decreased to 121.6Hz and 123Hz. The magnitudes of the first resonant peak from the simulation results are only about 2.76% and 6.21% higher than those from the experiment for Type 1 and Type 2 respectively. Please note that there's a significant difference in magnitude between two different types.

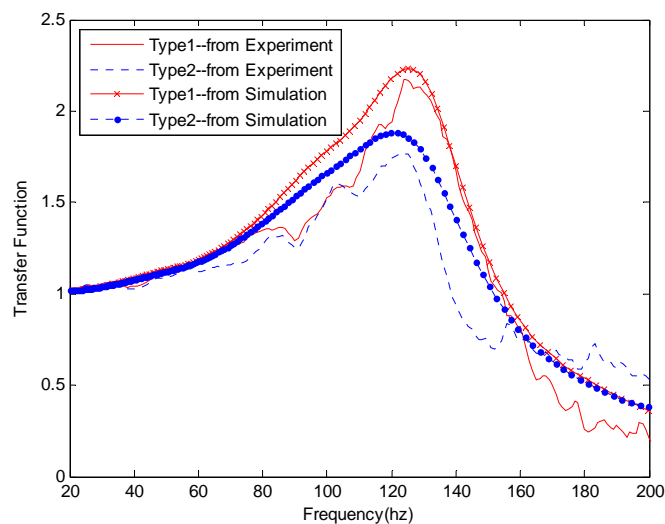


Figure 4-13: Comparison of experimentally determined transfer function and 2-D model simulation results

Figure 4-14, Figure 4-15, Figure 4-16 and Figure 4-17 show the transfer function results which were obtained from experimental testing and 2-D model simulation for different finish/base metal type and contact normal force levels respectively. As observed from the experiment results in Figure 4-14 and Figure 4-16, the magnitude of the first resonant peak of Type 1 samples is about 20% higher than the Type 2 samples. So it appears that the resonant frequency and the associated amplitude peak for the higher friction finish (Type 1) were somewhat higher. Moreover, as the normal force level is

increased, the magnitude of the first resonant peak of transfer function tends to be correspondingly increased. As shown in Figure 4-15 and Figure 4-17, the same phenomenon could be predicted by the 2-D model simulation very well. It could be observed from the simulation results that for both type of finish, the magnitude of Type c with the highest contact normal force is larger than Type b, while that of Type b is larger than Type a, which has the lowest contact normal force.

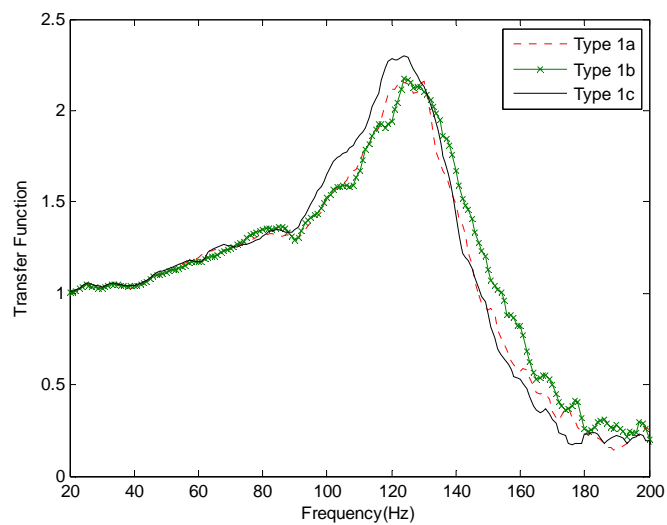


Figure 4-14: Experimental determined transfer function results for different contact normal force levels of specimen Type 1

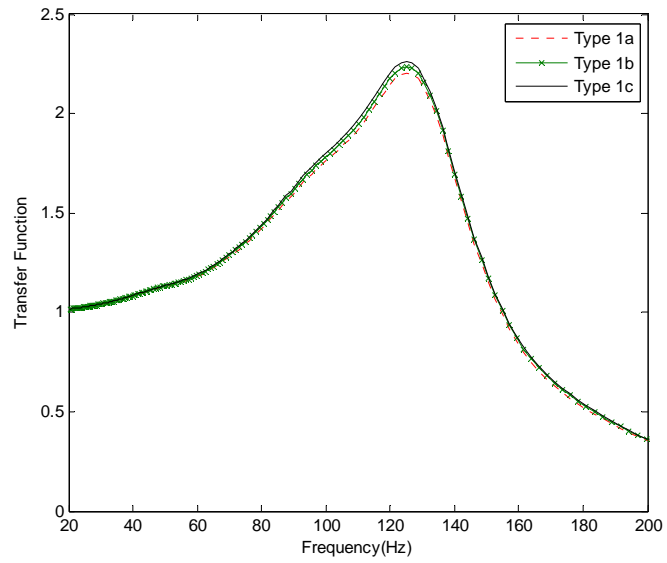


Figure 4-15: Simulation transfer function results for different contact normal force levels of specimen Type 1

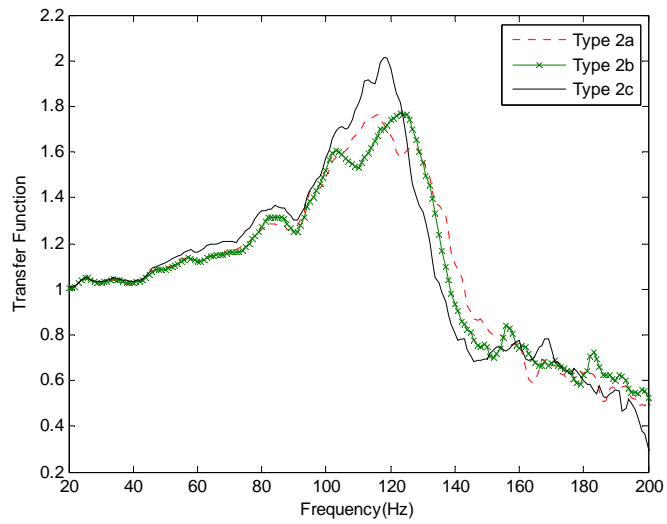


Figure 4-16: Experimental determined transfer function results for different contact normal force levels of specimen Type 2

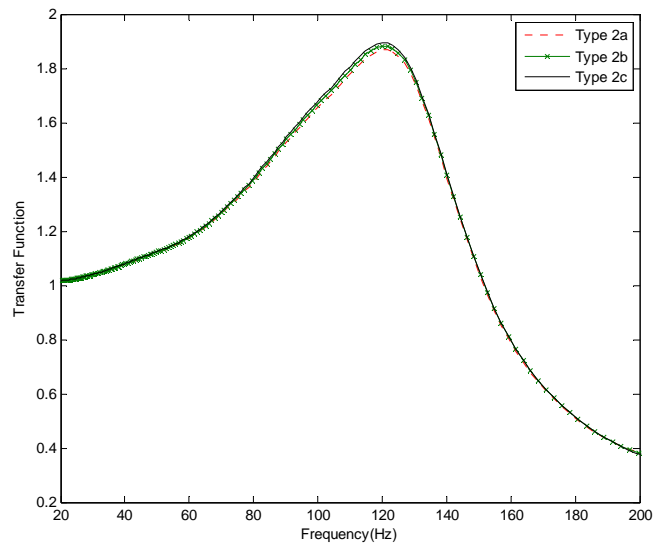


Figure 4-17: Simulation transfer function results for different contact normal force levels of specimen Type 2

4.4.2 Fretting Rate

Fretting rate experiments were performed for each type of samples at 90Hz by Flowers and Xie [38]. The different g-levels (acceleration of the shaker head) used in the experiments were calculated and transferred to be the input excitation displacement in the vibration simulation. Table 4-3 shows g-levels and corresponding displacements. The x-axis relative motion at position 1 was selected as a great indicator for the fretting corrosion in simulation. In this particular 2-D connector system model, position 1 was the point of the contact between the blade and the left inner bottom surface of the receptacle during the rocking motion as shown in Figure 4-11.

Table 4-2: G-levels and corresponding displacements at shaker head

G-level	Peak-to-peak displacement at shaker head
2g	0.06135mm
4g	0.12265mm
6g	0.18400mm

From Figure 4-18 and Figure 4-19, it could be observed that for each sample type, as the increment of contact normal force, the x-axis relative motion at position 1 generally increased. In another word, the x-axis relative motion amplitude of Type c is larger than that of Type b, while Type b is larger than Type a. Moreover, the comparison of the results of the two finish types showed the significant differences between the relative motions, with the higher friction finish having markedly higher x-axis relative motion amplitude. These results show a great agreement with the Flowers and Xie's previous work [38] of fretting rate in experiments in Figure 4-20 and Figure 4-21. The experimental results indicated that as the increase of the contact normal force, the fretting rate (rate of resistance changes) generally increased (except type 2b) too. Meanwhile, the fretting rate results for Type 1 with higher friction finish is larger than Type 2, with the slopes of the linear regression line are approximately 0.12 and 0.06 respectively. This phenomenon is generally in good agreement with the transfer function results. The magnitude of the transfer function is increased as the increase of the contact normal force and the magnitude of Type 1 is larger than Type 2.

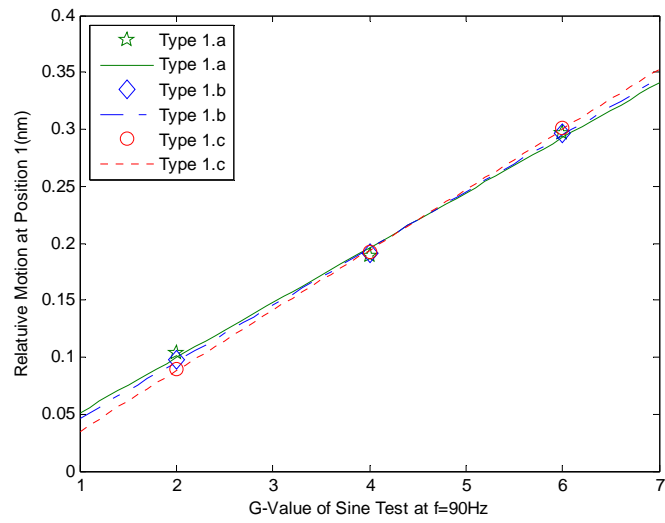


Figure 4-18: X-axis relative motion for different contact normal force levels for specimen Type 1 in simulation

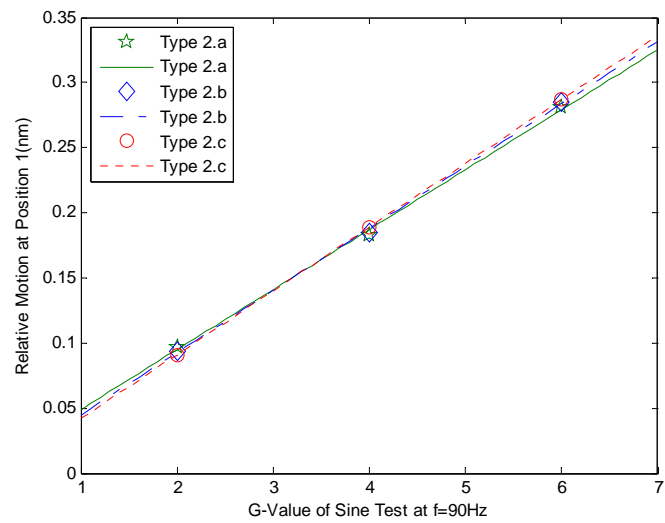


Figure 4-19: X-axis relative motion for different contact normal force levels for specimen Type 2 in simulation

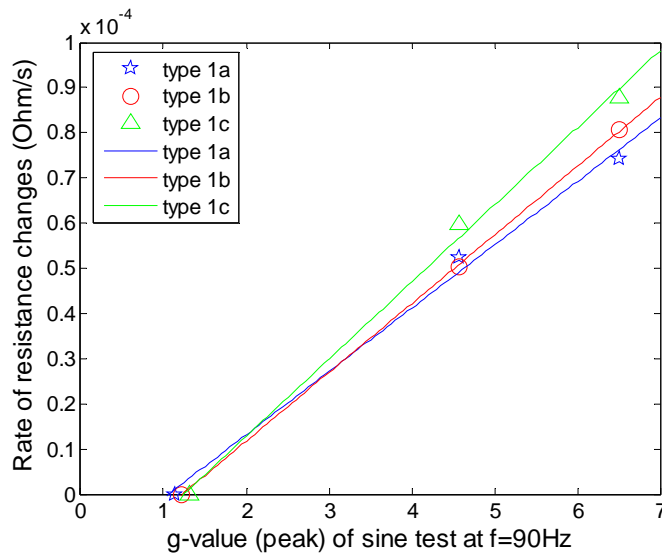


Figure 4-20: Rate of resistance change for Type 1 sample in experiment

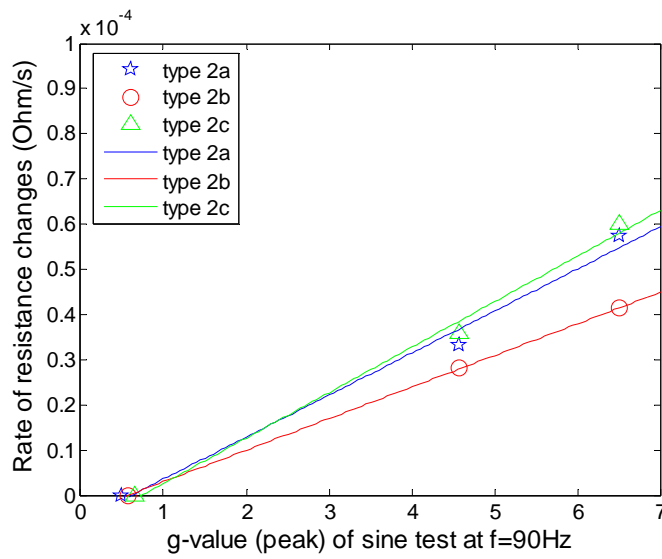


Figure 4-21: Rate of resistance change for Type 2 sample in experiment

Both results from experiment and simulation tend to follow the basic theory which was developed as part of earlier work on this topic [38]. In that work, it was observed that the fretting degradation rate satisfied the relationship:

$$\frac{d\Delta R}{dt} = E \frac{Z_F}{f^2} (G_f - G_{f,threshold}) f \quad (1)$$

where Z_F is the magnitude of the transfer function relating the relative motion between mating terminals (nominally equivalent to the motion of the “output” terminal relative to the “input” shaker head), G_f is the G-level acceleration of the shaker head, $G_{f,threshold}$ is the threshold vibration of the shaker head before the onset of fretting, f is the frequency of vibration, and E is a scaling factor. It is obviously from the relationship that as the increase of relative motion between mating terminals (E.g. position 1 in Figure 4-11 in simulation), the fretting rate should (rate of resistance changes) correspondingly increase. This relationship was proved by the trend shown in both simulation and experiment results. This value is in building a reasonable and consistent relationship between the experiment and simulation results.

4.5 Summary and Conclusions

A study of the application of FEA simulation techniques to vibration-induced fretting degradation of a connector system was presented. Two variations of surface finish types of connector systems were considered, with each type having three different contact normal force levels. The transfer functions and the fretting rate at certain frequency were measured in the experiment. A detailed 3-D model and a simplified 2-D model were developed and compared using ABAQUS for the connector system. The geometric dimensions, material properties and boundary conditions of both models were generated based on the experimental values. The 2-D finite element model was selected to be a better simulation tool especially in consideration of the computational cost. A series of simulations were performed on the 2-D housing connector model and

corresponding experiments were conducted to validate and test the performance of the system. Finally, the results from the simulation were compared with the results from the experiment and generally found to be in good agreement. It was demonstrated that, for this connector system, finite element modeling and analysis has enough potential to evaluate of the influence of design variations on the fretting behavior. This study's findings can be summarized and concluded as follows:

- Fretting rate and transfer function results were measured for all six types of samples in both experiment and simulation.
- The 2-D simplified model was proved to be a better tool than 3-D detailed model, especially in consideration of the computational cost.
- The relationship between the relative motion function and the fretting rate for this connector system was found in good agreement with the fretting degradation relationship concluded in previous study.
- The results from the simulation generally correlated well with that obtained from the experiment.
- Finite element modeling and analysis methodology has great potential for evaluating the influence of design variations on fretting behavior of the connector system.

CHAPTER 5 CONCLUSIONS AND RECOMMENDATIONS

A study of the prediction of vibration-induced fretting corrosion in electrical contacts has been described in this dissertation. Simulation-based modeling and analysis method accompany with corresponding experimental validations were conducted to evaluate the influences of different connector design factors on fretting behaviors of connectors. The dissertation consists of three chapters.

First of all, a research on vibration-induced fretting corrosion in a single blade/receptacle connector pair is introduced. A two dimensional (2-D) simplified finite element model was developed in ANSYS [11] based on the typical experimental configurations. The model was then optimized, simulated and experimentally validated. The relative motion transfer function was proved to be a good indicator of the tendency of such systems to fret. The same x-axis relative motion at the contact interfaces was observed when the experimental threshold displacements were used as the input vibration levels for this single blade/receptacle pair system. The results from the simulation were finally compared with the results from the experiment and generally found to be in good agreement. This finding proved that for this limited system, finite element modeling and analysis methodology is a potentially tool for the evaluation of the influence of design variations on the fretting behavior of connector.

In the second part, a three-dimensional modeling and analysis method for the same connector configuration was studied. A highly detailed 3-D finite element model

was developed in ABAQUS [14] according to true dimensions and boundary conditions of the blade/receptacle connector pair configuration in the experiments. A high-performance workstation as well as the parallel execution technology was utilized to increase the computational speed. The 3-D detailed model was then optimized and analyzed to evaluate the threshold vibration levels as a function of excitation frequency, wire tie-off length, supplementary mass, interface friction coefficient, and normal force. The 3-D simulation results were compared with the results from the 2-D simplified model simulation and the experimental results. The 3-D simulation correlated very well with the experiment and was proved to be practical and more adaptable than the 2-D simulation for this connector pair configuration.

The third study presented a study of the application of FEA simulation techniques to vibration-induced fretting degradation of a connector system. The connector system consists of 16 blade/receptacle connector pairs and the housing part. A detailed 3-D FEA model and a simplified 2-D FEA model were developed and compared using ABAQUS. The 2-D finite element model was proved to be a better tool in consideration of the computational cost. A series of simulations were performed on the 2-D housing connector model and corresponding experiments were conducted to validate and test the performance of the system. After comparison, the simulation results from the 2-D housing model generally match the experiments very well. It was demonstrated that, for this connector system configuration, finite element modeling and analysis has enough potential to evaluate of the influence of design variations on the fretting behavior.

There is certainly a great deal of fertile ground for further investigations on the topic of vibration-induced fretting corrosion. Some suggestions for future work in this area are:

- Investigation and prediction of the effects of contaminants on vibration-induced fretting degradation in electrical connectors.
- Detailed experimental and simulation analysis of surface profile and material composition at the contact interfaces to study the fretting mechanism.
- Study of the wear effect in connector systems.
- Optimization and simplification of the three-dimensional finite element model of the connector system to make it practical.
- Simplified computational mechanics model for connector systems in Matlab or C++ for industry applications.

REFERENCES

- [1] Ed P. Slade, "Electrical Contacts: Principles and Applications", Chapter 6, 1990.
- [2] D.V. Hutton, "Fundamentals of Finite Element Analysis", 2004.
- [3] L. Rayleigh, "On the Theory of Resonance", *Transactions of the Royal Society (London)*, A161 (1870).
- [4] W. Ritz, "Uber eine neue Methode zur Losung gewissen Variations-Probleme der mathematischen Physik", *J.Reine Angew.Math.*, 135(1909).
- [5] B.G. Galerkin, "Series Solution of Some Problems of Elastic Equilibrium and Rods and Plates", *Vestn.Inzh.Tekh*, 19(1915).
- [6] R. Courant, "Variational Methods for the Solution of Problems of Equilibrium and Vibrations", *Bulletin of the American Mathematical Society*, 49(1943).
- [7] R.W. Clough, "The Finite Element Method in Plane Stress Analysis", *Proceedings, American Society of Civil Engineering, Second Conference on Electronic Computation*, Pittsburgh, 1960.
- [8] H,C, Martin, "Finite Element Analysis of Fluid Flows", *Proceedings of the Second Conference on Matrix Methods in Structural Mechanics*, Wight-Patterson Air Force Base, Kilborn, Ohio, Oct. 1968.

- [9] E.L. Wilson and R.E. Nickell, "Application of the Finite Element Method to Heat Conduction Analysis", *Nuclear Engineering Design*, 4(1966).
- [10] MSC/NASTRAN. Lowell, MA: MacNeal-Schwindler Corp.
- [11] ANSYS. Houston, PA: Swanson Analysis Systems. Inc.
- [12] ALGOR. Pittsburgh: Algor Interactive Systems.
- [13] COSMOS/M. Los Angeles: Structural Research and Analysis Corp.
- [14] ABAQUS, Providence, RI: Dassault Systemes Simulia Corp.
- [15] E.M. Bock and J.H. Whitley, "Fretting Corrosion in Electric Contacts", *Electric Contacts -1974*, Chicago, 1974, p.128.
- [16] S. Krumbein, "Contact Properties of Tin Plates", *Electric Contacts -1974*, Chicago, 1974, p.38.
- [17] M. Antler, W.F. Graddick and H.G. Tompkins, "Base Metal Contacts: An Exploratory Study of Separable Connection To Tin-Lead", *Electric Contacts - 1975*, Chicago, 1975, p.25.
- [18] J.H. Whitley, "Investigation of Fretting Corrosion Phenomena in Electric Contacts", *Proc. 8th Int. Conf. Electrical Contact Phenomena*, Tokyo, 1976, pp.659-665.
- [19] M. Antler, and E.S. Sproles, "Effect of Fretting on the Contact Resistance of Palladium", *IEEE Trans. CHMT*, V.5, N.1, 1982, p.158.
- [20] J.M. Hooyer and K. Peekstok, "The Influence of Practical Contact Parameters on Fretting Corrosion of Tin-Base Low-Level Connector Contacts", *Electric Contacts -1987, IEEE - HOLM*, Chicago, 1987, p.43.

- [21] M. Antler, "Survey of Contact Fretting in Electrical Contacts", *Proceedings of the Twenty Ninth IEEE Holm Conference on Electrical Contacts*, 1984, pp.3-22.
- [22] A. Lee and M.S. Mamrick, "Fretting Corrosion of Tin with Electrical Load", *Proc. 13 International Conference On Electric Contacts*, Lausanne, Switzerland, 1986, p.476.
- [23] A. Lee and M.S. Mamrick, "Fretting Corrosion of Tin-Plated Copper Alloy", *IEEE Trans. CHMT – 10*, 1987, p.63.
- [24] A.Lee and M.S.Mamrick "Fretting Corrosion of Tin at Elevated Temperatures" *Proceedings of the Thirty Fourth IEEE Holm Conference on Electrical Contacts*, 1988, p. 87-91.
- [25] J. Swingler, J.W. McBride, and C. Maul, "The Degradation of Road Tested Automotive Connectors", *IEEE Transactions on Components and Packaging Technologies (CPMT)*, 2000, 23(1), p. 157-164.
- [26] G. T. Flowers, F. Xie, M. Bozack, and R.D. Malucci, "Vibration Thresholds for Fretting Corrosion in Electrical Connectors," *Proceedings of the 48th IEEE Holm Conference on Electrical Connectors*, October 21-23, 2002, pp.133-139.
- [27] L. Lam, J. W. McBride, C. Maul, and J. K. Atkinson, "Displacement Measurements at the Connector Contact Interface Employing a Novel Thick Film Sensor", *Electrical Contacts, 2005. Proceedings of the Fifty-First IEEE Holm Conference on 26-28 Sept. 2005*, pp. 89 – 96.

- [28] N. Ben Jemaa, E. Carvou, “Electrical contact behavior of power connector during fretting vibration”, *Proceedings of the 52nd IEEE Holm Conference on Electrical Connectors*, 25-27 Sept. 2006, pp. 263 – 266.
- [29] M.D. Bryant, “Resistance Buildup in Electrical Connectors Due To Fretting Corrosion of Rough Surfaces”, *IEEE Transactions on Components Packaging and Manufacturing Technology*, V.17, N.1, March 1994, pp. 86-95.
- [30] R. D. Malucci, “Multispot Model of Contacts Based on Surface Features”, *Electric Contacts -1990, IEEE - HOLM*, Montreal, 1990, p. 625.
- [31] R. D. Malucci, “Impact of Fretting Parameters on Contact Degradation”, *Proceedings of the 42nd IEEE Holm Conference on Electrical Contacts*, 1996, pp. 395-403.
- [32] G. Villeneuve, D. Kulkarni, P. Bastnagel, and D. Berry, “Dynamic Finite Element Analysis Simulation of the Terminal Crimping Process”, *Electrical Contacts, 1996., Proceedings of the Forty-Second IEEE Holm Conference Joint with the 18th International Conference on Electrical Contacts*, Sept. 1996 pp. 156-172.
- [33] A. Monnier, B. Froidurot, C. Jarrige, R. Meyer, and P. Teste, “A Mechanical, Electrical, Thermal Coupled-field Simulation of a Sphere-plane Electrical Contact”, *Proceedings of the 51st IEEE Holm Conference on electrical Contacts*, 26-28 Sept. 2005 pp. 224-231.
- [34] S.V. Angadi, W.E. Wilson, R.L. Jackson, Flowers, G.T. and B.I. Rickett, “A Multi-Physics Finite Element Model of an Electrical Connector Considering

- Rough Surface Contact”, *Proceedings of the 54th IEEE Holm Conference on electrical Contacts*, 27-29 Oct. 2008 pp. 168-177.
- [35] C. Leung, E. Streicher, D. Fitzgerald, and J. Cook, “Contact Erosion of Ag/SnO₂/In₂O₃ Made by Internal Oxidation and Powder Metallurgy”, *Electrical Contacts, 2005. Proceedings of the Fifty-First IEEE Holm Conference on 26-28 Sept. 2005* Page(s):22 – 27.
- [36] E. D. Taylor; “Cathode Spot Behavior on Tungsten-Copper Contacts in Vacuum and the Effect on Erosion”, *Electrical Contacts, 2005. Proceedings of the Fifty-First IEEE Holm Conference on 26-28 Sept. 2005* Page(s):135 – 138.
- [37] A. Gunatilake, S. Rowland, Z. Wang, and N. Allen, “Modeling and Management of Microshocks under High Voltage Transmission Lines”, *Electrical Contacts, 2005. Proceedings of the Fifty-First IEEE Holm Conference on 26-28 Sept. 2005* Page(s):63 – 68.
- [38] G. Flowers, F. Xie, M. Bozack, B. Rickett, and R. Malucci, “The Influence of Contact Interface Characteristics on Vibration-Induced Fretting Degradation”, *Electrical Contacts, 2005. Proceedings of the Fifty-First IEEE Holm Conference on 26-28 Sept. 2005* Page(s):82 – 88.
- [39] M. Braunovic, V. Izmailov, and M. Novoselova, “A Model for Life Time Evaluation of Closed Electrical Contacts”, *Electrical Contacts, 2005. Proceedings of the Fifty-First IEEE Holm Conference on 26-28 Sept. 2005* Page(s):217 – 223.

- [40] D. J. Dickrell; M. T. Dugger, “The Effects of Surface Contamination on Resistance Degradation of Hot-Switched Low-Force MEMS Electrical Contacts”, *Electrical Contacts, 2005. Proceedings of the Fifty-First IEEE Holm Conference on 26-28 Sept. 2005* Page(s):255 – 258.
- [41] E. Takano, “Equivalent Constriction Resistance Measured with the Low Dc Voltage Method under the Influence of Fretting Phenomena”, *Electrical Contacts, 2005. Proceedings of the Fifty-First IEEE Holm Conference on 26-28 Sept. 2005* Page(s):284 – 290.
- [42] T. Ueno, and N. Morita, “Influence of Surface Roughness on Contact Voltage Drop of Sliding Contacts”, *Electrical Contacts, 2005. Proceedings of the Fifty-First IEEE Holm Conference on 26-28 Sept. 2005* Page(s):324 – 328.
- [43] D. Sallais, N. Jemaa, E. Carou, C. Bourda, and D. Jeannot, “An Arc Study at High DC Current Levels in Automotive Applications”, *Electrical Contacts, 2005. Proceedings of the Fifty-First IEEE Holm Conference on 26-28 Sept. 2005* Page(s):329 – 334.
- [44] J. Aronstein, “Performance Classification for Electrical Connection Using ASTM B868”, *Electrical Contacts, 2005. Proceedings of the Fifty-First IEEE Holm Conference on 26-28 Sept. 2005* Page(s):162 – 166.
- [45] F. Xie, , G. Flowers, , C. Chen, M. Bozack, J. Suhling, B. Rickett, R. Malucci, C. Manlapaz, "Analysis and Prediction of Vibration-Induced Fretting Motion in a Blade/Receptacle Connector Pair," *Proceedings of 53rd IEEE HOLM Conference on Electrical Contacts*, pp. 222-228, PITTSBURGH, PA, Sept 16-19, 2007.

- [46] Model 2010 Multimeter User's Manual, Keithley Instruments, Inc., USA, 1999
- [47] Laser Vibrometer User Manual, Controller OFV-2610/2620, Sensor Head OFV-353, POLYTEC Co., Germany
- [48] HP 35665A Dynamic Signal Analyzer Installation and Verification Guide, Hewlett-Packard Company, USA, 1991
- [49] Installation and Operating Manual PA 500/1000L-CE Amplifiers, LDS Company, USA
- [50] Installation and Operating Manual V400 Series Vibrators, LDS Company, USA
- [51] G. T. Flowers, F. Xie, M. Bozack, R. Horvath, R. D. Malucci, and B. Rickett., "Vibration Testing of Fretting Corrosion in Electrical Connectors Subjected to Multi-Frequency and Random Spectral Profiles," *Proceedings of the 49th IEEE Holm Conference on Electrical Contacts*, pp. 45-50, Washington, DC, September 8-10, 2003.
- [52] G. T. Flowers, F. Xie, M. Bozack, X. Hai, B. Rickett and R. D. Malucci, "A Study of the Physical Characteristics of Vibration Induced Fretting Corrosion," *Proceedings of the 50th IEEE Holm Conference on Electrical Contacts*, pp. 312-319, Washington, DC, September 20-23, 2004.
- [53] B. Malucci, "Fretting Corrosion Degradation, Threshold Behavior and Contact Instability", Ragnar Holm Scientific Achievement Award Address, *Proceedings of the 49th IEEE Holm Conference on Electrical Contacts*, pp. 1-15, Washington, D.C., September 8-10, 2003.

- [54] Hammam, Tag, Kassman-Rudolphi, Asa, and Lundstrom, Per, “Vibration-induced deterioration of in-coated connectors studied by using a force controlled fretting bench-test,” *Proceedings of the Fifty-First IEEE Holm Conference on Electrical Contacts*, 2005, p 97-106, Sep 26-28 2005.
- [55] V850 Vibration Testing Systems Manual, LDS Company, USA
- [56] Laser Shaker Control System Guide, Dactron Incorporated, Milpitas, CA95035
- [57] Unpublished data, Professor M. J. Bozack, Surface Science Laboratory, Department of Physics, Auburn Univ

**APPENDIX A ANSYS LOG FILE FOR THE 2-D SIMPLIFIED FINITE
ELEMENT MODEL**

```
!* Modeling generation

/PREP7
!*
!*set element type as plane42 with thickness*!
ET,1,PLANE42
!*
KEYOPT,1,1,0
KEYOPT,1,2,0
KEYOPT,1,3,3
KEYOPT,1,5,0
KEYOPT,1,6,0
!*
!*thickness set1=2.55e-3 for receptacle*!
R,1,2.55e-3,
!*
!*thickness set2=1.90e-3 for partial annulus*!
R,2,0.0019,
!*
!*thickness set3=1.50e-3 for blade and spring*!
R,3,0.0015,
!*
R,4,0.00112,
!*

!*set material properties*!

!*type1-C19025-Star: blade,annulus*!
MPTEMP,,,,,,,,
MPTEMP,1,0
MPDATA,EX,1,,1.29742e11
MPDATA,PRXY,1,,0.3
MPTEMP,,,,,,,,
MPTEMP,1,0
MPDATA,DENS,1,,8910
```

MPTEMP,,,,,,,,
MPTEMP,1,0
MPDATA,MU,1,,0.33

!*type2-star: spring*!

MPTEMP,,,,,,,,
MPTEMP,1,0
MPDATA,EX,2,,1.29742e11
MPDATA,PRXY,2,,0.3
MPTEMP,,,,,,,,
MPTEMP,1,0
MPDATA,DENS,2,,8910
MPTEMP,,,,,,,,
MPTEMP,1,0
MPDATA,MU,2,,0.33
MPTEMP,,,,,,,,
MPTEMP,1,0
MPDATA,DAMP,2,,0.000

!*type3: wire for 2D model*!

MPTEMP,,,,,,,,
MPTEMP,1,0
MPDATA,EX,3,,1.35e9
MPDATA,PRXY,3,,0.3
MPTEMP,,,,,,,,
MPTEMP,1,0
MPDATA,DENS,3,,4564
MPTEMP,,,,,,,,
MPTEMP,1,0
MPDATA,DAMP,3,,0.0005

!*type4: Balls for 2D model*!

MPTEMP,,,,,,,,
MPTEMP,1,0
MPDATA,EX,4,,1.95e11
MPDATA,PRXY,4,,0.3
MPTEMP,,,,,,,,
MPTEMP,1,0
MPDATA,DENS,4,,12876.3

!*type5-C19025-Star-equivalent: receptacle*!

MPTEMP,,,,,,,,
MPTEMP,1,0
MPDATA,EX,5,,1.29742e14
MPDATA,PRXY,5,,0.3

MPTEMP,,,,,,,,
MPTEMP,1,0
MPDATA,DENS,5,,8794
MPTEMP,,,,,,,,
MPTEMP,1,0
MPDATA,MU,5,,0.33

!*type6-klf5-Reflow-equivqlent*!

MPTEMP,,,,,,,,
MPTEMP,1,0
MPDATA,EX,6,,1.20622e14
MPDATA,PRXY,6,,0.3
MPTEMP,,,,,,,,
MPTEMP,1,0
MPDATA,DENS,6,,3210
MPTEMP,,,,,,,,
MPTEMP,1,0
MPDATA,MU,6,,0.44

!*type7: blade rear part*!

MPTEMP,,,,,,,,
MPTEMP,1,0
MPDATA,EX,7,,1.29742e11
MPDATA,PRXY,7,,0.3
MPTEMP,,,,,,,,
MPTEMP,1,0
MPDATA,DENS,7,,6974.3
MPTEMP,,,,,,,,
MPTEMP,1,0
MPDATA,MU,7,,0.33
!!MPTEMP,,,,,,,,
!!MPTEMP,1,0
!!MPDATA,DAMP,7,,0.001

!*type8: end rectangle of spring*!

MPTEMP,,,,,,,,
MPTEMP,1,0
MPDATA,EX,8,,1.29742e11
MPDATA,PRXY,8,,0.3
MPTEMP,,,,,,,,
MPTEMP,1,0
MPDATA,DENS,8,,8910
MPTEMP,,,,,,,,
MPTEMP,1,0
MPDATA,MU,8,,0.33

```
!*generate blade*!  
K,1,0,0,,  
K,2,0,0.8e-3,,  
K,3,7.85e-3,0.8e-3,,  
K,4,7.85e-3,0,,  
K,5,8.85e-3,0.2e-3,,  
K,6,8.85e-3,0.6e-3,,  
K,7,-9.0e-3,0,,  
K,8,-9.0e-3,0.8e-3,,
```

```
FLST,2,4,3  
FITEM,2,1  
FITEM,2,2  
FITEM,2,3  
FITEM,2,4  
A,P51X
```

```
FLST,2,4,3  
FITEM,2,3  
FITEM,2,4  
FITEM,2,5  
FITEM,2,6  
A,P51X
```

```
FLST,2,4,3  
FITEM,2,1  
FITEM,2,2  
FITEM,2,8  
FITEM,2,7  
A,P51X
```

```
!*generate receptacle--front part*!  
RECTNG,0,1.0e-3,-0.6e-3,-0.3e-3,
```

```
!!RECTNG,2.0e-3,2.15e-3,-0.3e-3,0,  
RECTNG,1.6e-3,2.15e-3,-0.3e-3,0,  
RECTNG,2.15e-3,5.45e-3,-0.3e-3,0,  
!!RECTNG,5.45e-3,5.6e-3,-0.3e-3,0,  
RECTNG,5.45e-3,6.2e-3,-0.3e-3,0,
```

```
RECTNG,2.15e-3,5.45e-3,-0.6e-3,-0.3e-3,
```

```
RECTNG,6.80e-3,9.65e-3,-0.6e-3,-0.3e-3,  
RECTNG,9.65e-3,9.95e-3,-0.6e-3,-0.3e-3,
```

```
FLST,2,4,3
```

FITEM,2,11
FITEM,2,10
FITEM,2,13
FITEM,2,16
A,P51X
FLST,2,4,3
FITEM,2,22
FITEM,2,29
FITEM,2,32
FITEM,2,23
A,P51X

CYL4,0.63e-3,1.70e-3,0.2e-3,90,0.5e-3,257
RECTNG,3.37e-3,3.67e-3,0.48e-3,0.78e-3,

FLST,2,4,3
FITEM,2,39
FITEM,2,38
FITEM,2,41
FITEM,2,44
A,P51X

RECTNG,0.63e-3,9.65e-3,1.90e-3,2.20e-3,
RECTNG,9.65e-3,9.95e-3,1.90e-3,2.20e-3,

RECTNG,9.65e-3,9.95e-3,-0.30e-3,0.8e-3,
RECTNG,9.65e-3,9.95e-3,0.80e-3,1.10e-3,
RECTNG,9.65e-3,9.95e-3,1.10e-3,1.90e-3,

!*generate receptacle--rear part*!
RECTNG,9.95e-3,12.80e-3,1.90e-3,2.20e-3,

RECTNG,12.80e-3,13.10e-3,1.90e-3,2.20e-3,
RECTNG,12.80e-3,13.10e-3,1.55e-3,1.90e-3,
RECTNG,12.80e-3,13.10e-3,1.25e-3,1.55e-3,
RECTNG,12.80e-3,13.10e-3,1.10e-3,1.25e-3,

FLST,2,4,3
FITEM,2,59
FITEM,2,55
FITEM,2,77
FITEM,2,73
A,P51X

RECTNG,13.10e-3,16.70e-3,1.90e-3,2.20e-3,
RECTNG,13.10e-3,16.70e-3,1.55e-3,1.90e-3,

RECTNG,13.10e-3,16.70e-3,1.25e-3,1.55e-3,
RECTNG,13.10e-3,16.70e-3,1.10e-3,1.25e-3,

RECTNG,18.45e-3,20.45e-3,2.20e-3,2.50e-3,
RECTNG,18.45e-3,20.45e-3,1.40e-3,2.20e-3,
RECTNG,18.45e-3,20.45e-3,1.10e-3,1.40e-3,
RECTNG,18.45e-3,20.45e-3,0.60e-3,1.10e-3,

FLST,2,4,3
FITEM,2,87
FITEM,2,86
FITEM,2,101
FITEM,2,104
A,P51X
FLST,2,4,3
FITEM,2,86
FITEM,2,90
FITEM,2,105
FITEM,2,101
A,P51X
FLST,2,4,3
FITEM,2,90
FITEM,2,94
FITEM,2,109
FITEM,2,105
A,P51X

!*generate wire and balls*!
RECTNG,20.45e-3,34.00e-3,2.20e-3,2.50e-3,
RECTNG,20.45e-3,34.00e-3,1.40e-3,2.20e-3,
RECTNG,20.45e-3,34.00e-3,1.10e-3,1.40e-3,
RECTNG,20.45e-3,34.00e-3,0.60e-3,1.10e-3,

!*three balls*!
CYL4,35.00e-3,5.5e-3,3.16e-3
CYL4,41.32e-3,5.5e-3,3.16e-3
CYL4,47.64e-3,5.5e-3,3.16e-3

RECTNG,34.00e-3,36.00e-3,2.20e-3,2.50e-3,
RECTNG,34.00e-3,36.00e-3,1.40e-3,2.20e-3,
RECTNG,34.00e-3,36.00e-3,1.10e-3,1.40e-3,
RECTNG,34.00e-3,36.00e-3,0.60e-3,1.10e-3,

RECTNG,36.00e-3,40.32e-3,2.20e-3,2.50e-3,
RECTNG,36.00e-3,40.32e-3,1.40e-3,2.20e-3,
RECTNG,36.00e-3,40.32e-3,1.10e-3,1.40e-3,

RECTNG,36.00e-3,40.32e-3,0.60e-3,1.10e-3,

RECTNG,40.32e-3,42.32e-3,2.20e-3,2.50e-3,
RECTNG,40.32e-3,42.32e-3,1.40e-3,2.20e-3,
RECTNG,40.32e-3,42.32e-3,1.10e-3,1.40e-3,
RECTNG,40.32e-3,42.32e-3,0.60e-3,1.10e-3,

RECTNG,42.32e-3,46.64e-3,2.20e-3,2.50e-3,
RECTNG,42.32e-3,46.64e-3,1.40e-3,2.20e-3,
RECTNG,42.32e-3,46.64e-3,1.10e-3,1.40e-3,
RECTNG,42.32e-3,46.64e-3,0.60e-3,1.10e-3,

RECTNG,46.64e-3,48.64e-3,2.20e-3,2.50e-3,
RECTNG,46.64e-3,48.64e-3,1.40e-3,2.20e-3,
RECTNG,46.64e-3,48.64e-3,1.10e-3,1.40e-3,
RECTNG,46.64e-3,48.64e-3,0.60e-3,1.10e-3,

RECTNG,48.64e-3,156.00e-3,2.20e-3,2.50e-3,
RECTNG,48.64e-3,156.00e-3,1.40e-3,2.20e-3,
RECTNG,48.64e-3,156.00e-3,1.10e-3,1.40e-3,
RECTNG,48.64e-3,156.00e-3,0.60e-3,1.10e-3,

!*subtract three rectangles from three balls*!
RECTNG,34.00e-3,36.00e-3,2.20e-3,2.50e-3,
RECTNG,40.32e-3,42.32e-3,2.20e-3,2.50e-3,
RECTNG,46.64e-3,48.64e-3,2.20e-3,2.50e-3,

!*firstly, change the booleans tolerance to 0.3e-3*!
BOPTN,KEEP,0
BOPTN,NWARN,0
BOPTN,VERS,RV52
BTOL,3e-004,
!*

ASBA, 44, 71
ASBA, 43, 70
ASBA, 42, 69

!*change the Booleans tolerance back to 1e-5*!
BOPTN,KEEP,0
BOPTN,NWARN,0
BOPTN,VERS,RV52
BTOL,1e-005,
!*

!*glue*!

FLST,2,3,5,ORDE,2
FITEM,2,1
FITEM,2,-3
AGLUE,P51X

FLST,2,65,5,ORDE,5
FITEM,2,4
FITEM,2,-41
FITEM,2,43
FITEM,2,-68
FITEM,2,72
AGLUE,P51X

!*compress number for areas*!
NUMCMP,AREA
NUMMRG,KP, , , ,LOW
APLOT

!*named blade*!
ALLSEL,ALL
FLST,5,3,5,ORDE,2
FITEM,5,1
FITEM,5,-3
ASEL,R, , ,P51X
CM,blade,AREA

!*named receptacle*!
ALLSEL,ALL
FLST,5,25,5,ORDE,4
FITEM,5,4
FITEM,5,-14
FITEM,5,17
FITEM,5,-30
ASEL,R, , ,P51X
/MREP,EPLT
CM,receptacle,AREA

!*named balls*!
ALLSEL,ALL
FLST,5,3,5,ORDE,2
FITEM,5,66
FITEM,5,-68
ASEL,R, , ,P51X
CM,balls,AREA

!*named wire*!

```

ALLSEL,ALL
FLST,5,37,5,ORDE,4
FITEM,5,15
FITEM,5,-16
FITEM,5,31
FITEM,5,-65
ASEL,R, , ,P51X
CM,wire,AREA

```

```

!*color the blade, receptacle, balls and wire*!

```

```

ALLSEL,ALL
APLOT
/COLOR,CM,ORAN,BALLS
/REPLOT

```

```

!*

```

```

/COLOR,CM,BLUE,BLADE
/REPLOT

```

```

!*

```

```

/COLOR,CM,RED,RECEPTACLE
/REPLOT

```

```

!*

```

```

/COLOR,CM,CYAN,WIRE
/REPLOT

```

```

!*

```

```

!*define material property, real constant, element type*!
!*blade_front part: MP=1, RC=3 thickness(1.5mm), ET=1*!

```

```

FLST,5,2,5,ORDE,2

```

```

FITEM,5,1

```

```

FITEM,5,-2

```

```

CM,_Y,AREA

```

```

ASEL, , , ,P51X

```

```

CM,_Y1,AREA

```

```

CMSEL,S,_Y

```

```

!*

```

```

CMSEL,S,_Y1

```

```

AATT, 1, 3, 1, 0,

```

```

CMSEL,S,_Y

```

```

CMDELE,_Y

```

```

CMDELE,_Y1

```

```

!*

```

```

!*blade_rear part: MP=7, RC=1 thickness(2.55mm), ET=1*!

```

```

CM,_Y,AREA

```

```

ASEL, , , , 3

```

```

CM,_Y1,AREA

```

```

CMSEL,S,_Y
!*
CMSEL,S,_Y1
AATT, 7, 1, 1, 0,
CMSEL,S,_Y
CMDELE,_Y
CMDELE,_Y1
!*

!*spring: MP=2, RC=3 thickness(1.5mm), ET=1*!
CM,_Y,AREA
ASEL,,,, 11
CM,_Y1,AREA
CMSEL,S,_Y
!*
CMSEL,S,_Y1
AATT, 2, 3, 1, 0,
CMSEL,S,_Y
CMDELE,_Y
CMDELE,_Y1
!*

!*end of the spring: MP=8, RC=2 thickness(1.9mm), ET=1*!
CM,_Y,AREA
ASEL,,,, 10
CM,_Y1,AREA
CMSEL,S,_Y
!*
CMSEL,S,_Y1
AATT, 8, 2, 1, 0,
CMSEL,S,_Y
CMDELE,_Y
CMDELE,_Y1
!*

!*annulus: MP=1, RC=2 thickness(1.9mm), ET=1*!
CM,_Y,AREA
ASEL,,,, 9
CM,_Y1,AREA
CMSEL,S,_Y
!*
CMSEL,S,_Y1
AATT, 1, 2, 1, 0,
CMSEL,S,_Y
CMDELE,_Y
CMDELE,_Y1

```

!*receptacle: MP=5(equivalent MP), RC=1 thickness(2.55mm), ET=1*!

FLST,5,31,5,ORDE,7

FITEM,5,4

FITEM,5,-8

FITEM,5,12

FITEM,5,-32

FITEM,5,34

FITEM,5,-37

FITEM,5,43

CM,_Y,AREA

ASEL, , , P51X

CM,_Y1,AREA

CMSEL,S,_Y

!*

CMSEL,S,_Y1

AATT, 5, 1, 1, 0,

CMSEL,S,_Y

CMDELE,_Y

CMDELE,_Y1

!*

!*balls: MP=4, RC=1 thickness(2.55mm), ET=1*!

FLST,5,3,5,ORDE,2

FITEM,5,66

FITEM,5,-68

CM,_Y,AREA

ASEL, , , P51X

CM,_Y1,AREA

CMSEL,S,_Y

!*

CMSEL,S,_Y1

AATT, 4, 1, 1, 0,

CMSEL,S,_Y

CMDELE,_Y

CMDELE,_Y1

!*

!*wire: MP=3, RC=4 thickness(1.12mm), ET=1*!

FLST,5,28,5,ORDE,5

FITEM,5,33

FITEM,5,38

FITEM,5,-42

FITEM,5,44

FITEM,5,-65

CM,_Y,AREA

ASEL, , , P51X

```

CM,_Y1,AREA
CMSEL,S,_Y
!*
CMSEL,S,_Y1
AATT, 3, 4, 1, 0,
CMSEL,S,_Y
CMDELE,_Y
CMDELE,_Y1

!*mesh size control*!
!*manual mesh size for blade*!
!*thickness of blade into 4 divisions*!
FLST,5,4,4,ORDE,4
FITEM,5,1
FITEM,5,3
FITEM,5,6
FITEM,5,9
CM,_Y,LINE
LSEL, , , ,P51X
CM,_Y1,LINE
CMSEL,,_Y
!*
LESIZE,_Y1, , ,4, , , ,1
!*

!*length of bladehead into 3 divisions*!
FLST,5,2,4,ORDE,2
FITEM,5,5
FITEM,5,7
CM,_Y,LINE
LSEL, , , ,P51X
CM,_Y1,LINE
CMSEL,,_Y
!*
LESIZE,_Y1, , ,3, , , ,1
!*

!*length of bladebody into 20 divisions*!
FLST,5,2,4,ORDE,2
FITEM,5,2
FITEM,5,4
CM,_Y,LINE
LSEL, , , ,P51X
CM,_Y1,LINE
CMSEL,,_Y
!*
LESIZE,_Y1, , ,20, , , ,1

```

```
!*  
  
!*length of blade back part into 20 divisions*!  
FLST,5,2,4,ORDE,2  
FITEM,5,8  
FITEM,5,10  
CM,_Y,LINE  
LSEL,,,P51X  
CM,_Y1,LINE  
CMSEL,,_Y  
!*  
LESIZE,_Y1,,,20,,,,,1  
!*
```

```
!*manual mesh size for receptacle*!  
!*thickness into 3 divisions*!  
FLST,5,36,4,ORDE,35  
FITEM,5,12  
FITEM,5,14  
FITEM,5,16  
FITEM,5,18  
FITEM,5,20  
FITEM,5,24  
FITEM,5,32  
FITEM,5,34  
FITEM,5,36  
FITEM,5,44  
FITEM,5,46  
FITEM,5,48  
FITEM,5,50  
FITEM,5,54  
FITEM,5,58  
FITEM,5,63  
FITEM,5,67  
FITEM,5,74  
FITEM,5,78  
FITEM,5,81  
FITEM,5,85  
FITEM,5,93  
FITEM,5,95  
FITEM,5,98  
FITEM,5,114  
FITEM,5,116  
FITEM,5,264  
FITEM,5,-266  
FITEM,5,268
```

```

FITEM,5,272
FITEM,5,275
FITEM,5,278
FITEM,5,283
FITEM,5,-284
FITEM,5,287
CM,_Y,LINE
LSEL,,,P51X
CM,_Y1,LINE
CMSEL,,_Y
!*
LESIZE,_Y1,,,3,,,,,1
!*

```

!*length of samll rectangles into 4 divisions*!

```

FLST,5,14,4,ORDE,10
FITEM,5,11
FITEM,5,13
FITEM,5,15
FITEM,5,17
FITEM,5,39
FITEM,5,-42
FITEM,5,261
FITEM,5,-262
FITEM,5,279
FITEM,5,-282
CM,_Y,LINE
LSEL,,,P51X
CM,_Y1,LINE
CMSEL,,_Y
!*
LESIZE,_Y1,,,4,,,,,1
!*

```

!*length of springend rectangle into 2 divisions*!

```

FLST,5,2,4,ORDE,2
FITEM,5,47
FITEM,5,49
CM,_Y,LINE
LSEL,,,P51X
CM,_Y1,LINE
CMSEL,,_Y
!*
LESIZE,_Y1,,,2,,,,,1
!*

```

!*length of median rectangles into 10 divisions*!

```
FLST,5,11,4,ORDE,11
FITEM,5,27
FITEM,5,31
FITEM,5,33
FITEM,5,94
FITEM,5,96
FITEM,5,155
FITEM,5,-156
FITEM,5,276
FITEM,5,-277
FITEM,5,285
FITEM,5,-286
CM,_Y,LINE
LSEL, , , ,P51X
CM,_Y1,LINE
CMSEL,,_Y
!*
LESIZE,_Y1, , ,10, , , ,1
!*
```

!*length of spring into 20 divisions*!

```
FLST,5,2,4,ORDE,2
FITEM,5,51
FITEM,5,-52
CM,_Y,LINE
LSEL, , , ,P51X
CM,_Y1,LINE
CMSEL,,_Y
!*
LESIZE,_Y1, , ,20, , , ,1
!*
```

!*curves of partial circle into 20 divisions*!

```
FLST,5,2,4,ORDE,2
FITEM,5,43
FITEM,5,45
CM,_Y,LINE
LSEL, , , ,P51X
CM,_Y1,LINE
CMSEL,,_Y
!*
LESIZE,_Y1, , ,20, , , ,1
!*
```

!*length of large rectangle into 18 divisions*!

```
FLST,5,2,4,ORDE,2
FITEM,5,269
FITEM,5,-270
CM,_Y,LINE
LSEL,,,P51X
CM,_Y1,LINE
CMSEL,,_Y
!*
LESIZE,_Y1,,,18,,,,1
!*
```

```
!*length of rectangle-rear part into 4 divisions*!
```

```
FLST,5,4,4,ORDE,4
FITEM,5,113
FITEM,5,115
FITEM,5,129
FITEM,5,-130
CM,_Y,LINE
LSEL,,,P51X
CM,_Y1,LINE
CMSEL,,_Y
!*
LESIZE,_Y1,,,4,,,,1
!*
```

```
!*manual mesh size control for cable*!
```

```
!*tiny thickness into 1 division*!
```

```
FLST,5,3,4,ORDE,3
FITEM,5,290
FITEM,5,-291
FITEM,5,313
CM,_Y,LINE
LSEL,,,P51X
CM,_Y1,LINE
CMSEL,,_Y
!*
LESIZE,_Y1,,,1,,,,1
!*
```

```
!*continue the previous: thickness into 3*!
```

```
FLST,5,3,4,ORDE,3
FITEM,5,134
FITEM,5,136
FITEM,5,295
CM,_Y,LINE
LSEL,,,P51X
```

```
CM,_Y1,LINE
CMSEL,,_Y
!*
LESIZE,_Y1,,3,,,,,1
!*
```

```
!*continue the previous: length of median rectangle into 10*!
FLST,5,3,4,ORDE,3
FITEM,5,298
FITEM,5,-299
FITEM,5,312
CM,_Y,LINE
LSEL,, , ,P51X
CM,_Y1,LINE
CMSEL,,_Y
!*
LESIZE,_Y1,, ,10,,,,,1
!*
```

```
!*continue the previous: length of small rectangle into 4*!
FLST,5,5,4,ORDE,5
FITEM,5,117
FITEM,5,121
FITEM,5,125
FITEM,5,132
FITEM,5,135
CM,_Y,LINE
LSEL,, , ,P51X
CM,_Y1,LINE
CMSEL,,_Y
!*
LESIZE,_Y1,, ,4,,,,,1
!*
```

```
!*thickness of median rectangle into 4*!
FLST,5,5,4,ORDE,5
FITEM,5,131
FITEM,5,133
FITEM,5,288
FITEM,5,-289
FITEM,5,292
CM,_Y,LINE
LSEL,, , ,P51X
CM,_Y1,LINE
CMSEL,,_Y
!*
```

```
LESIZE,_Y1, , ,4, , , ,1  
!*  

```

```
FLST,5,2,4,ORDE,2  
FITEM,5,296  
FITEM,5,-297  
CM,_Y,LINE  
LSEL, , , ,P51X  
CM,_Y1,LINE  
CMSEL,,_Y  
!*  

```

```
LESIZE,_Y1, , ,2, , , ,1  
!*  

```

```
!*continue the previous: thickness into 3*!  

```

```
FLST,5,14,4,ORDE,14  
FITEM,5,138  
FITEM,5,214  
FITEM,5,230  
FITEM,5,246  
FITEM,5,302  
FITEM,5,306  
FITEM,5,311  
FITEM,5,317  
FITEM,5,323  
FITEM,5,331  
FITEM,5,337  
FITEM,5,343  
FITEM,5,349  
FITEM,5,355  
CM,_Y,LINE  
LSEL, , , ,P51X  
CM,_Y1,LINE  
CMSEL,,_Y  
!*  

```

```
LESIZE,_Y1, , ,3, , , ,1  
!*  

```

```
!*continue the previous: thickness of median rectangle into 4*!  

```

```
FLST,5,7,4,ORDE,7  
FITEM,5,315  
FITEM,5,321  
FITEM,5,328  
FITEM,5,335  
FITEM,5,341  
FITEM,5,347  

```

```

FITEM,5,353
CM,_Y,LINE
LSEL,, , ,P51X
CM,_Y1,LINE
CMSEL,,_Y
!*
LESIZE,_Y1, , ,4, , , ,1
!*

```

!*continue the previous: thickness of median rectangle into 2*!

```

FLST,5,7,4,ORDE,7

```

```

FITEM,5,319
FITEM,5,325
FITEM,5,333
FITEM,5,339
FITEM,5,345
FITEM,5,351
FITEM,5,357
CM,_Y,LINE
LSEL,, , ,P51X
CM,_Y1,LINE
CMSEL,,_Y

```

```

!*
LESIZE,_Y1, , ,2, , , ,1
!*

```

!*length of median rectangles into 20 divisions*!

```

FLST,5,5,4,ORDE,5

```

```

FITEM,5,293
FITEM,5,-294
FITEM,5,314
FITEM,5,316
FITEM,5,318
CM,_Y,LINE
LSEL,, , ,P51X
CM,_Y1,LINE
CMSEL,,_Y

```

```

!*
LESIZE,_Y1, , ,20, , , ,1
!*

```

!*joint lines between cable and balls into 2 divisions*!

```

FLST,5,15,4,ORDE,15

```

```

FITEM,5,267
FITEM,5,300
FITEM,5,-301

```

```

FITEM,5,303
FITEM,5,-304
FITEM,5,310
FITEM,5,320
FITEM,5,322
FITEM,5,324
FITEM,5,334
FITEM,5,336
FITEM,5,338
FITEM,5,346
FITEM,5,348
FITEM,5,350
CM,_Y,LINE
LSEL, , , ,P51X
CM,_Y1,LINE
CMSEL,,_Y
!*
LESIZE,_Y1, , ,2, , , ,1
!*

```

!*lines between balls into 8 divisions*!

```

FLST,5,10,4,ORDE,10
FITEM,5,305
FITEM,5,307
FITEM,5,326
FITEM,5,-327
FITEM,5,329
FITEM,5,-330
FITEM,5,332
FITEM,5,340
FITEM,5,342
FITEM,5,344
CM,_Y,LINE
LSEL, , , ,P51X
CM,_Y1,LINE
CMSEL,,_Y
!*
LESIZE,_Y1, , ,8, , , ,1
!*

```

!*longest length of cable into 100 divisions*!

```

FLST,5,5,4,ORDE,5
FITEM,5,308
FITEM,5,-309
FITEM,5,352
FITEM,5,354

```

```

FITEM,5,356
CM,_Y,LINE
LSEL,,,P51X
CM,_Y1,LINE
CMSEL,_,_Y
!*
LESIZE,_Y1,,,100,,,,,1
!*

```

```

!*mesh blade, receptacle, and cable*!
FLST,5,65,5,ORDE,2
FITEM,5,1
FITEM,5,-65
CM,_Y,AREA
ASEL,,,P51X
CM,_Y1,AREA
CHKMSH,'AREA'
CMSEL,S,_Y
!*
MSHKEY,1
AMESH,_Y1
MSHKEY,0
!*
CMDELE,_,_Y
CMDELE,_,_Y1
CMDELE,_,_Y2
!*

```

```

!*mesh balls*!
SMRTSIZE,6

```

```

MSHKEY,0
FLST,5,3,5,ORDE,2
FITEM,5,66
FITEM,5,-68
CM,_Y,AREA
ASEL,,,P51X
CM,_Y1,AREA
CHKMSH,'AREA'
CMSEL,S,_Y
!*
AMESH,_Y1
!*
CMDELE,_,_Y
CMDELE,_,_Y1
CMDELE,_,_Y2

```

```

!*
!*generate contact pair*!
!*
/COM, CONTACT PAIR CREATION - START
CM,_NODECM,NODE
CM,_ELEMCM,ELEM
CM,_KPCM,KP
CM,_LINECM,LINE
CM,_AREACM,AREA
CM,_VOLUCM,VOLU
/GSAV,cwz,gsav,,temp
MP,MU,1,0.33
MAT,1
MP,EMIS,1,7.88860905221e-031
R,5
REAL,5
ET,2,169
ET,3,172
R,5,,,0.01,0.1,0,
RMORE,,,1.0E20,0.0,1.0,
RMORE,0.0,0,1.0,,1.0,0.5
RMORE,0,1.0,1.0,0.0,,1.0
KEYOPT,3,3,0
KEYOPT,3,4,0
KEYOPT,3,5,0
KEYOPT,3,7,0
KEYOPT,3,8,0
KEYOPT,3,9,0
KEYOPT,3,10,1
KEYOPT,3,11,0
KEYOPT,3,12,0
KEYOPT,3,2,0
! Generate the target surface
LSEL,S,,,2
LSEL,A,,,4
LSEL,A,,,5
LSEL,A,,,6
LSEL,A,,,7
CM,_TARGET,LINE
TYPE,2
NSLL,S,1
ESLN,S,0
ESURF
CMSEL,S,_ELEMCM
! Generate the contact surface

```

```

LSEL,S,,,13
LSEL,A,,,17
LSEL,A,,,33
LSEL,A,,,40
LSEL,A,,,42
LSEL,A,,,43
LSEL,A,,,47
LSEL,A,,,51
LSEL,A,,,156
LSEL,A,,,262
CM,_CONTACT,LINE
TYPE,3
NSLL,S,1
ESLN,S,0
ESURF
ALLSEL
ESEL,ALL
ESEL,S,TYPE,,2
ESEL,A,TYPE,,3
ESEL,R,REAL,,5
/PSYMB,ESYS,1
/PNUM,TYPE,1
/NUM,1
EPLOT
ESEL,ALL
ESEL,S,TYPE,,2
ESEL,A,TYPE,,3
ESEL,R,REAL,,5
CMSEL,A,_NODECM
CMDEL,_NODECM
CMSEL,A,_ELEMCM
CMDEL,_ELEMCM
CMSEL,S,_KPCM
CMDEL,_KPCM
CMSEL,S,_LINECM
CMDEL,_LINECM
CMSEL,S,_AREACM
CMDEL,_AREACM
CMSEL,S,_VOLUCM
CMDEL,_VOLUCM
/GRES,cwz,gsav
CMDEL,_TARGET
CMDEL,_CONTACT
/COM, CONTACT PAIR CREATION - END
/MREP,EPLOT

```

EPLOTT

SAVE,'model_LongBlade_static_LowE_step3_48Gap','db','C:\ansyscc\'

! Harmonic Analysis

/CWD,'C:\ansyscc'

RESUME, 'model_LongBlade_static_LowE_step3_48Gap','db','C:\ansyscc',0,0

/SOLU

!*

ANTYPE,3

!*

!*

HROPT,FULL

HROUT,ON

LUMPM,0

!*

EQSLV,FRONT,1e-008,

PSTRES,0

!*

HARFRQ,0.05,200,

NSUBST,200,

KBC,1

!*

ALPHAD,0,

BETAD,0,

DMPRAT,0,

!*

FLST,2,3,1,ORDE,3

FITEM,2,1286

FITEM,2,2112

FITEM,2,2710

!*

/GO

D,P51X, ,0,0, , ,ALL, , , , ,

FLST,2,3,1,ORDE,3

FITEM,2,121

FITEM,2,141

FITEM,2,143

!*

/GO

D,P51X, ,0,0, , ,UX, , , , ,

```

FLST,2,3,1,ORDE,3
FITEM,2,121
FITEM,2,141
FITEM,2,143
!*
/GO
D,P51X, ,0.0005,0, , ,UY, , , , ,

/STATUS,SOLU
SOLVE

!* Transient analysis

/CWD,'C:\ansyscc\'
RESUME,'model_LongBlade_static_LowE_step3','db','C:\ansyscc\' ,0,0

EPLOT

!*
FINISH
/SOL

!*define loads*!
!*The end of wire is fixed*!
FLST,2,3,1,ORDE,3
FITEM,2,1286
FITEM,2,2112
FITEM,2,2710
!*
/GO
D,P51X, ,0, , , ,ALL, , , , ,

!*read sine_static_xxHz_0p3mm function*!
*DEL,_FNCNAME
*DEL,_FNCMTID
*DEL,_FNCCSYS
*SET,_FNCNAME,'SS0p3_40'
*SET,_FNCCSYS,0
!/INPUT,sine_static_40Hz_0p3mm.func
*DIM,%_FNCNAME%,TABLE,6,6,1,,,,,%_FNCCSYS%
!
! Begin of equation: 0.0003*sin(251.2*{TIME})
*SET,%_FNCNAME%(0,0,1), 0.0, -999
*SET,%_FNCNAME%(2,0,1), 0.0
*SET,%_FNCNAME%(3,0,1), 0.0

```

```

*SET,%_FNCNAME%(4,0,1), 0.0
*SET,%_FNCNAME%(5,0,1), 0.0
*SET,%_FNCNAME%(6,0,1), 0.0
*SET,%_FNCNAME%(0,1,1), 1.0, -1, 0, 251.2, 0, 0, 1
*SET,%_FNCNAME%(0,2,1), 0.0, -2, 0, 1, -1, 3, 1
*SET,%_FNCNAME%(0,3,1), 0, -1, 9, 1, -2, 0, 0
*SET,%_FNCNAME%(0,4,1), 0.0, -2, 0, 0.0003, 0, 0, -1
*SET,%_FNCNAME%(0,5,1), 0.0, -3, 0, 1, -2, 3, -1
*SET,%_FNCNAME%(0,6,1), 0.0, 99, 0, 1, -3, 0, 0
! End of equation: 0.0003*sin(251.2*{TIME})
!-->

```

```

!*define displacement of blade at x-axis as 0*!

```

```

FLST,2,3,1,ORDE,3
FITEM,2,121
FITEM,2,141
FITEM,2,143
!*
/GO
D,P51X, ,0, , , ,UX, , , , ,

```

```

!*define displacement of blade at y-axis as sine_static_xxHz_0p3mm function*!

```

```

FLST,2,3,1,ORDE,3
FITEM,2,121
FITEM,2,141
FITEM,2,143
!*
/GO
D,P51X, , %SS0p3_40% , , , ,UY, , , , ,

```

```

!*solution control*!

```

```

!*analysis type: transient*!

```

```

!*
ANTYPE,4
!*
TRNOPT,FULL
LUMPM,0
!*
ANTYPE,4
NLGEOM,1
NSUBST,480,480,480
OUTRES,ERASE
OUTRES,ALL,ALL
TIME,0.3

```

```

NEQIT,50

```

```
!*solve*!  
/STATUS,SOLU  
/nerr,100,100,off
```

```
SOLVE
```

**APPENDIX B MATLAB CODE EXAMPLE FOR TRANSFER FUNCTION
AND RELATIVE MOTION CALCULATION**

```
“Transfer_functions_star_reflow_type_c.m”  
  
load Reflow_43gap_50mV_1.TXT  
  
load Reflow_43gap_50mV_2.TXT  
  
load Reflow_43gap_50mV_3.TXT  
  
load Star_43gap_40mV_1.TXT  
  
load Star_43gap_40mV_2.TXT  
  
load Star_43gap_40mV_3.TXT  
  
load Star_43gap_40mV_3.TXT  
  
hold on  
  
plot((Reflow_43gap_50mV_1(21:141,1)+Reflow_43gap_50mV_2(21:141,1)+Reflow_43gap_50mV_3(21:141,1))/3,(Reflow_43gap_50mV_1(21:141,2)+Reflow_43gap_50mV_2(21:141,2)+Reflow_43gap_50mV_3(21:141,2))/3)  
  
plot((Star_43gap_40mV_1(1:121,1)+Star_43gap_40mV_2(1:121,1)+Star_43gap_40mV_3(1:121,1)+Star_43gap_40mV_4(1:121,1))/4,(Star_43gap_40mV_1(1:121,2)+Star_43gap_40mV_2(1:121,2)+Star_43gap_40mV_3(1:121,2)+Star_43gap_40mV_4(1:121,2))/4,'g')  
  
“Relativemotion_Type2_all.m”  
clear all  
close all  
M=10;  
N=75;  
load Star_43gap_40mV_1.TXT  
  
load Star_48gap_40mV_1.TXT
```

```

load Star_53gap_40mV_1.TXT

s43=Star_43gap_40mV_1;
s48=Star_43gap_40mV_1;
s53=Star_43gap_40mV_1;

f=s43(:,1);

[n,m]=size(s43);

for i=1:n,

    mags43(i)=sqrt((1-s43(i,2))^2+s43(i,3)^2);
    imags43(i)=1/mags43(i);
    mags48(i)=sqrt((1-s48(i,2))^2+s48(i,3)^2);
    imags48(i)=1/mags48(i);
    mags53(i)=sqrt((1-s53(i,2))^2+s53(i,3)^2);
    imags53(i)=1/mags53(i);
end

figure;

f2=[30,35,40,45,50];

fs48=[4.4,2.5,.85,1.2,1.4];
fs43=[5.25,2.6,1.5,0.9,1.2];

fs53=[2.9,1.45,0.6,1.,1.3]*1;
fs53sim=[2.8,1.6,1.2,0.7,0.8]*1;

fs48sim=[4.2,2.4,1.3,1.0,1.0]*1;
fs43sim=[5.1,2.7,1.8,1.05,1.0]*1;
sc1=fs43(1)/imags43(21);
sc2=fs48(1)/imags48(21);
sc3=fs53(1)/imags53(21);

plot(f(M:N),sc3*imags53(M:N),'k--',f(M:N),sc2*imags48(M:N),'k-
.',f(M:N),sc1*imags43(M:N),'k-')

hold

plot(f2,fs53sim,'k*')
plot(f2,fs48sim,'kd')
plot(f2,fs43sim,'ks')

```

```
legend('Type 2.a Scaled Inv. Rel. Motion Tran.Fun.', 'Type 2.b Scaled Inv. Rel.  
Motion Tran.Fun.', 'Type 2.c Scaled Inv. Rel. Motion Tran.Fun.', 'Type 2.a Threshold  
Value from 3D simulation', 'Type 2.b Threshold Value from 3D simulation', 'Type 2.c  
Threshold Value from 3D simulation')
```

```
hold off
```

```
xlabel('Frequency (Hz)')
```

```
ylabel('Threshold Displacement at the Shaker Head (mm)')
```

```
axis([25,55,0,10]);
```